TECHNISCHE UNIVERSITÄT MÜNCHEN
Lehrstuhl für Grünlandlehre

Assessing spatial variability of floodplain soil thickness with auxiliary high-resolution data and geostatistical modelling

Tom Gottfried

Vollständiger Abdruck der von der Fakultät Wissenschaftszentrum Weihenstephan der Technischen Universität München zur Erlangung des akademischen Grades eines

Doktors der Agrarwissenschaften

genehmigten Dissertation.

Vorsitzender: Univ.-Prof. Dr. H. Bernhardt

Prüfer der Dissertation:

1. apl. Prof. Dr. K. F. Auerswald
2. Univ.-Prof. Dr. U. Schmidhalter
3. Prof. Dr. P. Fiener (Indian Institute of Technology Madras/Indien)
   nur schriftliche Beurteilung

Die Dissertation wurde am 18.04.2012 bei der Technischen Universität München eingereicht und durch die Fakultät Wissenschaftszentrum Weihenstephan am 26.06.2012 angenommen.

«Je me demande, dit-il, si les étoiles sont éclairées afin que chacun puisse un jour retrouver la sienne.»

Antoine de Saint-Exupéry (1946): Le Petit Prince

Contents

Abstract

Soils provide functions, which are equally crucial for crop production and the provision of ecosystem services. Mostly, these functions are also related to soil thickness. It is known that spatial variation of soil properties occurs, more or less continuously, even within soil map units and uniformly managed fields. Especially, floodplain soils are characterised by lateral and vertical small scale patterns in soil properties induced by differing sedimentation conditions during substrate genesis. Such small scale variations can be assessed by means of high resolution auxiliary data. Auxiliary data that are commonly in use are the electrical conductivity of the ground and digital elevation models. Both are easily and non-invasively obtained at a spatial resolution corresponding to a subfield scale and are physically related to soil thickness. The hypothesis tested in the present study is that the physical relations between soil thickness, topography, groundwater table depth and electrical conductivity of the ground can be exploited for the prediction of soil thickness. Further, setting up a model that explicitly takes into account the spatial variability of these relations is hypothesised to overcome the shortcomings of a model assuming globally valid parameters.

To provide electrical conductivity of the ground as an auxiliary variable in appropriate spatial detail, an extensive survey was conducted with mobilised equipment. Therefore, a model that corrects for an offset between measured positions and sensor positions was developed. The provision of spatially detailed information about groundwater table height was accomplished by a physical conceptual model of the shallow unconfined water table at the study site. Groundwater table depth and the wetness index, a hydrologically based land-surface parameter, were derived from a digital elevation model. Measured values of soil thickness were provided by soil sampling. A physically based regression model was developed to relate soil thickness to the auxiliary data. A process based structural analysis of the semivariograms of involved variables was used to assess their spatial covariation. The regression model was fitted to neighbourhoods around each sampling location.

The obtained maps and the structural analysis of semivariograms showed distinct patterns of spatial variation shared between the physically related auxiliary variables and soil thickness. The local fitting of the physically based regression model lead to sufficiently accurate predictions of soil thickness, despite the heterogeneous soils at the study site. The prediction error was of similar magnitude as micro scale spatial variation of soil thickness observed during soil sampling. This micro scale variation could not be incorporated in the model due to the larger support of the auxiliary variables.

The physically based model allowed some generalisation to different configurations of layering in the ground. Ignoring these different configurations partly lead to few large values of residual soil thickness (>1.2 m) after fitting the regression model. Respecting the different layer configurations reduced the residuals to a maximum of 0.3 m. The possibility to be extended to more general conditions offered by the physically based regression model exhibits its validity beyond being a mere site specific regression model.

Overall, the methods and results presented in this study give evidence, that physical reality is worth being considered explicitly in the formulation of models for variables in different applications.

Zusammenfassung

Böden stellen Funktionen für den Anbau landwirtschaftlicher Produkte und die Umwelt zur Verfügung, die zum Teil von der Bodenmächtigkeit abhängen. Bodeneigenschaften variieren bekanntermaßen mehr oder weniger kontinuierlich auch auf räumlichen Skalen innerhalb von Feldern und kartierten Bodeneinheiten. Besonders Schwemmlandböden zeichnen sich, auf Grund der variierenden Bedingungen während der Sedimentation, durch horizontale und vertikale kleinräumige Variation aus. Derartige kleinräumige Variation kann mittels hochauflösend vorhandener Co-Variablen erfasst werden. Elektrische Bodenleitfähigkeit und digitale Höhenmodelle sind hierfür häufig verwendete Co-Variablen. Beide können leicht und ohne Zerstörung hochauflösend erfasst werden und hängen physikalisch mit der Bodenmächtigkeit zusammen. In der vorliegenden Studie wurde die Hypothese getestet, ob die physikalischen Zusammenhänge zwischen Bodenmächtigkeit, Topographie, Grundwasserflurabstand und elektrischer Bodenleitfähigkeit für die Vorhersage der Bodenmächtigkeit genutzt werden können. Zudem wurde getestet, ob ein Modell, das die räumliche Variabilität dieser Zusammenhänge berücksichtigt, die Nachteile der Annahme eines global einheitlichen Zusammenhanges ausgleicht.

Um die elektrische Bodenleitfähigkeit in angemessener räumlicher Detailliertheit erfassen zu können, wurde sie mit mobiler Ausrüstung erfasst. Zu diesem Zweck wurde ein Modell entwickelt, dass einen Versatz zwischen gemessenen Positionen und Sensor-Positionen korrigiert. Räumlich detaillierte Informationen über die Höhe des Grundwasserspiegels wurden mit einem physikalisch konzeptionellen Modell des flachen ungespannten Grundwasserspiegels am untersuchten Standort ermittelt. Grundwasserflurabstand und ein hydrologisch basierter Landform-Parameter wurden aus einem digitalen Höhenmodell abgeleitet. Messwerte der Bodenmächtigkeit wurden anhand von Bodenproben ermittelt. Ein physikalisch basiertes Regressionsmodell wurde entwickelt, um den Zusammenhang zwischen Bodenmächtigkeit und Co-Variablen zu erklären. Eine Analyse der Semivariogramm-Strukturen aller Variablen wurde genutzt, um deren räumliche Co-Variation zu ermitteln. Das Regressionsmodell wurde in räumlich begrenzten Nachbarschaften um die Probenahmeorte angepasst.

Die erstellten Karten und die Semivariogrammanalyse zeigten abgrenzbare Muster räumlicher Variation, die den Variablen gemeinsam waren. Das räumlich begrenzte Anpassen des Modells resultierte in genauen Vorhersagen der Bodenmächtigkeit, trotz der heterogenen Böden am untersuchten Standort. Der Fehler der Vorhersage war von der gleichen Größenordnung wie die mikro-skalige Variation der Bodenmächtigkeit, wie sie bei der Probenahme festgestellt wurde. Die mikro-skalige Variation konnte nicht im Modell integriert werden, da die Co-Variablen über größere Flächen erfasst wurden.

Das physikalisch basierte Modell ermöglichte eine Generalisierung hin zu verschiedenen Schicht-Anordnungen im Untergrund. Wurden diese ignoriert, kam es zu großen Residuen des Regressionsmodells (>1.2 m) nach dessen Anpassung. Wurden sie beachtet, waren die Residuen maximal 0.3 m. Die Möglichkeit der Generalisierung des physikalisch basierten Modells zeigt seine Validität über die eines rein standortbezogenen Regressionsmodells hinaus.

Insgesamt zeigen die vorgestellten Methoden und Ergebnisse, dass die explizite Einbeziehung physikalischer Gegebenheiten in die Formulierung von Modellen für unterschiedliche Variablen von Nutzen ist.

1 Introduction

Soils provide functions that are equally crucial for crop production and the provision of ecosystem services. Among such functions are storage of nutrients or water, regulation of water and matter fluxes and filtering of pollutants (Cassman, 1999; Kibblewhite et al., 2008). Soil thickness is an important control of these functions, as it is proportional to soil volume. Accordingly it is a crucial soil property with respect to crop productivity (Power et al., 1981) and plays an important role in hydrological modelling (Francés and Lubczynski, 2011).

It is known that spatial variation of soil properties occurs, more or less continuously, even within soil map units and uniformly managed fields (Burrough et al., 1997; Lin et al., 2005). Especially, floodplain soils are characterised by lateral and vertical small scale patterns in soil properties induced by differing sedimentation conditions during substrate genesis (Goulard and Voltz, 1992; Li et al., 1997). Accordingly, Goulard and Voltz (1992) observed a short range (≈20 m) spatial structure in soil hydraulic properties of an alluvial plain, which they attributed to local variations of water velocity at the time of deposition of the alluvium. Iqbal et al. (2005) proposed a spacing between sampling sites of less than 100 m for assessing soil hydraulic properties on alluvial soils. Another source of spatial variation occurs where floodplain soils consist of young fluvial deposits that fill the channels of old braided rivers (Hagedorn and Rother, 1992). In such a case, also soil thickness can be expected to exhibit small scale patterns, inherited from the paleotopography of the braided riverbed.

When a detailed and spatially explicit understanding of soil functioning related to soil thickness is needed, soil thickness has to be assessed in the corresponding detailedness. A direct measurement of soil properties such as soil thickness, however, is not generally possible in a non-destructive manner, because the soil is opaque and its lower limit hidden from view (Kuriakose et al., 2009; Lück et al., 2009). Indirect assessment has to involve auxiliary data that are appropriate as a proxy for the target variable and are obtainable in a resolution corresponding to the desired detailedness.

Auxiliary data that are commonly in use are among others the electrical conductivity of the ground and digital elevation models (DEM; McBratney et al., 2003). Both are easily and non-invasively obtained at a spatial resolution corresponding to a subfield scale.

Soil electrical conductivity is influenced by many physical and chemical properties (Auerswald et al., 2001; Friedman, 2005; McNeill, 1980a), rendering it an integrative measure of these properties. In turn, it is widely used as a proxy of soil properties and has become a valuable tool for assessing soil spatial variability (Corwin and Lesch, 2005b; Samouëlian et al., 2005). The possibility to quickly and non-invasively collect data in high spatial resolution is the key to the ease of use and cost-effectiveness of this method, especially if the measurement is accomplished with mobile equipment and a positioning system (Adamchuk et al., 2004; Lück et al., 2009; Samouëlian et al., 2005). The measurement of soil electrical conductivity can be accomplished differently (Corwin and Lesch, 2005a), e.g. with electrodes that have direct contact to the soil or with electromagnetic induction (Sudduth et al., 2003). In the latter case, it will be referred to as apparent electrical conductivity of the ground (σ_a) in the following.

σ_a is related to the thickness of distinct horizontal layers of the ground and thus can be used to deduce their thickness. Use of this has been made to predict soil thickness or the depth to the limit between other contrasting layers in the ground, such as depth to clay rich layers or groundwater table depth. The assessment of the relationship between σ_a and the depth of soil layers has been conducted using simple linear regression (Boettinger et al., 1997; Bork et al., 1998; Doolittle and Collins, 1998; Kitchen et al., 1996; Mertens et al., 2008) or using exponential or other functions to describe the relationship (Brus et al., 1992; Doolittle et al., 1994; Kitchen et al., 1999; Knotters et al., 1995; Saey et al., 2011; Sudduth et al., 2010). Some authors also used physically based depth response functions of the measurement instruments to derive the

relationship between σ_a and the limit between two contrasting soil layers (Saey et al., 2009, 2008; Sudduth et al., 2010). An explicit incorporation of spatial correlation into the modelling approach has also been applied for the prediction of depths (Bourennane and King, 2003; Francés and Lubczynski, 2011; Knotters et al., 1995). For the assessment of groundwater table depth, σ_a was used directly as a predictor in simple linear regression (Sherlock and McDonnell, 2003) and multiple linear regression (Buchanan and Triantafilis, 2009) and as logarithms of σ_a (Schumann and Zaman, 2003).

The shape of the land surface controls geomorphological processes and is, in turn, the outcome of geomorphological processes.Thus, land-surface parameters can be obtained, which reflect geomorphological processes related to soil properties (Moore et al., 1993). Especially, the way water moves in the landscape is influenced by the shape of the land surface. This gives the possibility to derive land-surface parameters that are related to hydrological parameters such as soil moisture (Moore et al., 1991; Peckham, 2009) and explain their variability at a range of spatial scales from decimetres to whole catchments (Hoover and Wolman, 2005; Western et al., 1999). Soil thickness can be a response of the downslope transport of material (Moore et al., 1993) and the preferential downslope transport of fine material affects soil texture (Rosenbloom et al., 2001). Land-surface parameters are therefore appropriate auxiliary variables for soil mapping, usually derived from a DEM (Dobos and Hengl, 2009; McBratney et al., 2003; Moore et al., 1993). High resolution DEMs can be derived from different data sources, e.g. airborne laser scanning (Nelson et al., 2009).

Electrical conductivity of the soil, and thus σ_a, is dependent on soil moisture because current mainly passes through the water filled pore volume (Auerswald et al., 2001; Brevik et al., 2006; Friedman, 2005; McNeill, 1980a). Another important control of soil electrical conductivity, especially for non-saline soils, is fine-textured material due to the conductance of adsorbed ions along the surface of such materials (Auerswald et al., 2001; Friedman, 2005). Texture, moisture and thickness of soils are thus related to both σ_a and topography. It follows that also their spatial patterns are related (Heil and Schmidhalter, 2012) and spatial covariation should reflect the interactions of the physical processes these soil properties are subject to.

The hypothesis tested in the present study is that the physical relations between soil thickness, topography, groundwater table depth and σ_a can be exploited for the prediction of soil thickness. Further, setting up a model that explicitly takes into account the spatial variability of these relations is hypothesised to overcome the shortcomings of a model assuming globally valid parameters. A theoretical consideration of these hypotheses is given in chapter 4.

The testing of the hypotheses was accomplished by the prediction of the thickness of shallow floodplain soils (0.1 m to 1.5 m) over gravely substrate and a shallow groundwater table (0.1 m to 1.5 m). To provide σ_a as an auxiliary variable in appropriate spatial detail, an extensive survey was conducted with mobilised equipment. In such surveys, a common complication arises from the fact, that the used Global Positioning System (GPS) antenna cannot easily be placed on top of the measuring instrument. This leads to an offset between the measured positions and the actual instrument positions. Therefore, a solution was developed, which provided instrument positions with appropriate accuracy. This solution is deemed important beyond the scope of the present study. It is thus described and evaluated in detail in an extra chapter (chapter 2), which has been published (Gottfried et al., 2012). The provision of spatially detailed information about groundwater table depths was accomplished by a physical conceptual model of the shallow unconfined water table at the study site. The model incorporated regional scale and drainage ditch induced gradients as well as seasonal and weather induced fluctuations. These allowed predictions of the groundwater table, which were suitable for the joint analysis with other high resolution auxiliary variables. The groundwater table model is presented and evaluated in an extra chapter too (chapter 3), because the unique methodology needed a close look on its validity and performance and is deemed to be more generally applicable.

2 Kinematic correction for the spatial offset between sensor and position data

2.1 Introduction

Detailed knowledge about site patterns at fine resolution is needed for decisions on a wide range of environmental and farm management problems (Adamchuk et al., 2004; Auernhammer, 2001; Grunwald, 2009). Accordingly, sensor-based soil testing and digital processing of recorded data, referred to as digital soil mapping (Grunwald, 2009; McBratney et al., 2003), has become a widely used approach in soil science. Ground-based sensor systems are used in various fields such as precision farming (Adamchuk et al., 2004; Auernhammer, 2001; Corwin and Plant, 2005), environmental analyses (Buchanan and Triantafilis, 2009; Peters et al., 1994), detection of buried objects such as unexploded ordnance (Nelson and McDonald, 2001; Peters et al., 1994) or archaeology (Kvamme, 2003). The applied sensors examine ground electrical or electromagnetic properties like in the case of apparent electrical conductivity of the ground (Corwin and Plant, 2005) or ground penetrating radar measurements (Huisman et al., 2003; Peters et al., 1994). They measure yield (Birrell et al., 1996), or light reflectance properties of the soil (Sudduth and Hummel, 1993) or the plant canopy (Mistele and Schmidhalter, 2008). Though many applications of digital soil mapping are research oriented and lack the information on their economical traits (Grunwald, 2009), sensor based mapping, as a technology for precision agriculture, has the potential to improve cost effectiveness in agricultural production (Adamchuk et al., 2004; Massey et al., 2008; Sonka et al., 1997).

The variation of site variables is more or less continuous (Burrough et al., 1997; Heuvelink and Webster, 2001), and soils and crop properties vary significantly within fields (Corwin and Lesch, 2005a). Spatial autocorrelation ranges are often smaller than 100 m (McBratney and Pringle, 1999). Lin et al. (2005) found most of the variation of various soil properties occurring within 12 m. Consequently, a resolution of <20 m is suggested for soil surveys at the field scale, e.g. for precision farming (McBratney et al., 2000), and even a pixel width of 5 m has been suggested (McBratney et al., 2003). Recognising patterns at such a scale calls for distances between neighbouring measured positions similar to the pixel size of the desired map (Hengl, 2006). In ground-based surveys, this is usually accomplished by ''on-the-go'' sensor applications with vehicle-mounted sensors and a global navigation satellite system (GNSS, such as the Global Positioning System, GPS) receiver connected to a computer, which synchronously collects the measurements of both instruments (Adamchuk et al., 2004).

A possible complication in such a configuration is that the locations of the sensor and the GNSS antenna measurements may differ. This can occur due to asynchronous measurements in on-the-go applications such as yield data recording, when the harvested good has to be processed through the combine before measurement (Ross et al., 2008; Sudduth and Drummond, 2007). A time lag in the data acquisition system can also cause a spatial offset as a function of driving velocity (Sudduth et al., 2001). A spatial offset also occurs where the GNSS antenna is not placed directly on top of the sensor (Speckmann, 2000). For example, in soil electrical conductivity surveys based on electromagnetic induction, metallic objects (i.e. the GNSS antenna) within proximity of the electrical conductivity sensor interfere with the electromagnetic measurement (Freeland et al., 2002; Sudduth et al., 2001). In this case the GNSS antenna must either be placed on top of the sensor in appropriate height as in the example given in Corwin and Lesch (2005b) or in appropriate lateral distance. A spatial offset as resulting from the latter increases the uncertainty of the relationship of georeferenced variables (Grimm and Behrens, 2010) and adds uncertainty to geostatistical estimation of the measured variable (Cressie and Kornak, 2003). Thus, the measured GNSS antenna positions have to be corrected, at least if the offset is relevant for the required accuracy of positioning. As a rule of thumb, this is roughly half of the resolution of the final map (Hengl, 2006).

The temporal offset due to processing of threshing goods in a combine has been extensively studied (see review by Ross et al., 2008). The correction of a spatial offset can be simple, if only a constant spatial vector has to be added to the coordinate vectors (Ross et al., 2008). More sophisticated methods have to be applied, if the offset depends on movement parameters such as velocity of the vehicle, travel direction or curve radius. Such conditions require a model that predicts the offset between measured GNSS antenna positions and true sensor positions based on the underlying mechanisms. The mathematical description of the path of a mass point (the pursuer) following another mass point (the pursued) at constant distance and with velocity always directed to the pursued is called a tractrix (Garlick et al., 1993). This kinematic concept seems promising for the prediction of the positions of a sensor towed by a GNSS-equipped vehicle.

In the present study, a model is presented using a tractrix equation that describes the position of a sensor on a cart or sledge towed by a vehicle equipped with a positioning system. The applicability of the model is examined with respect to measurements with a ground conductivity meter and the model's benefits regarding the accuracy of the resulting map are demonstrated.

2.2 Model development

The kinematic model describes the movement of a sensor (mounted on a cart or sledge) along its pathway $\mathbf{S}(t)$ as a function of the pathway $\mathbf{G}(t)$ of a GNSS antenna, which is mounted on the vehicle drawing the sensor. The sensor is towed to a pivot at the rear of the vehicle. The pivot moves along $\mathbf{P}(t)$. The fixed spacing between pivot and sensor is given by $l = |\mathbf{P} - \mathbf{S}|$ (figure 2.1a). While the vehicle moves, the GNSS antenna positions $\mathbf{G}_i = \mathbf{G}(t_i)$ are measured at discrete times t_i along the continuous pathway $\mathbf{G}(t)$. The sensor collects data along the pathway $\mathbf{S}(t)$ at sensor positions $\mathbf{S}_i = \mathbf{S}(t_i)$ synchronously to the GNSS measurements. To derive $\mathbf{S}_i$ from the set of positions $\mathbf{G}_i$, the problem is split. First, the set $\mathbf{P}_i = \mathbf{P}(t_i)$ of pivot positions is derived from $\mathbf{G}_i$. Then, $\mathbf{S}_i$ is derived from $\mathbf{P}_i$. In the following, the pathways are given in an earth-fixed Cartesian coordinate system, which is called the field coordinate system (Zhang and Qiu, 2004). For a more detailed description of coordinate systems with respect to vehicle motion see e.g. Zhang and Qiu (2004) or Skog and Händel (2009).

2.2.1 Relationship between GNSS antenna and pivot positions

GNSS antenna and pivot have fixed positions on the vehicle, that are denoted $\mathbf{G}'$ and $\mathbf{P}'$ in the Cartesian vehicle coordinate system (with the x'-axis pointing in the direction of vehicle heading and the y'-axis pointing to the lateral (leftward) direction; figure 2.1a). The $\mathbf{P}_i$ are calculated by rotating the vector $(\mathbf{G}' - \mathbf{P}')$ from the vehicle coordinate system into the field coordinate system according to

$$\mathbf{P}_i = \mathbf{G}_i - \begin{pmatrix} \cos\alpha_i^* & -\sin\alpha_i^* \\ \sin\alpha_i^* & \cos\alpha_i^* \end{pmatrix} (\mathbf{G}' - \mathbf{P}') \quad , \tag{2.1}$$

where α_i^* is the heading of the vehicle at $\mathbf{G}_i$. Often heading is not recorded with GNSS data. Thus, α_i^* is approximated for all $1 < i < n$ by the direction of the vector $(\mathbf{G}_{i+1} - \mathbf{G}_{i-1})$ (figure 2.1b),

$$\cos\alpha_i^* = \frac{(\mathbf{G}_{i+1} - \mathbf{G}_{i-1})_x}{|\mathbf{G}_{i+1} - \mathbf{G}_{i-1}|} \quad , \qquad \sin\alpha_i^* = \frac{(\mathbf{G}_{i+1} - \mathbf{G}_{i-1})_y}{|\mathbf{G}_{i+1} - \mathbf{G}_{i-1}|} \quad , \tag{2.2}$$

where the indices x and y denote the respective components of the vector. α_1^* is approximated by the direction of $(\mathbf{G}_2 - \mathbf{G}_1)$, and α_n^* by the direction of $(\mathbf{G}_n - \mathbf{G}_{n-1})$.

2.2.2 Relationship between pivot and sensor positions

The curve $\mathbf{S}(t)$ of the sensor is described by the tractrix of the pathway $\mathbf{P}(t)$ of the pivot, since the sensor is towed to the pivot. $\mathbf{P}$ is assumed to move on a straight line between $\mathbf{P}_i$ and $\mathbf{P}_{i+1}$

(which is justified for sufficiently small time intervals between two measurements). The heading, α_i, is thus constant between $\mathbf{P}_i$ and $\mathbf{P}_{i+1}$ and is given by

$$\cos\alpha_i = \frac{(\mathbf{P}_{i+1} - \mathbf{P}_{i-1})_x}{|\mathbf{P}_{i+1} - \mathbf{P}_{i-1}|} \quad , \qquad \sin\alpha_i = \frac{(\mathbf{P}_{i+1} - \mathbf{P}_{i-1})_y}{|\mathbf{P}_{i+1} - \mathbf{P}_{i-1}|} \quad . \tag{2.3}$$

The sensor position $\mathbf{S}_{i+1}$ is derived from the previous sensor position $\mathbf{S}_i$ and the movement of the sensor along the tractrix $\mathbf{S}(t)$ according to

$$\mathbf{S}_{i+1} = \mathbf{S}_i + \int_{t_i}^{t_{i+1}} \frac{\mathrm{d}\mathbf{S}}{\mathrm{d}t}\,\mathrm{d}t \quad . \tag{2.4}$$

Therefore the movement of the pivot, $\frac{\mathrm{d}\mathbf{P}}{\mathrm{d}t}$, is decomposed in two components, one in direction of $(\mathbf{P}(t) - \mathbf{S}(t))$ and one perpendicular to $(\mathbf{P}(t) - \mathbf{S}(t))$. The first component, in direction of $(\mathbf{P}(t) - \mathbf{S}(t))$, is given by $\cos\varphi\,\frac{\mathrm{d}P}{\mathrm{d}t}$, where $P = |\mathbf{P}(t) - \mathbf{P}_i|$, and φ is the direction of $(\mathbf{P}(t) - \mathbf{S}(t))$ in the vehicle coordinate system (figure 2.1c). Thus, as the sensor is towed to the pivot with fixed spacing, the instantaneous movement $\frac{\mathrm{d}\mathbf{S}}{\mathrm{d}t}$ of the sensor equals the magnitude and respective direction of the component. In field coordinates,

$$\frac{\mathrm{d}\mathbf{S}}{\mathrm{d}t} = \begin{pmatrix}\cos(\alpha_i + \varphi)\\ \sin(\alpha_i + \varphi)\end{pmatrix} \cos\varphi \frac{\mathrm{d}P}{\mathrm{d}t} \quad . \tag{2.5}$$

For convenient model implementation and consistency with equation (2.3), $\cos(\alpha_i + \varphi)$ and $\sin(\alpha_i + \varphi)$ can each be decomposed using the addition theorems for trigonometric functions. The second component, perpendicular to the first, is given by $\sin\varphi\,\frac{\mathrm{d}P}{\mathrm{d}t}$ and describes the rotation of the pivot around the sensor (figure 2.1c),

$$l\frac{\mathrm{d}\varphi}{\mathrm{d}t} = -\sin\varphi\frac{\mathrm{d}P}{\mathrm{d}t} \quad . \tag{2.6}$$

To describe the change of direction of the sensor movement while the pivot moves between $\mathbf{P}_i$ and $\mathbf{P}_{i+1}$, equation (2.6) is solved for φ as a function of P. Therefore, equation (2.6) is rearranged

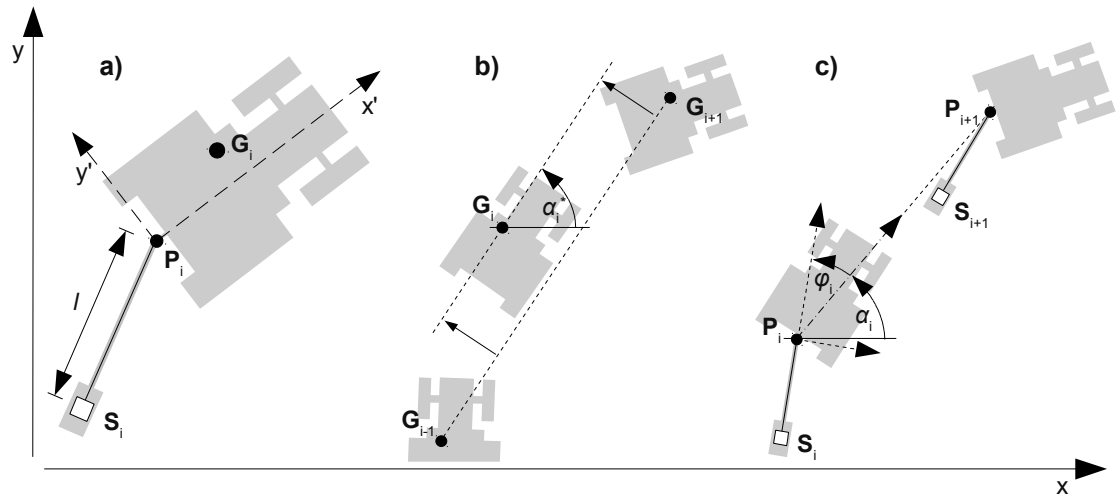

Figure 2.1: Schematic illustration of the kinematic model.
a) A drawing vehicle is equipped with a GNSS antenna at position $\mathbf{G}_i$. A sensor at position $\mathbf{S}_i$ is attached to the vehicle at a pivot (e.g. trailer coupling) at position $\mathbf{P}_i$. The index i denotes a specific point in time. l denotes the spacing between $\mathbf{P}_i$ and $\mathbf{S}_i$. Two coordinate systems are shown: x and y denote the earth-fixed field coordinate system, whereas x' and y' denote the vehicle-fixed vehicular coordinate system. b) The heading of the GNSS antenna in the field coordinate system at time t_i, α_i^*, is approximated by the direction of the vector $(\mathbf{G}_{i+1} - \mathbf{G}_{i-1})$. c) The heading of the pivot in the field coordinate system is denoted α_i for $t_i < t < t_{i+1}$. The direction of $(\mathbf{P}' - \mathbf{S}_i')$ in the vehicle coordinate system is φ_i. The movement of the pivot (dash-dotted arrow) is decomposed in two components (dotted arrows) to describe the movement of the sensor. One component points in direction $(\alpha_i + \varphi_i)$, the other perpendicular to $(\alpha_i + \varphi_i)$.

to obtain

$$\frac{1}{\sin\varphi}\frac{\mathrm{d}\varphi}{\mathrm{d}t} = -\frac{1}{l}\frac{\mathrm{d}P}{\mathrm{d}t} \quad . \tag{2.7}$$

Let φ_i be the direction of $(\mathbf{P}_i - \mathbf{S}_i)$. Integrating equation (2.7) from φ_i to φ gives

$$\int_{\varphi_i}^{\varphi} \frac{1}{\sin\varphi}\,\mathrm{d}\varphi = -\frac{1}{l}\int 1\,\mathrm{d}P \;\Leftrightarrow\; \ln\left(\tan\left(\frac{\varphi}{2}\right)\right) - \ln\left(\tan\left(\frac{\varphi_i}{2}\right)\right) = -\frac{P}{l} \quad . \tag{2.8}$$

Solving equation (2.8) for φ as a function of P gives

$$\varphi(P) = 2\arctan\left(\frac{\sin\varphi_i}{1+\cos\varphi_i}\exp\left(-\frac{P}{l}\right)\right) \quad . \tag{2.9}$$

φ_i can be determined after rotating $(\mathbf{P}_i - \mathbf{S}_i)$ through α_i into the vehicle coordinate system by

$$\cos\varphi_i = \frac{(\mathbf{P}' - \mathbf{S}'_i)_x}{|\mathbf{P}' - \mathbf{S}'_i|} \quad , \qquad \sin\varphi_i = \frac{(\mathbf{P}' - \mathbf{S}'_i)_y}{|\mathbf{P}' - \mathbf{S}'_i|} \quad . \tag{2.10}$$

Combining equations (2.4), (2.5) and (2.9) allows to determine the tractrix $\mathbf{S}(t)$ between t_i and t_{i+1} with

$$\mathbf{S}_{i+1} = \mathbf{S}_i + \int_0^P \begin{pmatrix}\cos(\alpha_i + \varphi(P))\\ \sin(\alpha_i + \varphi(P))\end{pmatrix}\cos(\varphi(P))\,\mathrm{d}P \tag{2.11}$$

when $\mathbf{S}_i = \mathbf{S}(t_i)$ is known. Using this relationship, the $\mathbf{S}_i$ are successively calculated from a known initial position $\mathbf{S}_1$ of the sensor. In combination with section 2.2.1, the sensor positions $\mathbf{S}_i$ are obtained corresponding to the measured GNSS antenna positions $\mathbf{G}_i$.

2.2.3 Stiff or flexible connection between sensor and pivot

The above equations assume a stiff connection between the pivot at the drawing vehicle and the sensor, e.g. by a rod (figure 2.2a and b). They are also valid when the sensor is towed with a flexible connection (e.g. a rope) if the sensor is behind the vehicle (figure 2.2a). This is the predominant case in practice. In case of tight turns or backward movement of the drawing vehicle ($\varphi_i > 90°$), a flexible connection sags and the sensor stalls. This occurs when the pathway of the pivot runs within a circle around the sensor with radius l (figure 2.2c). Thus, $\mathbf{S}_{i+1} = \mathbf{S}_i$ for $|\mathbf{P}_{i+1} - \mathbf{S}_i| < l$.

If the straight line from $\mathbf{P}_i$ to $\mathbf{P}_{i+1}$ partly falls within that circle, then the movement of the pivot is decomposed in two parts (figure 2.2d). The first part, from $\mathbf{P}_i$ to $\mathbf{P}_i^*$, runs within the circle and causes no movement of the sensor (compare figure 2.2c). The second part, from $\mathbf{P}_i^*$ to $\mathbf{P}_{i+1}$ corresponds to the trailed sensor (compare figure 2.2a) and is treated as detailed in section 2.2.2 above. According to geometric consideration (figure 2.3), $\mathbf{P}_i^*$ is derived as

$$\mathbf{P}_i^* = \mathbf{P}_i - 2l\,\cos\varphi_i\,\frac{\mathbf{P}_{i+1} - \mathbf{P}_i}{|\mathbf{P}_{i+1} - \mathbf{P}_i|} \quad . \tag{2.12}$$

2.3 Model evaluation

2.3.1 Data collection

The model was applied to a survey of apparent electrical conductivity of the ground (σ_a). The survey was conducted at a 135 ha site, managed as 21 pastures and meadows on permanent grassland (for site and management conditions see Schnyder et al., 2006). The survey site exhibited spatial patterns in σ_a on a sub-field scale, thus providing adequate conditions to test whether the assessment of the spatial structures were improved by modelling the sensor positions.

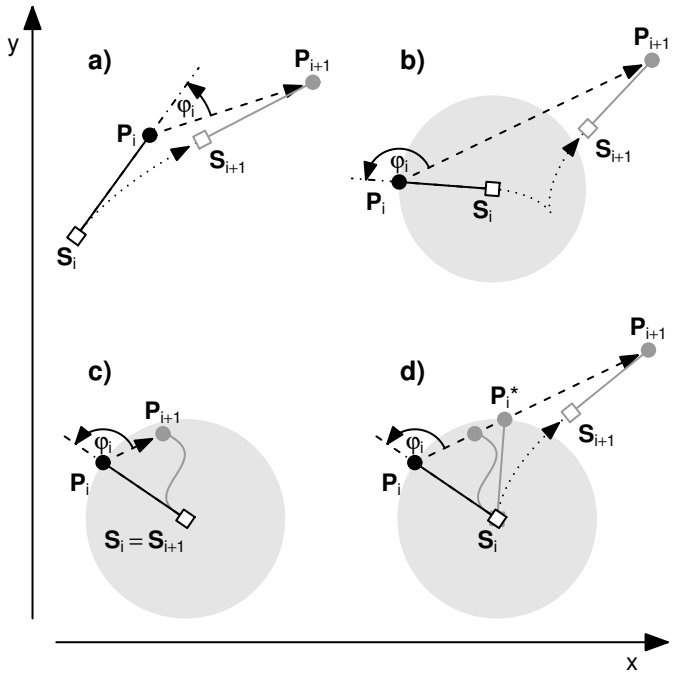

Figure 2.2: Potential pathways of a sensor towed to a vehicle at a pivot.
Solid lines represent the connection between vehicle and sensor (with length l), dashed lines represent the motion of the pivot between $\mathbf{P}_i$ and $\mathbf{P}_{i+1}$, and dotted lines represent the resulting motion of the sensor (tractrix) between $\mathbf{S}_i$ and $\mathbf{S}_{i+1}$. Positions subsequent to the initial position are plotted in grey. a) Usual forward driving (sensor behind pivot, $\varphi_i < 90°$). b-d) Tight turns or backward movement of the drawing vehicle ($\varphi_i > 90°$). In detail: b) Stiff connection (e.g. a rod) between sensor and pivot. c-d) Sensor attached to the pivot by a flexible connector (e.g. a rope). c) The pathway of the pivot runs within a circle around the sensor with radius l: the sensor stalls. d) The pivot pathway partly runs through the circle: this corresponds to c) for pivot movement between $\mathbf{P}_i$ and $\mathbf{P}_i^*$, and to a) for pivot movement between $\mathbf{P}_i^*$ and $\mathbf{P}_{i+1}$.

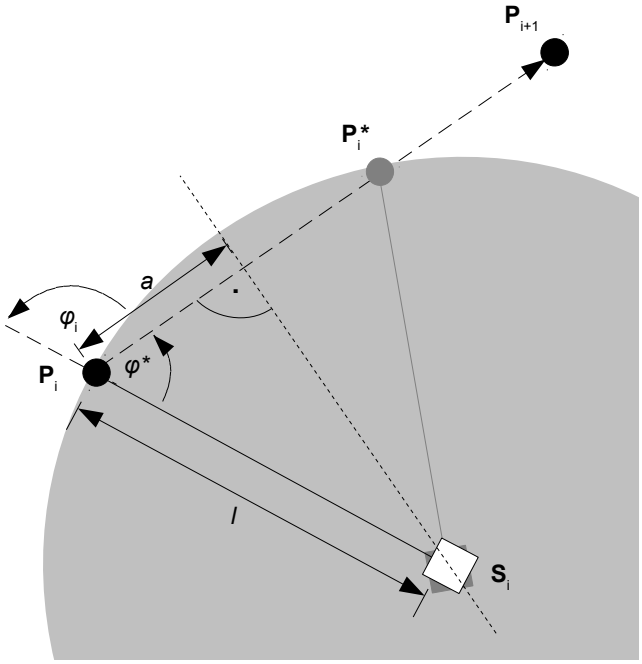

Figure 2.3: The figure shows a detail of figure 2.2d) with the geometric derivation of the intermediate pivot position $\mathbf{P}_i^*$.
$\mathbf{S}_i$, $\mathbf{P}_i$ and $\mathbf{P}_i^*$ span an isosceles triangle with side length l. This can be subdivided into two right-angled triangles with hypotenuse of length l. The side adjacent to φ^*, a, has length $l \cdot \cos\varphi^*$. Because $\varphi^* = \pi - \varphi_i$ and $\cos(\pi - \varphi_i) = -\cos\varphi_i$, it follows $2a = |\mathbf{P}_i^* - \mathbf{P}_i| = -2\,l \cdot \cos\varphi_i$. Multiplied with the unit vector in direction of $(\mathbf{P}_{i+1} - \mathbf{P}_i)$, this gives the vector $(\mathbf{P}_i^* - \mathbf{P}_i)$ and thus equation (2.12).

The σ_a measurements were conducted with an EM38 ground conductivity meter (Geonics Ltd., Mississauga, Canada), referred to as sensor in the following. The sensor was mounted in vertical orientation on a plastic sledge, towed by an agricultural tractor. The sledge was connected to the tractor by two ropes between the forehand edges of the sledge and the trailer coupling of the tractor. The offset between the trailer coupling and the centre of the sensor was 3.25 m, to avoid interference of the sensor with metallic parts of the vehicle. The sensor was kept under a wooden box to avoid bias due to instrument heating by sunlight (Robinson et al., 2004). The antenna of a differential GPS receiver (Trimble AgGPS) was mounted on the roof of the tractor. The horizontal offset between the GNSS antenna and the trailer coupling was 2.25 m longitudinally and 0 m laterally. GNSS antenna positions and sensor data were collected synchronously on each field at a frequency of 1 Hz. In total, 103 867 individual measurements were taken in the study area. With the vehicle driving at typically 7 km h^{-1} to 17 km h^{-1} (2 m s^{-1}

to 5 m s^{-1}), the typical distance between successively measured positions ranged between 2 m and 5 m. The spacing between adjacent passes was typically 3 m to 5 m and curve radii were about 2 m to 6 m. The geodetic output coordinates from the GNSS receiver were projected into a Gauß-Krüger coordinate system, corresponding to the field coordinate system mentioned in section 2.2

Soil temperature was measured at each field at the time of σ_a measurement and the measured values of σ_a were converted to σ_a at a reference temperature of 25 °C according to Sheets and Hendrickx (1995). In the following the apparent conductivity at the reference temperature is referred to as σ_a. In order to quantify instrument drift (Corwin and Lesch, 2005b), two measurements of σ_a were taken at the same location at the beginning (after calibration) and at the end of each measurement day. Individual measurements were corrected according to the assumption of linear drift over time (details of temperature and drift correction are given by Gottfried, 2008). Measurements with negative value, deviating more than four times the standard deviation from the overall mean or showing artefacts (e.g. derived from electric fences along field borders) were considered erroneous and excluded from further analysis.

2.3.2 Data filtering and model application

Errors in GNSS receiver measurements (Ganskopp and Johnson, 2007; Hurford, 2009) lead to scatter in the recorded pathway. As a result, the direction of vectors between subsequently measured positions deviates from the true pathway direction (Hurford, 2009). Such a discrepancy would lead to erroneous estimates of the sensor positions. Thus, the measured positions were filtered to smooth out scatter. For this purpose, the precision of the GNSS data was assessed from stationary GNSS measurements over longer periods of time (10 min to 1 h). The distribution of a total of 79 065 measurements was assessed, taken at 62 locations in the study area. The 95 % quantile of distances to the long-time mean positions of the stationary measurements was 1.36 m. This distance was the maximum distance for which two successive positions were considered colocated (minimum distance threshold (Ganskopp and Johnson, 2007); figure 2.4). For points considered colocated, the coordinates and sensor data of both positions were replaced by the respective means. The distance between the resulting mean position and the subsequent positions was again compared with the threshold distance and the procedure iteratively applied to all successive pairs of positions.

Distances >10 m between successive positions along the GNSS antenna pathway imply a velocity of the drawing vehicle of >10 m s^{-1} (>36 km h^{-1}). Since such high velocities did not occur in reality, a failure of the GNSS receiver was supposed. The corresponding pairs of positions were omitted and the filtered data split at these locations resulting in 39 subsets of the pathway with the distance between all successive positions <10 m. The model was applied to the individual subsets. For each subset, the initial sensor position was estimated by

$$\mathbf{S}_1 = \mathbf{P}_1 - l \begin{pmatrix} \cos\alpha_1 \\ \sin\alpha_1 \end{pmatrix} \quad . \tag{2.13}$$

All data were handled and the model was implemented in R (R Development Core Team, 2012) and PostgreSQL/PostGIS (www.postgresql.org, www.postgis.org).

2.3.3 Geostatistical analysis

The raw (unfiltered) GNSS antenna positions were not considered during geostatistical analysis, as the differences between raw and filtered positions comprised only a small fraction of the data (2 %) and were regarded to be solely due to imprecision of the GNSS positioning. Thus, the filtered GNSS antenna positions are referred to in the following as GNSS positions.

To quantify the effect of sensor position modelling on the apparent spatial structure of σ_a and the variance at the measurement position (nugget effect), semivariograms were calculated

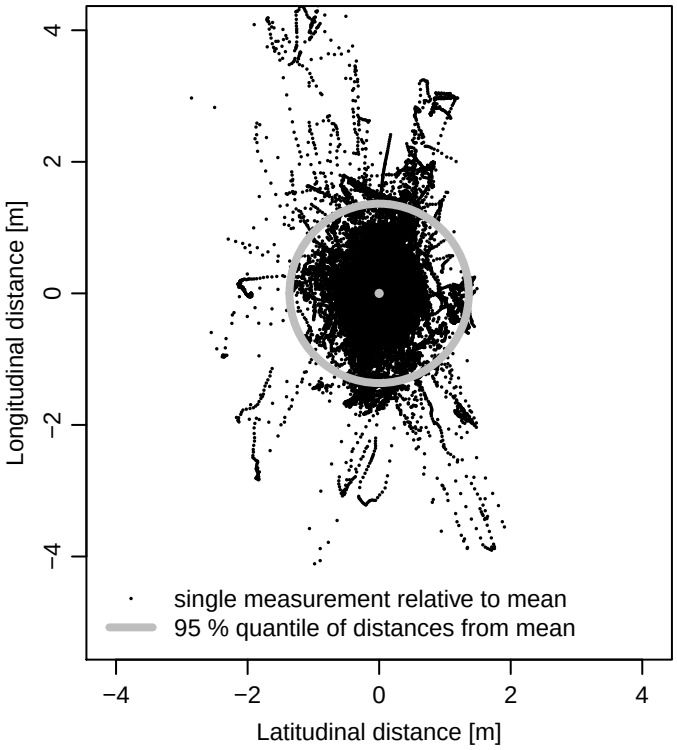

Figure 2.4: Precision of GNSS measurements.
79 065 measurements relative to the mean position of a stationary GNSS antenna placed at 62 positions in the study area. 150 measurements (0.2 %) deviated more than 4 m (maximum 34 m) from the mean and are not shown.

(Goovaerts, 1997; Sudduth and Drummond, 2007) with GNSS positions and modelled sensor positions respectively up to a lag of 22 m, which is 4 times the overall offset between the GNSS antenna and the sensor. For curved pathways in particular, the model performance was assessed by manually defining areas where turning of the vehicle occurred (so-called 'headland area', figure 2.5). Semivariograms for all positions in the headland area were calculated as for the total area. Further, anisotropic experimental semivariograms were calculated (Zimmerman, 1993) in driving direction and perpendicular to it from all positions in an area that has been measured by driving on parallel passes. These are adequate to illustrate the direction dependent nature of the artefacts introduced in the spatial structure by the offset between GNSS antenna and sensor when data are recorded in opposing direction on adjacent passes.

To assess the improvement by the modelling of sensor positions for the prediction of individual σ_a measurements, a kriging-based cross-validation approach was chosen similar to that applied by Simbahan et al. (2004). As the kriging equations imply that all positions are unique, σ_a measurements at duplicate positions were replaced by their mean for all geostatistical procedures. The kriging was carried out for the whole dataset and for the headland area respectively with both the GNSS positions and modelled sensor positions, thus for a total of four datasets. Kriging was performed with a neighbourhood with radius of 22 m. For this purpose, Gaussian semivariogram models were fitted to the experimental semivariograms of all datasets (figure 2.6). Cross-validation was applied as implemented in the gstat package (Pebesma, 2004) in the R software environment (R Development Core Team, 2012). Each dataset was divided into ten subsets of randomly chosen locations. Prediction of σ_a at the locations from an individual subset was done by kriging with the data from the remaining nine subsets. For each subset, the root mean squared error (RMSE) was then calculated from the predicted and measured values of σ_a. The relative error was calculated by

$$\eta = \frac{\bar{\epsilon}_\mathrm{G}}{\bar{\epsilon}_\mathrm{S}} \quad , \tag{2.14}$$

where $\bar{\epsilon}_\mathrm{G}$ denotes the mean RMSE of the ten subsets from GNSS positions and $\bar{\epsilon}_\mathrm{S}$ denotes the mean RMSE of the ten subsets from modelled sensor positions. A Welch-test (t-test with

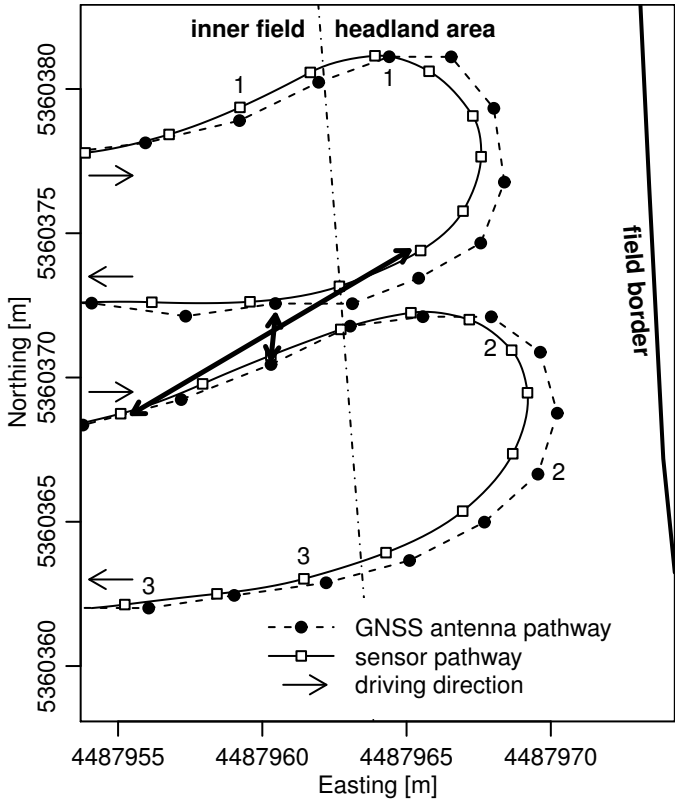

Figure 2.5: Pathways of GNSS antenna and sensor.
Filtered GNSS antenna positions and modelled sensor positions on part of a field with the headland area along the field border. Three corresponding antenna and sensor positions are indicated with the same number. Bold arrows illustrate an example of a pair of positions with a small apparent lag of the GNSS positions and a true lag of approximately two times the offset between the GNSS antenna and the sensor.

variances assumed to be unequal) was used to compare the mean RMSEs from the subsets from GNSS positions and modelled sensor positions.

2.4 Results

2.4.1 Data collection and filtering

In the soil electrical conductivity survey, σ_a ranged from 7.6 mS m^{-1} to 61.3 mS m^{-1}. 103 867 measured positions on 135 ha were obtained, and thus a surface density of 765 positions per hectare. 1806 measured positions were averaged because they were located within the threshold distance of 1.36 m for successive measurements. This resulted in 189 filtered GNSS positions. They corresponded to locations where the vehicle had stopped or had driven very slowly. In total, the filtering procedure left over 101 960 positions (98.2 % of the total dataset).

The average distance between nearest neighbour positions (mean shortest distance), irrespective if recorded successively or not, in the filtered dataset was 2.76 m (table 2.1). The selected headland area covered 3.7 ha and included 5235 measured positions. Thus, it showed 1419 positions per hectare, with a mean shortest distance of 1.48 m. The distance between

Table 2.1: Cross-validation for the total area and the headland area with filtered GNSS positions or modelled sensor positions.

Coordinate quality	total area				headland area			
	$\bar{h}_{ij}$[a] [m]	$\bar{\epsilon}$[b] [mS m^{-1}]	η[c] [%]	p[d]	$\bar{h}_{ij}$[a] [m]	$\bar{\epsilon}$[b] [mS m^{-1}]	η[c] [%]	p[d]
filtered	2.76	1.52	133		1.48	1.83	149	
modelled	2.76	1.14		<0.01	1.46	1.23		<0.01

[a] Mean shortest distance
[b] Mean root mean squared error (RMSE) of cross-validation
[c] Error of σ_a predicted with GNSS antenna coordinates relative to predicted with modelled sensor positions (equation (2.14))
[d] Probability that $\bar{\epsilon}_G$ and $\bar{\epsilon}_S$ do not differ (obtained by a Welch-test)

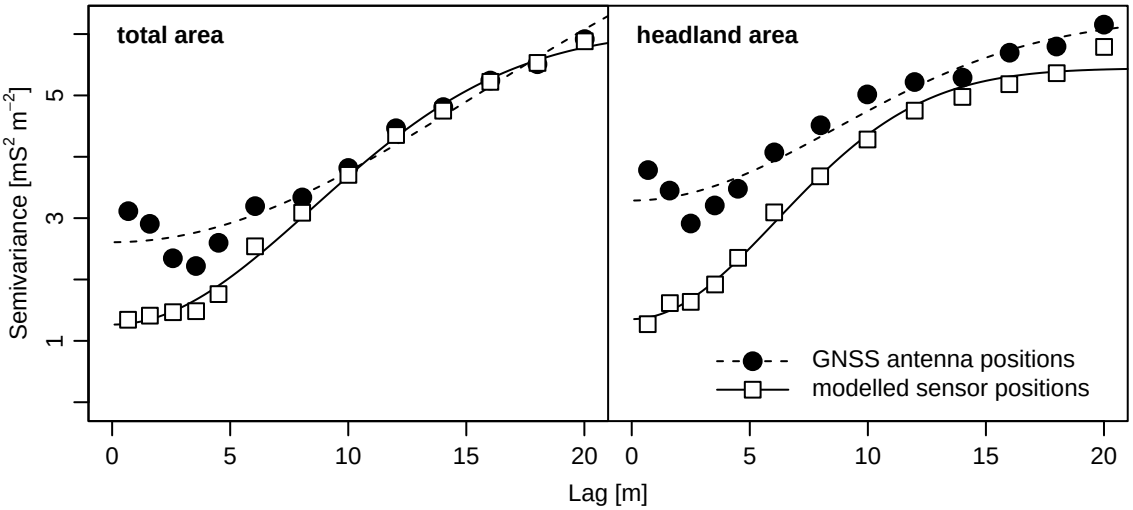

Figure 2.6: Semivariograms for the total study area and headland area.
Experimental semivariograms (markers) calculated with (1) filtered GNSS antenna positions and (2) modelled sensor positions. Gaussian semivariogram models (lines) were used for a kriging-based cross-validation of the modelling of sensor positions.

positions on the headland area was less than on the total area due to overlapping pathways and the fact that driving velocity was smaller in curves.

The modelled sensor positions yielded a realistic pathway of the sensor with respect to the pathway of the GNSS antenna even during turns at the field borders (figure 2.5): The modelling predicted that the sensor moved slightly outside of the GNSS antenna pathway where the vehicle started a turning operation due to the deflection of the trailer coupling towards the exterior of the curve (figure 2.5, example 1; pathway of trailer coupling not shown). During the turning operation itself, the sensor pathway followed a narrower curve radius than the GNSS antenna (figure 2.5, example 2). Both pathways were in line while driving straight (figure 2.5, example 3). However, during straight driving the largest offset between the modelled sensor position and the GNSS position occurred. It equalled the sum of the offsets between GNSS antenna, trailer coupling and sensor (5.5 m). For measurements in adjacent passes, the driving directions and hence the offset directions were usually opposite. Then, the mismatch between the locations of two measurements was approximately twice the offset between sensor and GNSS antenna (figure 2.5, bold arrows).

2.4.2 Semivariogram analysis

The number of pairs of positions per lag ranged roughly from 260 000 to 860 000 for the total area and from 14 000 to 24 000 for the headland area for lag classes > 5 m. For lag classes < 5 m, the corresponding ranges are from 3500 to 265 000 for the total area and from 780 to 16 800 for the headland area.

Experimental semivariograms derived from GNSS positions (figure 2.6, closed circles) showed a decrease in the semivariance with increasing lag up to approximately 3 m, indicating that σ_a measurements within a distance of approximately 3 m correlated closer than those within shorter distances. In contrast to semivariograms derived from the GNSS positions, the semivariograms derived from the modelled sensor positions (figure 2.6, open squares) showed the expected increase in semivariance with increasing lag. Also, the nugget variance was improved and became half of that calculated with the GNSS positions (1.3 $mS^2\,m^{-2}$ vs. 2.6 $mS^2\,m^{-2}$ in the Gaussian semivariogram models for the total area, 1.6 $mS^2\,m^{-2}$ vs. 3.3 $mS^2\,m^{-2}$ for the headland area).

When anisotropy was considered, the mean semivariance for lags < 6 m calculated from GNSS positions was 1.2 $mS^2\,m^{-2}$ in driving direction (along-pass), while it was increased (2.4 $mS^2\,m^{-2}$) perpendicular to the driving direction (cross-pass; figure 2.7, closed circles). At the same time, the mean semivariance for lags < 6 m derived from modelled sensor positions was similar in driving direction and perpendicular to it (1.0 $mS^2\,m^{-2}$ vs. 1.2 $mS^2\,m^{-2}$; figure 2.7, open squares).

2.4.3 Cross-validation

The RMSEs of cross-validation with GNSS positions (1.52 $mS\,m^{-1}$ and 1.83 $mS\,m^{-1}$ for total and headland area) were similar to the accuracy of the sensor (given for the EM38 as ±5 % at 30 $mS\,m^{-1}$, which equals 1.5 $mS\,m^{-1}$ (Geonics Limited, n.d.); table 2.1). This indicates a high quality of the measurements. Still, the RMSE for the modelled sensor positions was significantly smaller ($p < 0.01$) than for the original GNSS positions for both total and headland area. The prediction error η was 30 % to 50 % higher for GNSS positions than for modelled sensor positions. The relative improvement by using modelled sensor positions instead of GNSS positions was more pronounced on the headland area than in the total area, although the prediction was less accurate in absolute terms (see higher RMSE and higher η on headland area in table 2.1).

2.5 Discussion

2.5.1 Model evaluation

The model substantially decreased the systematic positioning bias due to an offset between a GNSS antenna and a sensor towed by a vehicle, as shown by the reduction of nugget effect (figure 2.6), directional dependence of the nugget (figure 2.7) and interpolation error (table 2.1). As shown by the analysis of headland area, the improvement occurred also for curved pathways. Anisotropic artefacts introduced by the offset on parallel passes were removed by the modelling too.

Mainly, σ_a was measured along adjacent passes but in alternating direction. Therefore, for the GNSS positions, the measured and real distance of two positions lying on adjoined opposing passes differed by about two times the offset between GNSS antenna and sensor (illustrated

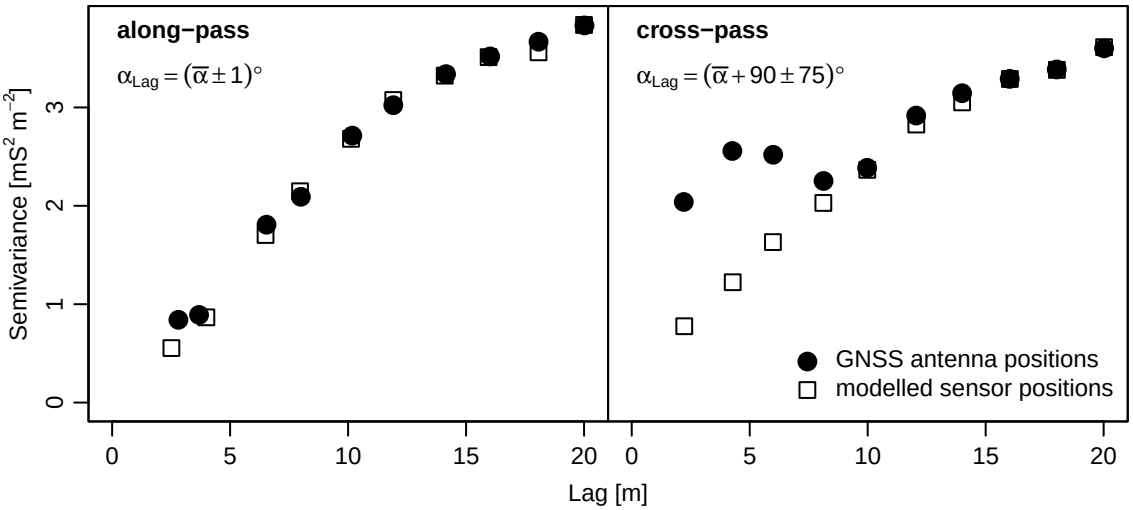

Figure 2.7: Anisotropic semivariograms from parallel passes on three approximately rectangular fields (excluding headland area).
The left panel shows the anisotropic semivariogram in mean driving direction ($\bar{\alpha}$) with a small tolerance to ensure that only pairs of positions are included that lie on the same pass (6 % of total 485 000 pairs of positions). The right panel shows the anisotropic semivariogram perpendicular to $\bar{\alpha}$.

by bold arrows in figure 2.5). Such a systematic shift converts the real small-scale pattern into a pattern, where a shifted measurement on the neighbouring pass has similar properties while the direct neighbour is at larger contrast. This displacement happens only between neighbouring passes while the data along a pass—although wrongly positioned in absolute terms—are correctly positioned relative to one another. Thus, the semivariance in lag classes, that comprise to a large extent pairs of positions, whose GNSS positions lie in proximity on adjoined opposing passes, was artificially increased. This is consistent with two other findings. First, the semivariance at short lags in the headland area was larger than for the total area, because on the headland area also successive measurements on the same pass were displaced relative to one another (figure 2.6). Second, the along-pass anisotropic semivariance, for which the GNSS positions were correct relatively to one another even though the absolute positions were wrong, was nearly identical when derived from both GNSS positions and modelled sensor positions (figure 2.7, left panel). This agreed with the fact that a constant offset along straight passes cannot appear in the anisotropic semivariance along the same direction but in the semivariance perpendicular to the driving direction. This apparent anisotropic spatial process (i.e. the offset) was superposed to the real spatial pattern of the measured variable (Zimmerman, 1993). Consequently, the artefacts introduced in the spatial autocorrelation structure of the measured variable were effectively eliminated by removing the offset from the data by applying the model (figure 2.7). A similar effect can be achieved for a temporal offset by correction for the delay between position and attribute measurement: Sudduth and Drummond (2007) demonstrated the elimination of a characteristic saw-tooth pattern at the limit between areas of contrasting attribute level in a yield map. The semivariograms, they show, exhibit similar patterns at short lags as in the present study, though these might also derive from various other filters they applied.

The spatial interpolation of measured data by kriging relies on information about the spatial structure of the measured variable. In case the spatial structure cannot be reliably determined, accuracy of the interpolation is affected (Kravchenko, 2003). An offset between the positions measured with a positioning system and the true positions of related sensor data perturbs the spatial structure of the measured variable, as shown above. Consequently, interpolating such data without correcting for the offset will result in relatively inaccurate predictions of the variable at unsampled locations. This is in line with the results, showing higher prediction accuracy obtained from kriging with the same dataset, but after correction for the offset. The improvement due to using modelled sensor positions instead of GNSS positions was larger in the headland area. This is in line with the semivariograms, which also exhibited a larger artefact due to the offset on the headland area. It can again be explained by the fact that—on the headland area—also successive measurements were displaced relative to one another.

2.5.2 Possible generalisations

The design of the model relies on several conditions that might not be applicable in all cases. Necessary considerations and solutions for more general conditions will be discussed in the following.

(i) Only the spatial offsets between components of the system was taken into account, requiring measurements of GNSS receiver and sensor to be synchronous. This is hardly ever the case in a true sense due to time lags in the electronics used for data acquisition. Sudduth et al. (2001) experienced a time lag of 0.28 s, which would imply a smaller but still considerable spatial offset of 0.6 m to 1.4 m at typical operating speed in the survey. Possibilities to take this additionally into account are given by Sudduth et al. (2001).

(ii) Potential tilting of the vehicle in hilly terrain might introduce an additional positional error. In the present study, the slope computed from a digital elevation model (2 m$\times$2 m grid)

was on average 1° and 95 % of the slopes were < 2°. As the GNSS antenna was mounted at approximately 3 m above ground, the given 95 % quantile-slope corresponds to an horizontal offset of the measured positions of 0.1 m. Thus, tilting was negligible in the present study, since the terrain was sufficiently flat. Where this is not the case, the tilting can be coped with either statistically (Tantum et al., 2003) or analytically (Speckmann, 2000).

(iii) In the presented survey, curve radii were typically 2 m to 6 m and distances between successive positions were 2 m to 5 m, with a trend to lower values in curves due to lower velocity. Thus, distances between successive positions were smaller than curve radii leading to good representations of the pathway by the discrete measured positions. Therefore, approximating the GNSS pathway by straight lines and the estimation of vehicle heading at measured positions was justified. Nevertheless, other positioning technologies (i.e. vehicle dynamic sensors) can provide heading information at much higher frequency compared to GNSS (Hague et al., 2000; Skog and Händel, 2009) and could help to record curved pathways much more accurately. The bias towards the inside of a curve, introduced in the modelled coordinates due to approximating the GNSS pathway by straight lines, would thus be reduced. However, the geostatistical analysis indicated that potential improvements would be small. Additionally, the need for heading data at measured positions can be avoided if the GNSS antenna is located on top of the pivot. Then the positions of the pivot are known and need not to be estimated by the model. However, if mounting the GNSS antenna on top of the pivot is not applicable (Speckmann, 2000), the presented equations provide the means to model correct sensor positions.

(iv) In case GNSS positioning is of insufficient quality or unavailable, then navigation techniques such as dead reckoning (Reitz and Kutzbach, 1996) or the combination of several GNSSs (such as the American Global Positioning System (GPS), Russian Globalnaja Nawigazionnaja Sputnikowaja Sistema (GLONASS), the Chinese system Compass and the upcoming European system Galileo) may provide appropriate input coordinates to the model. Combining data of several sensors into a single position estimate through the use of e.g. a Kalman filter can directly provide position estimates with quantifiable reliability (Hague et al., 2000; Skog and Händel, 2009; van Bergeijk et al., 1998) but is more demanding in implementation than the simple filtering algorithm presented in section 2.3.2. Further, positional uncertainty can be taken into account geostatistically (Cressie and Kornak, 2003), or be improved by statistical post-processing (Tantum et al., 2009; Tarokh and Miller, 2007).

(v) The sensor movement is derived from kinematics without explicitly describing the forces, which cause the movement. Thus, any forces not implicitly incorporated in the kinematic description have to be negligible to obtain accurate model results. Among these forces are centrifugal forces in curves and—in case of a flexible connection between pivot and sensor—inertia during braking. Both can be easily controlled by driving sufficiently slow (Garlick et al., 1993). However, on sloping land gravity may become important if it causes the sensor to drift downhill, especially if mounted on a sledge.

(vi) The accuracy of a modelled sensor position depends on the accuracy of two subsequently measured positions and the previously modelled sensor position. The former can be considered as unbiased, besides possible bias as discussed in items (i), (ii) and (iv) of this section and correlation in space and time which is inherent to positions derived from dead reckoning (Hague et al., 2000) and can be due to build in filters of the GNSS receiver (Skog and Händel, 2009). A bias as discussed in items (iii) and (v) is inherent to the model and accumulates throughout a curve because of the dependence of each

modelled position on its predecessor. Apart from what has been mentioned in items (iii) and (v) considering avoiding such a bias, it is eliminated when driving straight and thus can be expected to not accumulate throughout the measurements on a complete field in practical applications.

2.5.3 Potential applications

Conceivable applications of the model occur in many fields of research and practice. Sensor based soil mapping for research applications or precision agriculture requires sufficient positional accuracy, if spatial patterns on a local or sub-field scale are to be mapped or discontinuities are relevant to improve geostatistical interpolation (Sinowski and Auerswald, 1999). The same applies to the detection of buried objects (Nelson and McDonald, 2001) or archaeological features with several decimetres radius (Hejcman and Smrž, 2010) in high-resolution sensor-based mapping (Ciminale et al., 2009).

In the technical framework of precision agriculture, an implementation for mapping or real-time applications (Adamchuk et al., 2004; Auernhammer, 2001) and integration with other technologies is conceivable (Peets et al., 2012; Speckmann, 2000; Speckmann and Jahns, 1999). The correction for positional offset is particularly useful in case where multiple sensors are mounted at different locations on agricultural machinery in conjunction with a GNSS receiver (Speckmann, 2000). Further, it is particularly relevant on small-sized fields with non-rectangular shape as frequently found in Europe.

Though the concept of tractrix has been used for the prediction of vehicle offtracking (Erkert et al., 1989; Garlick et al., 1993; Sayers, 1991; Torisu et al., 1992), the benefits of this concept for on-the-go sensor applications and mapping have not yet been investigated. The requirements of the model for input data and application are simple. Knowledge of the GNSS antenna positions and the geometric configuration of GNSS antenna and sensor relative to the vehicle are sufficient to estimate the real positions of the sensor, even retrospectively. In case of unknown offset between GNSS antenna and sensor, the offset with maximum correlation between neighbouring sensor values on adjacent passes may be estimated (Lark et al., 1997) and used in the model.

2.6 Conclusions

The kinematic model proved to be a useful tool for the estimation of sensor positions from measured GNSS positions in on-the-go applications. It reduced the apparent measurement error as quantified by the nugget effect in a geostatistical analysis by a factor of two. This offers the possibility to improve the quality of high resolution digital mapping. The application of the model is possible even to existing datasets. In particular, practical applications and the simultaneous use of different sensors can benefit from the realistic correction of the offset between sensors that are mounted at different positions to agricultural machinery. In addition, the suggested extensions to more general conditions will facilitate further improvement of positional correction.

3 Spatial and temporal variation of a shallow unconfined groundwater table

3.1 Introduction

Groundwater and landuse are linked through geochemical, ecological and production cycles. In these, groundwater is integrated as a source and sink, not only for the water itself but also for other substances such as pollutants. The coupling to processes occurring in and above the soil is especially tight for unconfined aquifers with a shallow water table. Thus, rapid responses of NO^3-concentrations to fertiliser applications can be found (Baker and Johnson, 1981), water tables can respond to evapotranspiration (Rosenberry and Winter, 1997), and the proximity of the water table can have an effect on plant growth (Brolsma et al., 2010; Schmidhalter and Oertli, 1993). For shallow groundwater tables, the closeness to the soil surface leads to a relative importance of local topography for variation in table depth, if the water table is not a subdued replica of the topography, which would only be the case for aquifers with especially low permeability (Haitjema and Mitchell-Bruker, 2005). Thus, spatial variability occurs in the links between groundwater and surface such as recharge or penetration depth of contamination (Böhlke, 2002).

A dominant landuse affecting groundwater fluxes and geochemistry, e.g. by irrigation, drainage and nitrate contamination, is agriculture (Böhlke, 2002; Skaggs et al., 1994). Here the tight coupling of shallow groundwater emerges in higher risk of pollution (Nolan, 2001), direct interaction with irrigation and drainage (Böhlke, 2002), direct relevance in water availability for plants (Raes and Deproost, 2003; Schmidhalter and Oertli, 1993) and in turn possible modification of the table by consumption (Rosenberry and Winter, 1997).

Studying the interactions of shallow groundwater with numerous processes at local scale and with high temporal resolution requires accordingly resolved information on the water table. But table height data are often especially sparse in space due to the high cost of wells (Buchanan and Triantafilis, 2009; Rouhani and Myers, 1990) though relatively abundant in time (Rouhani and Myers, 1990). Mere spatial interpolation of the available data leads to mapping results that do not represent the actual local variability (Buchanan and Triantafilis, 2009) and fails to reproduce physical properties (Rivest et al., 2008). Therefore numerous attempts exist in the literature to overcome this shortcoming. Auxiliary data have been used in the prediction of the water table in a Bayesian framework (Fasbender et al., 2008) or as covariables in geostatistical interpolation (Finke et al., 2004) or regression models (Buchanan and Triantafilis, 2009; Schumann and Zaman, 2003). The use of conceptual knowledge about the flow of groundwater has been incorporated in spatial predictions as well (Peeters et al., 2010; Rivest et al., 2008; Tonkin and Larson, 2002). For temporal interpolation, weather data have been used in time series analysis as auxiliary variables (Finke et al., 2004; Knotters and Bierkens, 2000). Spatio-temporal geostatistical interpolation of residuals from a trend model obtained with spatial auxiliary data allowed for producing maps of seasonal groundwater fluctuations (Hoogland et al., 2010). The use of landuse parameters to aid in the prediction of water table included parameters such as the local density of the drainage network and distance to local ditches (Finke et al., 2004). Drainage ditches are known to lower groundwater decreasingly with distance from the ditch. This fact has been shown theoretically (Skaggs et al., 2005) and experimentally (Hayes Jr. and Vepraskas, 2000; Phillips et al., 2010).

It is hypothesised that incorporating distance to the nearest ditch in a physical conceptual model of the water table of a shallow unconfined aquifer improves modelling results and thus the spatial prediction of the water table from spatially sparse data. In order to test this hypothesis a physical conceptual model was built of a shallow unconfined water table incorporating regional scale and drainage ditch induced gradients as well as seasonal fluctuations. The performance of the model was assessed by geostatistical analysis of the residuals.

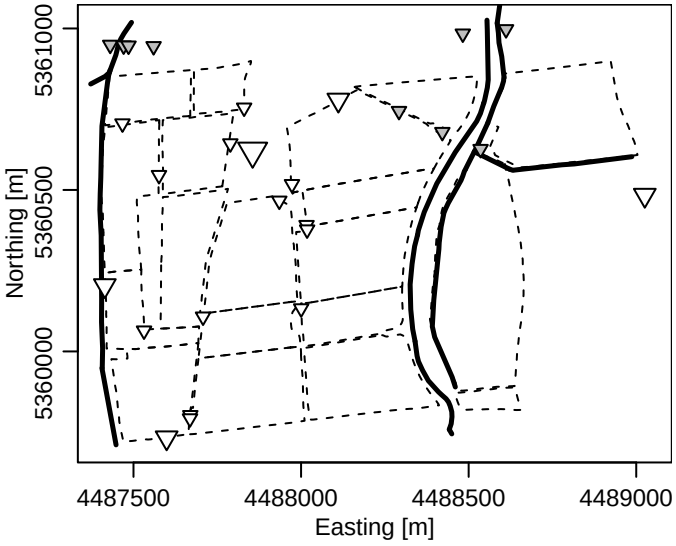

Figure 3.1: Map of the study site, showing the arrangement of pastures and meadows (dashed polygons), the locations of 27 wells (triangles) and the ditches that drain the area (bold lines). Wells have hourly (large triangle), weekly (medium triangles) and monthly (small triangles) resolution. At some wells time series are available for the second half of the hydrological year only (grey triangles). Coordinates refer to a common Gauß-Krüger projection for south-west Germany (central meridian 12°, Potsdam datum).

3.2 Material and methods

3.2.1 Study site

The present study has been undertaken on Grünschwaige research station, a 135 ha site, managed as 21 pastures and meadows on permanent grassland (for site and management conditions see Schnyder et al., 2006). The site is located at the north edge of the Munich gravel plane, consisting of quaternary glacial deposits, partly covered by peat in the area of the study site (Haunschild, 1981). The thickness of the gravel is approximately 10 m and up to 20 m in troughs originating from former river valleys. A 10 m to 15 m thick unconfined aquifer is located within the gravel, flowing in north-north-eastward to northward direction on the underlying tertiary molasse, which exhibits a slope of approximately 3 ‰ (Traub, 1956). In the south of the site is located an airport under which groundwater is technically lowered and reinjected to the aquifer north of the two southernmost fields of the study site. These two fields have thus been excluded from the analysis leaving an area of 116 ha of the study site. Natural and artificial ditches, that cross and surround the area (figure 3.1), drain into the river Isar, which flows approximately 3 km north of the site from west to east.

3.2.2 Data acquisition

Table height was measured at 27 wells placed across the study site. The data used in the present study were of the hydrological year November 2000 to October 2001. This year proved to be typical based on data of a well in the centre of the study site for which at least weekly data exist for a 40 year period (figure 3.2). At this well, hourly measurements were undertaken and aggregated as daily averages. Weekly time series were generated at four wells and at another thirteen wells measurements were taken at approximately monthly intervals (figure 3.1). At nine wells also approximately monthly time series were generated but starting only from June.

A high resolution (2 m×2 m grid) digital elevation model (DEM) from the Bavarian land surveying office was used to derive land-surface height. The network of ditches was partly also taken from the Bavarian land surveying office and partly digitised based on knowledge of the site conditions and orthophotos (figure 3.1). Distance to the nearest ditch was calculated as the 2 dimensional Cartesian minimum distance between any location and the set of lines representing the ditches.

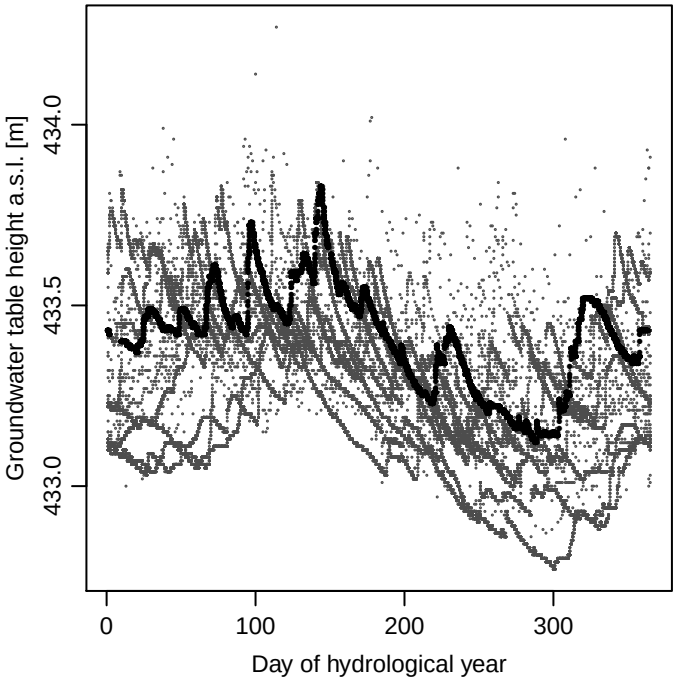

Figure 3.2: Weekly up to hourly table height data from the years 1969 to 2011 from a well near the centre of the study site (large triangle in figure 3.1). Hourly data from the hydrological year 2001 are plotted in black over the grey dots representing the complete dataset.

3.2.3 Water table model

Adopting the Dupuit assumptions that flow occurs horizontally at each point and is in each vertical section proportional to the thickness of the saturated aquifer, according to Darcy's law, groundwater discharge can be written as

$$Q = -hK\frac{\mathrm{d}h}{\mathrm{d}l} \quad , \tag{3.1}$$

with h the hydraulic head, K hydraulic conductivity and l the distance in flow direction. Integrating and rearranging this gives

$$h = \sqrt{\frac{-2Q}{K}l + c} \quad , \tag{3.2}$$

indicating a parabolic shape of the water table of an unconfined aquifer with parallel flow (Hiscock, 2005).

Thus, assuming a regional flow system with a seepage point at unknown distance, a local system of flow towards ditches, both with parallel flow, and a sinusoidal seasonal fluctuation, table height is expressed as

$$h = \sqrt{\beta_1\, l + \beta_2} + \sqrt{\beta_3\, d} + \beta_4\, \sin(\omega t + \beta_5) + \beta_6 \quad , \tag{3.3}$$

where the first summand captures the regional scale, the second the local scale and the third the seasonal scale. In the equation h denotes table height, l the distance in regional flow direction, d the distance to the nearest ditch, t time, ω the period of one year and β_i an optimal parameter set obtained by a non-linear least-squares fit against the measured values of table height. β_1, β_3 and β_4 capture the variability of the data caused by the respective independent variable and β_2, β_5 and β_6 are needed because l, t and h are given on interval scales. This is because no previous knowledge is assumed about the location and height of the seepage point of the regional flow system nor on any zero of the sine and h is given as height above sea level (a.s.l.). The event scale (weather) was not included in this model as prediction of rain events is not possible. It was thus assessed as the outcome of a random function in time domain and interpolation was performed by means of colocated cokriging, using the data of the well with daily values as secondary variable (see section 3.2.4).

3.2.4 Model performance

The model was cross validated against each measured datum by predicting this datum with the model parameterised with the dataset reduced to data not originating from the same location or time as the predicted datum.

To quantify possibly unexplained temporal or spatial patterns in the dataset not captured by the model, a geostatistical analysis of the model residuals was performed in time domain as well as in space domain. The temporal structure of the model residuals was assessed by a pooled experimental semivariogram and a fitted semivariogram model. Pooling was done by location, thus considering only point pairs with both points originating from the same location. This allowed excluding any spatial effect from the analysis of the temporal structure. The spatial structure was equally assessed by a pooled experimental semivariogram and a fitted semivariogram model. Here, pooling was done by time, allowing for the exclusion of temporal effects from the analysis of the spatial structure.

As the model residuals were temporally and spatially structured, temporal and spatial interpolation was applied to obtain a full spatio-temporal coverage of model residuals. In order to represent the event scale, temporal interpolation was implemented for each location by colocated cokriging (Bivand et al., 2008) with the time series of daily values as secondary variable. The neighbourhood was restricted to 10 points for the primary variable to reduce computing time. The usage of the daily time series as covariable was justified as for the porous gravelly aquifer a high transmissivity could be assumed (Bundesanstalt für Geowissenchaften und Rohstoffe, 2008) and thus the temporal patterns at all wells should correlate. Linear regressions between synchronous residuals from the time series of daily values and all other time series were performed to verify this assumption. Colocated cokriging was chosen because it is favourable if secondary data are exhaustively available and no physical relationship is established between primary and secondary variable (Goovaerts, 1997). Spatial interpolation of model residuals was implemented by ordinary kriging of the temporally interpolated residuals of any specific time, thus allowing for a full spatio-temporal coverage.

The temporal interpolation of residuals at each location was evaluated by leave-one-out cross-validation (Bivand et al., 2008) and the obtained residuals were aggregated into root mean squared error (RMSE). The quality of the spatial interpolation of temporally interpolated residuals was evaluated exemplary for 2001-02-15 and 2001-07-15 by leave-one-out cross-validation and the so obtained residuals were merged and aggregated into one RMSE.

To assess a possible benefit of residual interpolation for table height mapping, the conceptual model and the temporal and spatial interpolation were jointly cross validated, too. To this end, every measured datum was predicted with the conceptual model and residual interpolation, using the dataset reduced to data not originating from the same location nor the same time as the predicted datum.

3.3 Results

3.3.1 Site characteristics

Distance from each well to the nearest ditch varied between 10 m and 451 m. The variation in the DEM could be explained to 89 % by a first-order trend surface with a south-north slope of approximately 3 ‰. Thus, local topography within the extend of the study site was only 11 % of the regional trend in land-surface height.

3.3.2 Water table model

Figure 3.3 shows the hydrographs for the hydrological year 2001 for all wells installed at the study site. The differences in mean table height between the wells were associated to spatial variation.

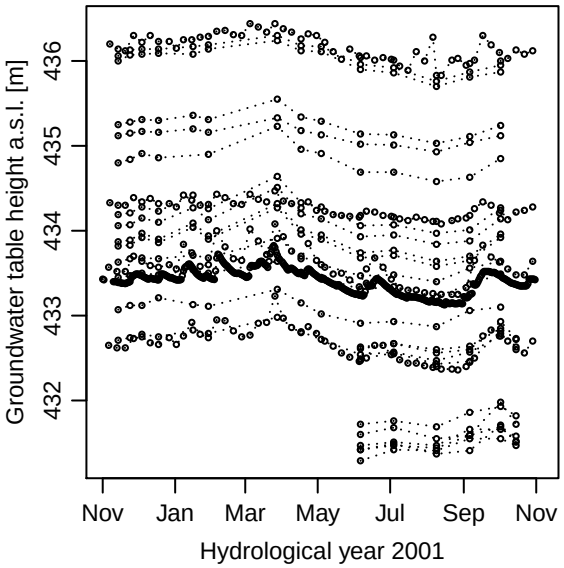

Figure 3.3: Hydrographs of all wells for the hydrological year 2001.

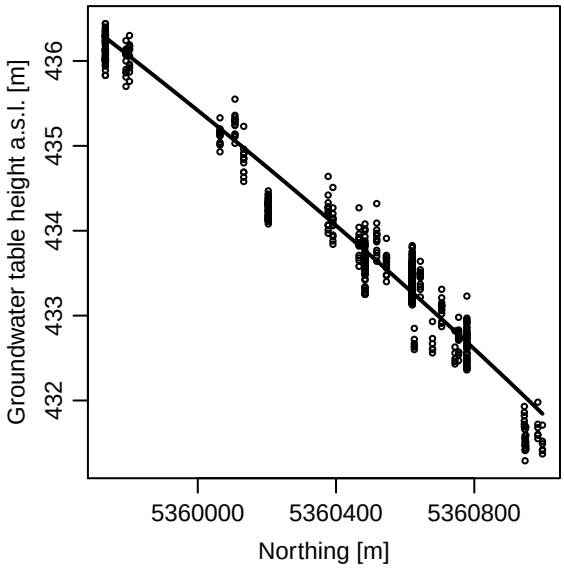

Figure 3.4: All table height measurements (circles) with the fitted regional scale component of the model (solid line). Northing refers to a common Gauß-Krüger projection for south-west Germany (central meridian 12°, Potsdam datum).

The temporal pattern revealed a seasonal sinusoidal fluctuation and an irregular fluctuation of higher frequency.

Fitting the regional scale term in the model equation with two components for the Northing and Easting in the Cartesian coordinate system did not show a significant effect of the Easting component, which was therefore neglected.

94.9 % of the variation in table height could be explained by the regional gradient (figure 3.4, table 3.1). Nevertheless considerable variation was explained by the other two scales. The seasonal fluctuation caused an amplitude of approximately 0.2 m (figure 3.5) and explained another 29.5 % of the residual variation (table 3.1). Incorporating distance to the nearest ditch explained further 0.4 m (figure 3.6) or 58.6 % of the residual variation obtained by the other two model terms. Thus, only 1.5 % of the variation in the data were left unexplained (table 3.1), which included the event scale and errors.

3.3.3 Model performance

Though >98 % of the variation of table height could be explained by the conceptual model (table 3.1), the residuals still revealed temporal and spatial structures. The hydrograph residuals showed parallel temporal patterns for all wells, but also the mean of the residuals differed per well, indicating spatial variation in the residuals (figure 3.7). The temporal semivariogram revealed an exponential plus a periodical structure (figure 3.8), indicating a mean period of

Table 3.1: Quality of the explanation of table height measurements with a physical conceptual model of increasing complexity.

Model complexity	RMSE	95 % quantile of absolute residuals	Residual variance explained[a]	Total variance explained[b]
	[m]	[m]	[%]	[%]
Global mean	1.06	2.40		0.0
+ regional gradient	0.24	0.51	94.9	94.9
+ seasonal fluctuation	0.20	0.43	29.5	96.4
+ distance to nearest ditch	0.13	0.25	58.6	98.5

[a] Fraction of residual variance of less complex model explained
[b] Fraction of variance of measured table height explained

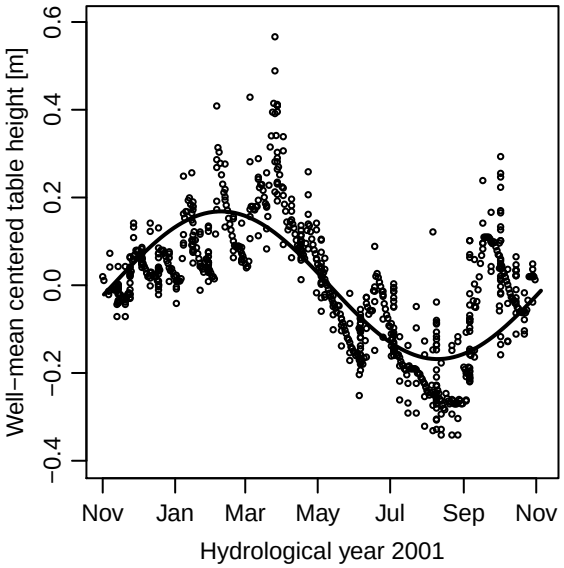

Figure 3.5: Seasonal fluctuation of table height (measurements centred to the mean of the respective wells) and a fitted sine.

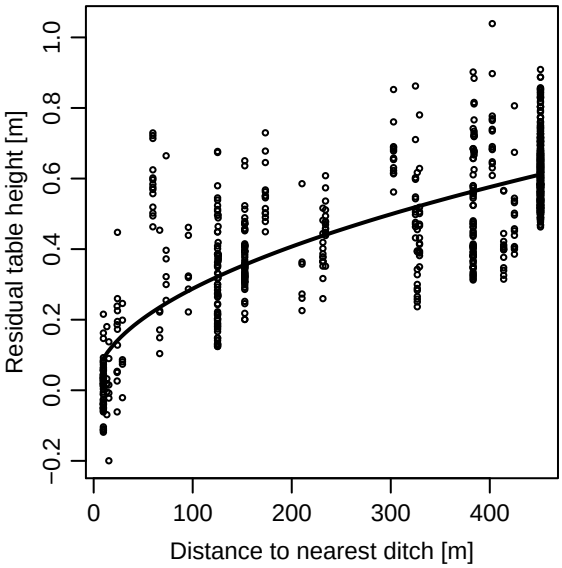

Figure 3.6: Influence of distance to nearest ditch on residual table height obtained by subtracting the fitted regional scale component and the seasonal fluctuation from measured values.

approximately four months in the event scale temporal variation. The spatial semivariogram exhibited a spherical structure with a range of 197 m (figure 3.9). The nuggets were irrelevant in both cases indicating low measurement errors. The sills were 0.02 m^2 for the unexplained spatial variation and 0.009 m^2 for the temporal variation, which correspond to square roots of 0.14 m and 0.10 m. The latter quantifies the standard deviation of the event scale fluctuation around the predicted mean of a certain well caused by rain-drought cycles. The former quantifies the standard deviation of the deviation of the wells from their predicted mean values.

The linear regressions between temporally colocated residuals from each well with residuals from the well with daily values revealed an R^2 (coefficient of determination) of >0.8 for more than half of the wells. The minimum R^2 was 0.25 for a well with weekly time series at the south edge of the study site. This well was located next to a street and might have been influenced by strong local effects of surface runoff. The correlation was significant on a 10 % confidence level for all but two wells ($p<0.01$ for 21 wells, $p<0.1$ for 25 wells). The time series from the wells without significant correlation were monthly time series covering half of the year, thus consisting of only six values and still revealed an R^2 of >0.3. As a consequence, the daily time series was used as secondary variable for prediction by colocated cokriging at all wells. Figure 3.7 illustrates the transfer of the temporal pattern from the daily time series to the interpolated time series at two other wells. cross-validation of the temporal interpolation showed a good agreement between measured and predicted residual table height. The cross-validation yielded a mean RMSE of 0.06 m and <0.1 m even for those wells without significant correlation with the secondary variable and for the well with the smallest R^2.

Cross-validation of the spatial interpolation of model residuals at two dates, based on the temporally interpolated residuals, did not reveal a considerable improvement compared to the prediction with only the conceptual model. The RMSE only decreased from 0.15 m to 0.14 m,

Table 3.2: Quality of the prediction of table height (cross-validation) with the complete conceptual model and with additional geostatistical interpolation (in time and space) of the residuals.

Prediction method	RMSE [m]	95 % quantile of absolute residuals [m]
Conceptual model	0.15	0.28
Conceptual model + spatio-temporal interpolation	0.14	0.25

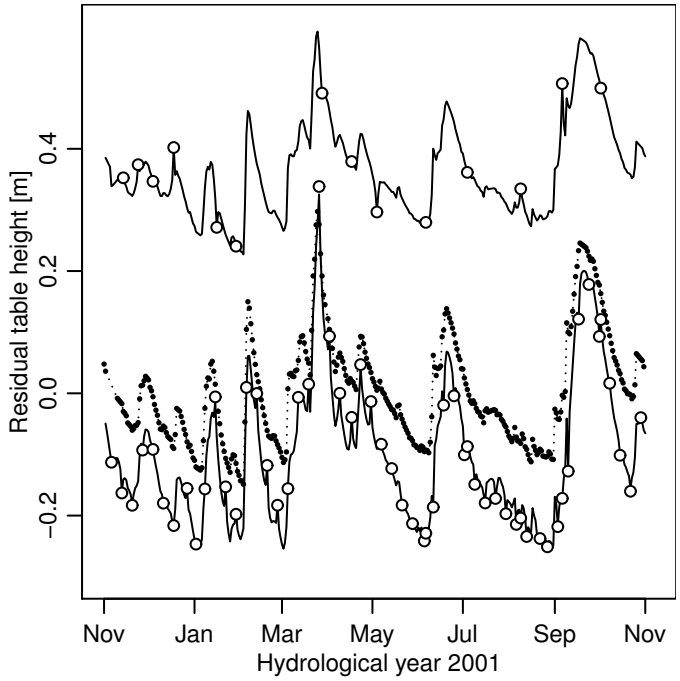

Figure 3.7: Examples of hydrograph residuals obtained by subtraction of the conceptual model and residual interpolation. The dotted line and dots represent residuals from the well with daily values. Examples are shown of residuals from wells with weekly respectively monthly measurements, interpolated to daily resolution (solid lines) based on respective residuals (circles) and colocated cokriging with residuals from the well with daily values as secondary variable.

despite the clear semivariogram (figure 3.9). This was due to the fact that the distance between wells was too large at most places to contribute to the prediction at a left out well. On average only two neighbouring wells were within the range of the spherical semivariogram model and only three wells had the maximum of four other wells within their neighbourhood. The same applied for the joint cross-validation of conceptual model and spatio-temporal interpolation of residuals, which also suffered from the large distance in space between wells despite the good performance of the colocated cokriging in time domain (table 3.2).

3.4 Discussion

The physical conceptual model explained most of the variability in table height data and thus captured the majority of the underlying effects. Four main components were found affecting table height of the studied aquifer: A regional gradient, local gradients towards drainage ditches, seasonal fluctuation and fluctuation with higher temporal frequency (for simplicity called

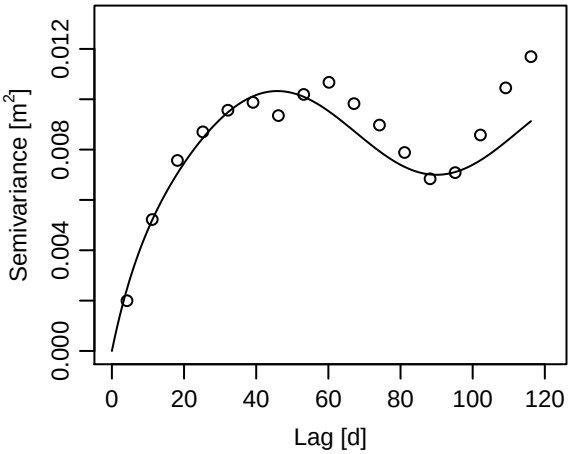

Figure 3.8: Temporal semivariance of table height residuals obtained by subtraction of the conceptual model. Only point pairs obtained from the same well were considered to exclude a spatial effect and were then pooled among all wells.

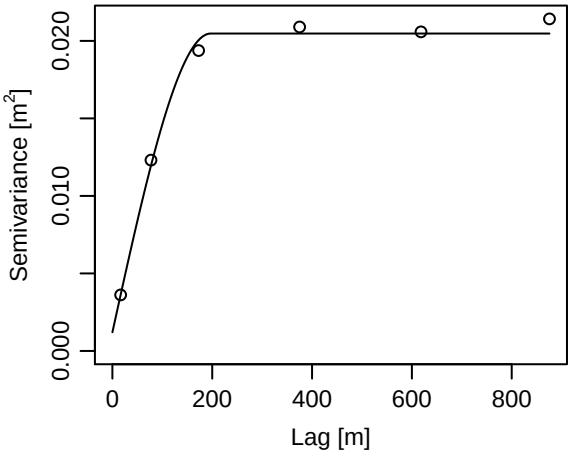

Figure 3.9: Spatial semivariance of residuals of table height obtained by subtraction of the conceptual model. Only point pairs obtained from the same date were considered to exclude a temporal effect and were then pooled among all dates.

‘‘event’’ scale). The first three components were incorporated in the proposed conceptual model and represented 98.5 % of the observed variability in table height with the regional gradient dominating. This dominance corresponded with the topographic situation at the study site, which was also dominated by a south-north slope, as indicated by analysis of the DEM (section 3.3.1). Therefore, flow systems deriving from local topography are not to be expected (Tòth, 1963). Further, highly permeable aquifers, as the studied porous aquifer in the quaternary gravel, are unlikely to be subject of local groundwater mounding following topography (Haitjema and Mitchell-Bruker, 2005).

As was hypothesised, distance to the nearest ditch explained partly the variation in table height and the influence decreased parabolically with distance (figure 3.6). This agrees with other studies considering lateral effects of ditch and subsurface drainage (Hayes Jr. and Vepraskas, 2000; Montagne et al., 2009; Phillips et al., 2010).

The temporal pattern revealed a seasonal sinusoidal fluctuation which corresponded well with historical data from another well located in the Munich gravel plain, showing maximum table height in January and minimum table height in August averaged over the years 1907 to 1950 (Traub, 1956).

The event scale was captured by colocated cokriging with model residuals from a well with daily values. The observed temporal pattern was attributed to weather induced fluctuations of the water table. Besides the event-scale fluctuation, there is residual spatial variation. Though the latter is not of relevant magnitude for prediction (table 3.2), many spatially variable system properties might contribute to this effect (von Asmuth and Knotters, 2004), such as different hydraulic properties of the ditches (Ernst, 1978a,b) or the aquifer.

3.5 Conclusions

The physical conceptual model explained most of the variability in table height data and thus captured the majority of the underlying effects. It is therefore also appropriate as a trend model in groundwater table mapping approaches. The regional gradient contributed most to the variation (4 m) followed by the local gradient to the ditches (0.5 m) and the seasonal fluctuation (0.4 m).

4 Model development

Measuring the conductivity of the ground with electromagnetic induction involves two coils placed on or near the ground (figure 4.1). The first coil (transmitter coil) is supplied with an alternating current, which induces electric currents within the ground through electromagnetic induction. The electromagnetic fields of the first coil and of the currents in the ground are received by the second coil (receiver coil). The signal obtained by the receiver coil is thus related to the electrical conductivity of the ground. Instruments built on this principle and operating at so called ''low induction numbers'' have certain physical constraints built into their design. These constraints justify the assumption that the current flow induced in a homogeneous or horizontally layered ground is horizontal and at any depth independent from the current at any other depth. Consequently, the signal obtained at the ground surface is a linear combination of the conductivities of all depth increments. Further, the relative contribution of the current flow at any depth to the measured signal can be described as a function of relative depth (z), with z being depth divided by the spacing between the transmitter and receiver coil of the instrument. Figure 4.2 shows this depth response function given by

$$\Phi(z) = \frac{4z}{(4z^2+1)^{3/2}} \tag{4.1}$$

for vertical coil configuration (i.e. both coils are oriented vertically with respect to ground surface; figure 4.1), which was the configuration used in the present study. Integrating equation (4.1) according to

$$R(z) = \int_z^\infty \Phi(z)\,\mathrm{d}z = \frac{1}{\sqrt{4z^2+1}} \tag{4.2}$$

gives the cumulative response below any z, thus the contribution of the halfspace below z to the measured signal (McNeill, 1980b; figure 4.3). The cumulative response at ground surface when the instrument is placed on the ground ($z = 0$ defined at ground surface) in the following will be referred to as apparent electrical conductivity of the ground (σ_a).

Following the above considerations, given a finite number of homogeneous horizontal layers, σ_a can be expressed as the sum of the layer conductivities multiplied with the cumulative response between the normalised depths of the layer boundaries:

$$\sigma_\mathrm{a} = \sum_{i=1}^{n} \sigma_i (R(z_{i-1}) - R(z_i)) \quad , \tag{4.3}$$

with z_i and σ_i the normalised depths and conductivities of the n discrete layers (Slavich, 1990).

Equation (4.3) shows that σ_a is related to the conductivities as well as the thickness of the homogeneous layers. However, expressing σ_a as a linear combination of the σ_i with coefficients being a function of layer depths is not suitable, if any layer depth has to be predicted. It is the goal of this work to build an applicable model of which the response is layer depth (i.e. soil thickness). Thus, in the following, an equation is derived that represents the same physical relationships but in a form suitable for such a model.

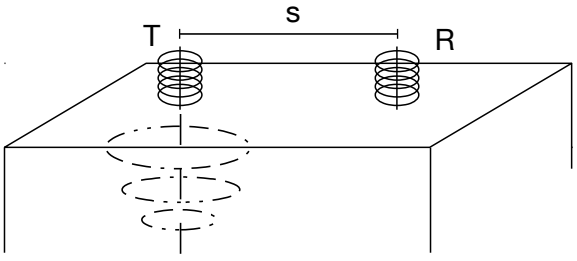

Figure 4.1: Schematic illustration of an instrument for the measurement of apparent electrical conductivity of the ground with electromagnetic induction: A transmitter coil (T) is supplied with alternating current inducing currents in the soil. The electromagnetic fields of the currents in both T and the soil are sensed by the receiver coil (R) at distance s from T. Both coils are vertically oriented with respect to ground surface.

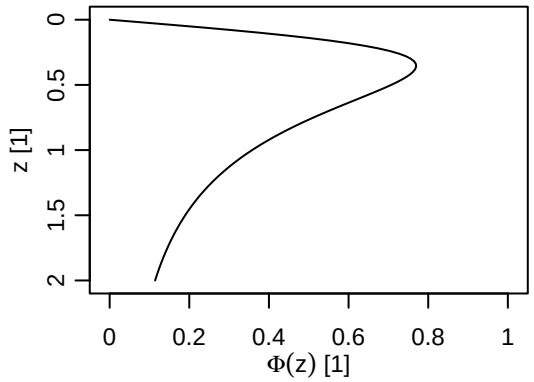

Figure 4.2: Relative contribution of electrical current flow at any depth z(normalised to the intercoil spacing) to the measured σ_{a}-signal (depth response).

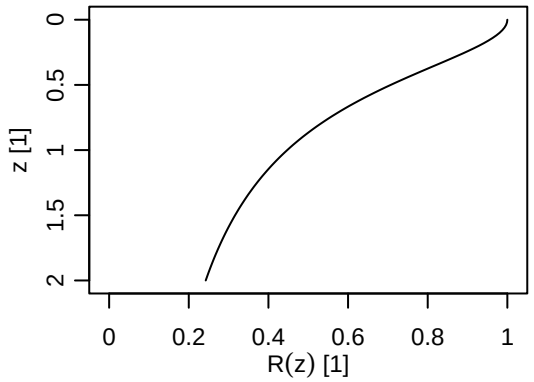

Figure 4.3: Relative contribution of the conductivity of a halfspace below any depth z(normalised to the intercoil spacing) to the measured σ_{a}-signal (cumulative depth response).

The layers are indexed with increasing depth. Defining $z_0 = 0$ and $z_n = \infty$, gives $R(z_0) = 1$ and $R(z_n) = 0$ (compare figure 4.3). Thus, equation (4.3) can be rewritten as

$$\begin{aligned} \sigma_{\mathrm{a}} &= \sigma_1 + \sum_{i=2}^{n} \sigma_i \, R(z_{i-1}) - \sum_{i=1}^{n-1} \sigma_i \, R(z_i) \\ &= \sigma_1 + \sum_{i=1}^{n-1} \sigma_{i+1} \, R(z_i) - \sum_{i=1}^{n-1} \sigma_i \, R(z_i) \\ &= \sigma_1 + \sum_{i=1}^{n-1} R(z_i)(\sigma_{i+1} - \sigma_i) \quad , \end{aligned} \tag{4.4}$$

expressing σ_{a} as linearly related to the output of $R(z)$, which is referred to as ‘‘transformed layer depth’’ in the following. Equation (4.4) can be solved for $R(z_j)$ with $1 < j < n-1$, which gives

$$R(z_j) = \frac{\sigma_{\mathrm{a}} - \sigma_1 - \sum_{i=1}^{j-1} R(z_i)(\sigma_{i+1} - \sigma_i) - \sum_{i=j+1}^{n-1} R(z_i)(\sigma_{i+1} - \sigma_i)}{\sigma_{j+1} - \sigma_j} \quad . \tag{4.5}$$

For $j = 1$ respectively $j = n-1$ obviously just the next to last respectively last sum has to be omitted above the fraction line. Equation (4.5) reveals that any transformed layer depth can be shown to be linearly related to σ_{a} and the transformed depths of the remaining layers. Supposed the σ_i are constant over a whole domain under study and given a set of measured values of σ_{a} and corresponding layer thicknesses z_i, a linear regression model can be set up with the form

$$R(z_j) = \beta_0 + \beta_j \, \sigma_{\mathrm{a}} + \sum_{i=1}^{j-1} \beta_i \, R(z_i) + \sum_{i=j+1}^{n-1} \beta_i \, R(z_i) + \epsilon \quad . \tag{4.6}$$

The coefficients β_i depend only on the layer conductivities σ_i and ϵ is a zero mean heteroscedastic and possibly spatially autocorrelated error component.

The heteroscedasticity of ϵ can be expressed by a variance function (Pinheiro and Bates, 2000), which can be derived with the Delta method (Tiwari and Elston, 1999) as follows. Let ϵ_z be the normally distributed, homoscedastic error of z_j. In case ϵ_z is sufficiently small, from an approximation of the graph of R by its gradient (first degree Taylor series approximation) about z_j follows

$$\mathrm{Var}(\epsilon) \approx \mathrm{Var}(\epsilon_z) \, \Phi(z_j)^2 \quad , \tag{4.7}$$

with Φ the depth response function expressed in equation (4.1) (Tiwari and Elston, 1999).

Spatial autocorrelation in ϵ can stem from either spatial autocorrelation of the measurement error attributed to z_j, or a violation of the assumption of layer homogeneity (i.e. constant σ_i) within the domain under study. In the latter case, equation (4.3) might still be valid for every

single measurement location, but the regression coefficients β_i do no longer reflect the true σ_i at every measurement location. Spatially autocorrelated variation of the σ_i then becomes part of residual variation.

The assumption of layer homogeneity will be seldom met over a whole study area because of varying soil properties. This calls for an approach, which allows the σ_i to vary spatially (Sudduth et al., 2010). Restricting the assumption of homogeneity to arbitrarily small neighbourhoods around a prediction location tends to allow continuous variation of the σ_i in space. Though in practice the neighbourhood cannot be arbitrarily small, fitting of the physically based model within sufficiently small neighbourhoods is sensible, even if no relationship between response and covariates of the model is statistically evident for the whole study area (Goovaerts, 1997). However, the tradeoff between minimising the extent of the neighbourhood and choosing enough data points to allow a reliable model fit might lead to considerable variation of the σ_i within the neighbourhood. Consequently, ϵ can be spatially autocorrelated and this has to be taken into account, even when fitting the trend model to restricted neighbourhoods.

The predictions $\widehat{R(z_j)}$ from a model fitted to equation (4.6) are transformed layer depths. Using a first degree Taylor series approximation, the expected value of normalised layer depth is given by

$$E[\widehat{z_j}] \approx R^{-1}(\widehat{R(z_j)}) \tag{4.8}$$

(Tiwari and Elston, 1999), if ϵ_z is sufficiently small. Then, from the predictions $\widehat{R(z_j)}$, the normalised layer depths $\widehat{z_j}$ can be obtained using the inverse of equation (4.2),

$$z = R^{-1}(R(z)) = \sqrt{\frac{1}{4\,R(z)^2} - \frac{1}{4}} \quad , \tag{4.9}$$

and multiplication with the intercoil spacing yields the actual layer depths. However, for small absolute values of $R(z)$, small changes in $R(z)$ result in large changes of z when applying R^{-1} (compare figure 4.3). In such a case, small errors in $\widehat{R(z_j)}$ might cause unstable estimates $\widehat{z_j}$.

It has been shown above that a theoretically founded linear relationship exists between the transformed depth of a layer and σ_a and the transformed depths of the remaining layers. The response of the resulting model, equation (4.6), can be back transformed to obtain actual layer depth (equation (4.9)). This approach has some advantages over using the depths response functions to construct a nonlinear regression model with actual layer depth as response. Firstly, a linear model has simpler requirements regarding the fitting (Pinheiro and Bates, 2000). Secondly, when moving towards a spatially explicit approach with common geostatistical techniques, linear relationships between covariates are often required (Goovaerts, 1997).

5 Material and methods

5.1 Study site

The present study has been undertaken on Grünschwaige research station, a 135 ha site, managed as 21 pastures and meadows on permanent grassland (for site and management conditions see Schnyder et al., 2006). The site is located at the north edge of the Munich gravel plane (11°50′20″ East, 48°22′50″ North), an outwash plane consisting of quaternary glacial deposits. Due to the northward decline of the plane, the groundwater level exceeds the gravel at the north edge, which led to the formation of fens (Traub, 1956), though nowadays these are more or less degenerated by drainage and carbon loss. Residuals of such fens occur on the western part of the study site. Thus, the site is partly covered by peat (histosols) in the western part of the site, whereas the eastern part consists of mineral alluvial soils (inceptisols; Haunschild, 1981; Schnyder et al., 2006). The two southernmost fields have been excluded from the analysis due to missing groundwater data (see section 3.2.1), leaving an area of the study site of 116 ha (figure 5.1).

5.2 Preparation of high resolution data

A high resolution (2 m×2 m grid) digital elevation model (DEM) derived from airborne laser-scanning of the Bavarian land surveying office (Landesamt für Vermessung und Geoinformation, n.d.; figure 5.2) was used to derive terrain parameters. The DEM was noisy and exhibited artefacts that appeared as straight rills in approximate north-south direction, possibly originating from the laser-scanning. Therefore, the original DEM was filtered in two steps. Firstly, local outliers were detected by estimating the probability to find a certain value in a neighbourhood by comparing the observed value with a kriging estimate (Hengl et al., 2004). A 7×7 pixel neighbourhood was chosen to capture, besides real outliers, human artefacts near the field borders like ditches and dams. A Gaussian semivariogram model with a small nugget effect (Posa, 1989) and a fitted practical range (Journel and Huijbregts, 1978) of 12 m was used to represent the spatial dependence structure in the DEM. The choice of a Gaussian structure was suggested by the data and the fact that the represented landscape mainly consists of smooth, continuous features (Goovaerts, 1997). Observed values of elevation in the DEM less probable than 5 % were replaced by the kriged estimates. In a second step, the DEM was smoothed to filter out artefacts and random or micro-scale variation by fitting bivariate quadratic polynomials over the coordinates to 15×15 grid cell windows and replacing elevation by the fitted

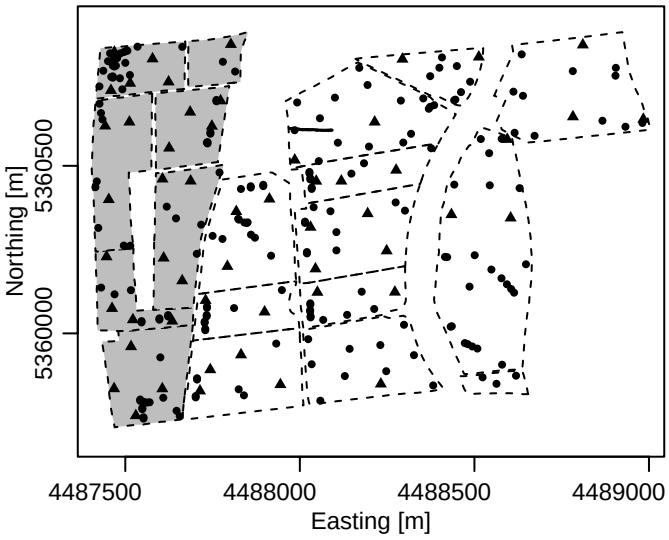

Figure 5.1: Map of the study site, showing the arrangement of pastures and meadows (dashed polygons) and the locations of 297 soil sampling sites. Soil samples were taken with a machine auger (triangles), with hand augers (dots) and from a transect of soil profiles (small dots aligned in the centre of the upper half of the plot). Grey shaded areas represent peat soil sites. Coordinates refer to a common Gauß-Krüger projection for south-west Germany (central meridian 12°, Potsdam datum).

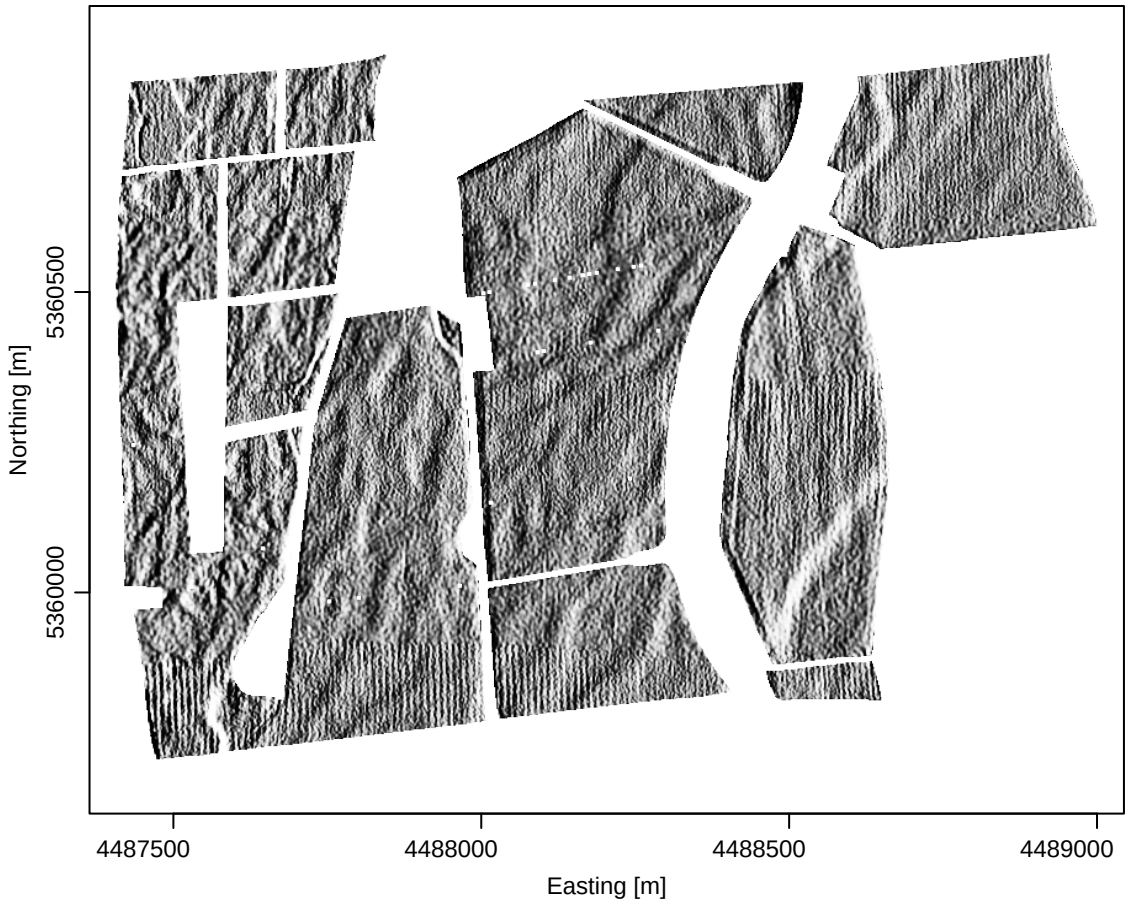

Figure 5.2: 2 m×2 m gridded digital elevation model (DEM) derived from airborne laser-scanning as distributed by the Bavarian land surveying office (Landesamt für Vermessung und Geoinformation, n.d.). The representation is a histogram equalised shaded relief with 15 fold exaggeration as created with GRASS (GRASS Development Team, 2011).

values (GRASS Development Team, 2011; Hofierka et al., 2009). The side length of the window comprises two times the practical range of the semivariogram of elevation, which was used for outlier removal. Thus, micro scale variability and noise was filtered, if it occurred at scales below what is represented by the semivariogram. The root mean squared difference between original and corrected DEM was 0.05 m. The 95 % quantile of differences was 0.09 m. Both are within the vertical accuracy of ±0.2 m given by the manufacturer of the DEM (Landesamt für Vermessung und Geoinformation, n.d.). This indicates that the corrected DEM is not over-smoothed. The 95 % quantile of relative relief (difference between minimum and maximum height; MacMillan and Shary, 2009) within a moving window of 3×3 grid cells was reduced from 0.6 m to 0.3 m. Accordingly, the corrected DEM is visually less noisy (compare figure 5.2 and figure 5.3), and represents topographic features at a vertical scale of several decametres more clearly. The vertical magnitude of such features was 0.25 m, quantified as the median of the relative relief within a moving window of 15×15 grid cells of the corrected DEM. This enlightens the need for noise reduction given the 95 % quantile of relative relief of 0.6 m in the uncorrected DEM. However, the previously described artefacts persist in the corrected DEM, though reduced in magnitude (figure 5.3).

Groundwater table depth (z_{w}) was obtained from the smoothed DEM and point estimates of table height at the respective grid cell centres. It was refrained from true block estimates as the variability of modelled table height within a 2 m×2 m grid cell was negligible. Table height of the shallow unconfined aquifer at the study site was modelled with a physical conceptual model and geostatistical interpolation of residuals as described in detail in chapter 3. For every field, z_{w} was estimated for the specific day at which σ_{a} had been measured. On average, the spatial and

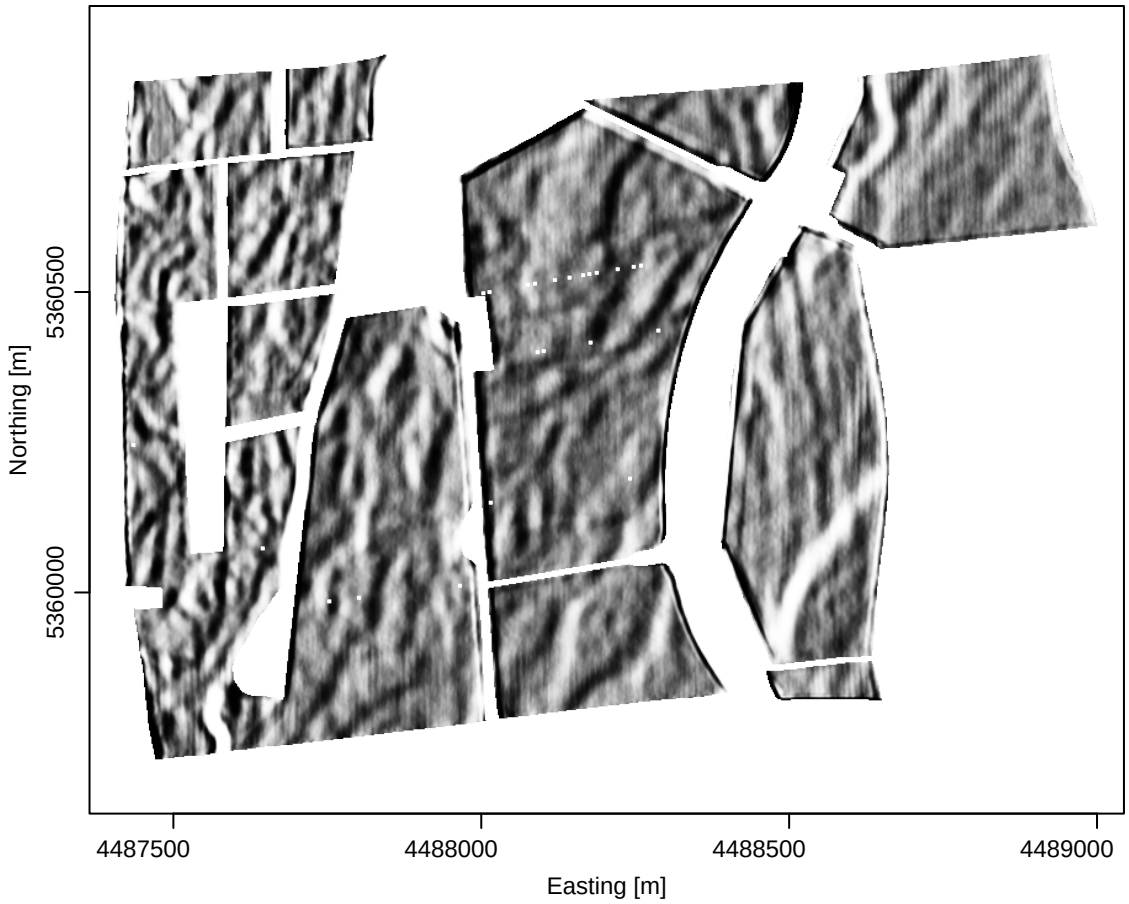

Figure 5.3: 2 m×2 m corrected and smoothed digital elevation model (DEM). The representation is a histogram equalised shaded relief with 15 fold exaggeration as created with GRASS (GRASS Development Team, 2011).

temporal geostatistical interpolation of residuals did not substantially improve the prediction of groundwater table height (section 3.3.3; table 3.2). Nevertheless, it was applied here, because estimates are needed for single days that are potentially strongly influenced by weather events.

From the smoothed DEM, a hydrologically based land-surface parameter, which has been found to be related to soil water content and is referred to as wetness index, was derived according to

$$w = \ln\left(\frac{A_s}{\tan\gamma}\right) \quad , \tag{5.1}$$

with A_s the upslope area contributing to the flow crossing a grid cell and γ the steepest slope angle of the respective cell (Moore et al., 1991). A_s was calculated with GRASS (GRASS Development Team, 2011) as described by Mitášová et al. (1995). Additionally, for every grid cell with no upslope grid cells, A_s was set half of the area of a grid cell (2 m^2). γ was computed based on bivariate quadratic polynomials fitted to 15×15 grid cell windows of the smoothed DEM (GRASS Development Team, 2011; Hofierka et al., 2009).

Measurements of apparent electrical conductivity of the ground (σ_a) were conducted in spring (February to April) were soil moisture content could be assumed to be at field capacity. This was assumed to provide the advantage of a larger contrast in conductivity between topsoil and gravel (Brus et al., 1992) and of better delineation of lateral patterns (Brevik et al., 2006). Two possible influences of urine and dung patches are also likely to be reduced in spring. Small-scale patches of higher sward productivity (Shiyomi et al., 1998) can take up soil water quicker and thus cause small-scale variability in soil water content during the growing season. The influence of spots with highly conductive soil solution due to animal excreta might be reduced by leaching over winter too, though such effects can be perennial (Afzal and Adams, 1992) and might have

led to local outliers. The measurements were conducted with an EM38 ground conductivity meter (Geonics Ltd., Mississauga, Canada). The EM38 was mounted in vertical orientation on a plastic sledge, towed by an agricultural tractor equipped with a Global Positioning System (GPS) receiver. The positions of the EM38 were derived from the measured positions of the GPS antenna with a kinematic model described in detail in chapter 2. Further, the σ_a-data were corrected for differences in soil temperature, instrument drift and outliers (see section 2.3.1). From the irregularly placed measurements of σ_a, a gridded map corresponding to the previously described DEM was produced by ordinary kriging (Goovaerts, 1997) using the semivariogram of σ_a obtained by the structural analysis described in section 5.4.

5.3 Soil sampling

Measurements of soil thickness (z_s) where obtained at a total of 297 sites throughout the study site (figure 5.1), partly by machine augering, partly with hand augers and from a transect of soil profiles. z_s, in the present study, is defined as the distance between ground surface and the top of the gravely substrate within which no considerable signs of soil formation or mixing with soil are visible.

For the machine augering, sampling sites were preselected aided by the previously obtained map of σ_a with the goal to obtain a representative set of z_s-σ_a pairs. Therefore, the cell centres of the grid of kriged σ_a served as candidate sites. From the complete grid, those cells were excluded, which were closer than 10 m to field boundaries or closer than 5 m to outliers or artefacts in σ_a (see section 2.3.1). The remaining set of candidate sites was stratified into 10 classes of σ_a values of equal width. From these classes, a maximum of 500 sites with σ_a values closest to the centre of the class was chosen. From the sites selected in the described way, hence representing the whole range of σ_a, a final set of sampling sites was selected in an automated manner by maximising the distance between sampling sites under the constraint of

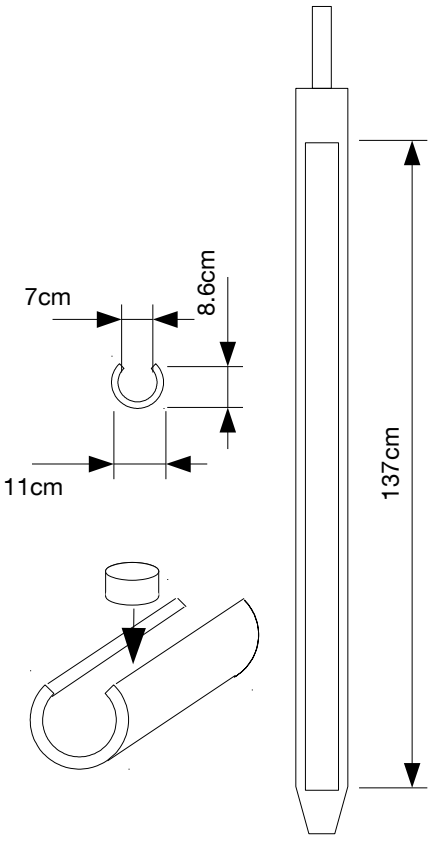

Figure 5.4: Drawing of the ramming core probe used for machine augering. The round bar at the top of the probe served as fixing point for the hydraulic hammer and for pull-out. The cross section with the depicted measures and the subjacent view show that standard 100 cm^3 core cutters can be taken out of the probe at its open side. In the present study, the opening was used for visual inspection of the soil profile and measurement of soil thickness (z_s).

equal representation of each σ_a-stratum in the final set. This resulted in a set of 36 sampling sites, which was representative for the spatial as well as for the σ_a domain. In favour of better representation of single fields, 26 sites were added manually on those fields, where the automated selection placed no or only few sampling sites. The so obtained 62 sites for machine augering (figure 5.1) were approximately determined in the field with a differential GPS receiver. The true sampling sites were then determined by averaging the positions measured during at least 10 min at a frequency of 1 s^{-1} with stationary GPS antenna.

Soil sampling was executed with a ramming core probe (figure 5.4). The probe was driven into the ground down to the gravelly substrate and pulled out with a hydraulically driven machine mounted to an agricultural tractor. Measurement of z_s and visual inspection was applied at the profiles from the open side of the probe. At most of the sampling sites, two cores were taken within a distance of few decimetres from the GPS-measured position and an average value of z_s was recorded. Similarly to the profiles excavated with the ramming core probe, z_s was measured at soil profiles excavated by digging along a transect (figure 5.1).

The samples obtained with machine augering were complemented with samples obtained with a hand auger (Edelmannbohrer), that did not allow the visual inspection of the undisturbed profile but measurement of z_s by digging down to the gravelly substrate. In swampy areas of the study site, another type of hand auger (Pürckhauer) was used because the first mentioned did not allow sampling below 1 m and turned out to be inadequate for sampling wet peat. The sites for manual sampling (figure 5.1) were chosen in the field to be evenly spread over the study site and at special points of interest (e.g. along topographic gradients) as well as at sites where the excavated soil cores could not be used for the measurement of z_s. Positions were determined with Real Time Kinematic GPS, which allowed a positioning with sub meter accuracy within few seconds.

5.4 Modelling and evaluation

z_s and z_w at the study site range both within 0 m and 1.5 m. The depth up to which the underlying halfspace is known to contribute significantly to σ_a (chapter 4) measured with the EM38 is approximately 1.5 m (Geonics Limited, n.d.; Triantafilis and Monteiro Santos, 2009). Therefore, σ_a is deemed to be (amongst others) controlled by z_s and z_w at the study site. This gives the possibility to predict z_s according to the considerations in chapter 4. To this end, the ground is assumed being vertically divided into three homogeneous layers with limits corresponding to z_s and z_w. z, as defined in chapter 4, is a dimensionless measure (depth normalised with the intercoil spacing of the σ_a-measurement instrument). The intercoil spacing in case of the EM38 is 1 m. Therefore, the terms z_s and z_w are used interchangeably for soil thickness respectively groundwater table depth and their respective normalised values, due to numerical equivalence. According to the general model formulation in equation (4.6), transformed z_s can be predicted by fitting a model of the form

$$R(z_s) = \beta_0 + \beta_1 \sigma_a + \beta_2 R(z_w) + \epsilon \quad . \tag{5.2}$$

Under the assumption of layer homogeneity in a local neighbourhood, surrounding sampling sites were selected for every sampling site within a radius of 100 m. Where less than 20 points were found within this radius, the search radius was enlarged up to either a distance within which 20 points were found or a maximum of 360 m. The lower threshold distance (100 m) was necessary to ensure significant variability in the covariates even where 20 points were found within a smaller search radius. The upper threshold distance (360 m) was the minimal distance assuring that at least 10 points were in every neighbourhood, which is considered the least acceptable number to get reasonable estimates from the neighbourhood (Goovaerts, 1997).

The trend model according to equation (5.2) was fitted to the selected neighbourhoods using generalised least squares (GLS) as implemented in the package nlme (Pinheiro et al., 2012) within the software environment R (R Development Core Team, 2012). A variance function according to equation (4.7) representing heteroscedasticity was provided to the fitting algorithm as well as a residual spatial autocorrelation structure (Pinheiro and Bates, 2000).

The inference of the residual autocorrelation structure is not straightforward as it has to be performed on the residuals, which are not known a priori (Goovaerts, 1997). However, the residual autocorrelation structure is contained within the autocorrelation structure of the response variable of the linear model (Kitanidis, 1993). A structural analysis of the semivariogram of the response variable can reveal nested autocorrelation structures that can be attributed to different sources of spatial variability (Journel and Huijbregts, 1978). Such sources of spatial variation of the model response are the residual spatial variation and the spatially varying covariates. To assess the autocorrelation structures present in the response and the covariates in equation (5.2), experimental semivariograms were calculated for the extensive datasets of $R(z_\mathrm{w})$, w and σ_a with lag classes ranging from 2 m width for the smallest lags up to 5 m width for lags corresponding to the maximum search radius in neighbourhood selection (360 m). Experimental semivariograms for the more sparse ground truth derived $R(z_\mathrm{s})$ and corresponding residuals were calculated with lag classes ranging from 4 m width for the smallest lags up to 50 m width for lags up to 360 m. A set of basic semivariogram functions was chosen that allowed to build nested semivariogram models fitting the experimental semivariograms. The sills and ranges of the semivariogram models were fitted to the experimental semivariograms of the high resolution data using ordinary least squares (Pebesma, 2004). The semivariogram model of the more sparse soil data was obtained by fitting the same structures (with fixed ranges) to the respective experimental semivariogram. Incorporating a covariate in the trend model removes its spatial structure from the semivariogram of the residuals (Kitanidis, 1993). Additionally, semivariances of the response variable at small lags tend to be relatively unaffected by the trend (Goovaerts, 1997). Thus, the structure with the shortest range and corresponding to w, which was not incorporated in the trend model, was chosen to model the residual spatial variation when fitting the trend using GLS. As predictions are the more insensitive to the specification of the residual autocorrelation structure the more of the variability is explained by the trend, this choice might be uncritical with respect to the prediction of z_s (Kitanidis, 1993). Practical ranges of the Gaussian and exponential semivariogram functions were calculated according to Journel and Huijbregts (1978) as the range were 95 % of the sill is reached with $a' = a\sqrt{3}$ respectively $a' = 3a$ (with practical range a' and range a).

In order to be able to fit the linear model to colocated data at the soil sampling sites, values of z_w at the soil sampling sites were obtained by selecting the respective values from colocated cells of the 2 m$\times$2 m grid given by the DEM. σ_a was obtained at soil sampling sites by ordinary kriging (Goovaerts, 1997) of measured σ_a within a neighbourhood with 10 m radius and using the semivariogram model of σ_a obtained in the structural analysis. The appropriateness of the neighbourhood radius was assessed by plotting kriging weights vs. distance to the prediction location for a few randomly selected sampling sites (not shown).

Rarely, the fitted values of the model response slightly exceeded a value of 1, which is beyond the domain of R^{-1} (equation (4.9)). Thus, prior to back transformation of the fitted model response to estimates of z_s, those values where set to 0.99. Setting to 1 would have denoted assuming zero soil thickness, which seems fairly unrealistic at the study site, whereas $R^{-1}(0.99) = 0.07$, thus corresponding to 7 cm soil thickness.

To assess the goodness of fit at the scale of z_s, a root mean squared error (RMSE) was calculated from the measured values and the back transformed fitted model response in each neighbourhood. To assess the capability to predict z_s at unmeasured locations, the fitting was repeated under exclusion of the prediction location around which the neighbourhood was build.

A value of residual z_{s} was calculated for each prediction location from the fitted model obtained that way and the respective measured value (cross-validation). From these residuals, overall RMSE and mean error were calculated for the whole study site.

The physical meaning of the coefficients in equation (5.2), β_i, is different depending on whether $z_{\mathrm{s}} < z_{\mathrm{w}}$ or $z_{\mathrm{s}} > z_{\mathrm{w}}$. In the former case, the model is equivalent to equation (4.6) with $j = 1$. The σ_i that form the coefficients are those of topsoil (above z_{s}), unsaturated subsoil (between z_{s} and z_{w}) and aquifer (below z_{w}). In the latter case, the model is equivalent to equation (4.6) with $j = 2$ and the medium layer is saturated soil. Mixing up both layer configurations in one model fit might give unreliable predictions. Therefore, the procedure of neighbourhood selection and model fitting was repeated under exclusion of the sampling sites where $z_{\mathrm{s}} > z_{\mathrm{w}}$ for prediction locations where $z_{\mathrm{s}} < z_{\mathrm{w}}$ and vice versa. For six sampling sites, this did not allow selecting at least 10 sampling points within a search radius of 360 m. Those RMSEs of both fitting procedures, which differed due to omitted sampling sites in the neighbourhood, were compared with a one-sided Wilcoxon matched pairs signed rank test, to test whether omitting the respective sampling sites significantly improved the prediction.

In order to map z_{s} at the resolution of the DEM, z_{s} was predicted at each grid cell using the values of the covariates at the grid cell and the fitted trend model of the nearest soil sampling site. For mapping, only those models were used, which had been fitted with consistent layer configuration. Thus, the prediction was made based on one model fit for each of the Thiessen polygons (Goovaerts, 2000) that were made up by the sampling sites for which the fitting of a model with consistent layer configuration was possible.

6 Results

6.1 Soil sampling

The undisturbed soil samples obtained by machine augering revealed different types of profiles that can roughly be divided into five classes. These are described here by means of the horizons occurring above the gravelly substrate (exemplary coloured photographs and corresponding site data shown in appendix A):

(i) Deep (soil thickness >0.5 m) peat soils, which are degraded near the surface due to aeration and intact in depth, especially below the groundwater table (figure A.1a).

(ii) Shallow peat soils, which are degraded throughout the whole profiles (figure A.1b).

(iii) Shallow soils consisting of a single layer of humic mineral soil (figure A.1c).

(iv) Profiles with alternating horizons of mineral soil, ochre and peat (figure A.1d).

(v) Humic mineral soils with an intermediate layer of loamy or sandy material between topsoil and gravelly substrate (figure A.1e).

Soil thickness (z_s), is defined as the distance between ground surface and the top of the gravelly substrate in the present study. Thus, an important characteristic for the measurement of z_s is the nature of the limit between soil and gravel. Often, a sharp discordance existed between the peaty or loamy soil and the gravelly substrate (figure A.2a), but also more or less important (up to few decimetres) vertical zones with gradual change of the proportion of gravel without a clear limit occurred (figure A.2b).

The small and micro scale spatial variability of z_s also has to be taken into account when analysing the relationship with other variables of which the areal support exceeds the scale of such variation (Atkinson and Tate, 2000). Considerable differences appeared between two soil cores taken at one sampling site (thus within a distance of approximately 0.5 m, figure A.2b), and even within the extend of the probe the variation in z_s was sometimes of the order of magnitude of a decimetre (figure A.2c). In both cases recorded values of z_s are an average of the observed values. In case of $R(z_\mathrm{w})$, the support corresponds to the resolution of the used digital elevation model (DEM). The areal extent of the soil assessed with a single σ_a measurement with the ground conductivity meter EM38 is of several square metres (Sudduth et al., 2001). Therefore, the described small and micro scale spatial variability of z_s cannot be explained by the covariates in equation (5.2) and thus will be incorporated in the error component ϵ. True measurement error

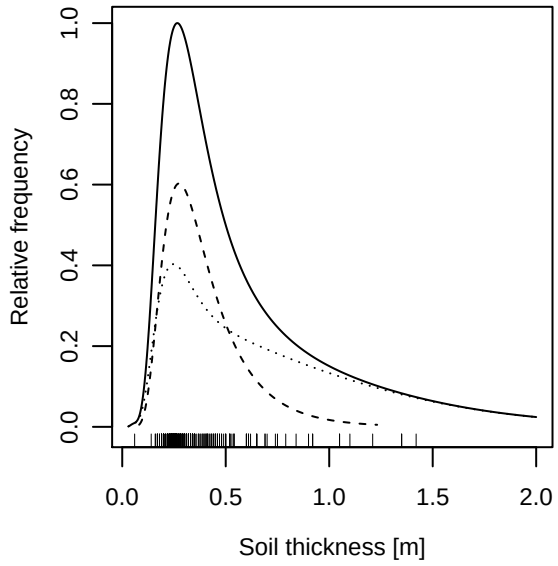

Figure 6.1: Estimated probability density of soil thickness (kernel density of logarithms, back transformed). The solid line represents all samples (n=297), the dotted line those from the peat soil site (n=94) and the dashed line those from the mineral soil site (n=203). Vertical lines at the bottom of the graph represent the actual measured values.

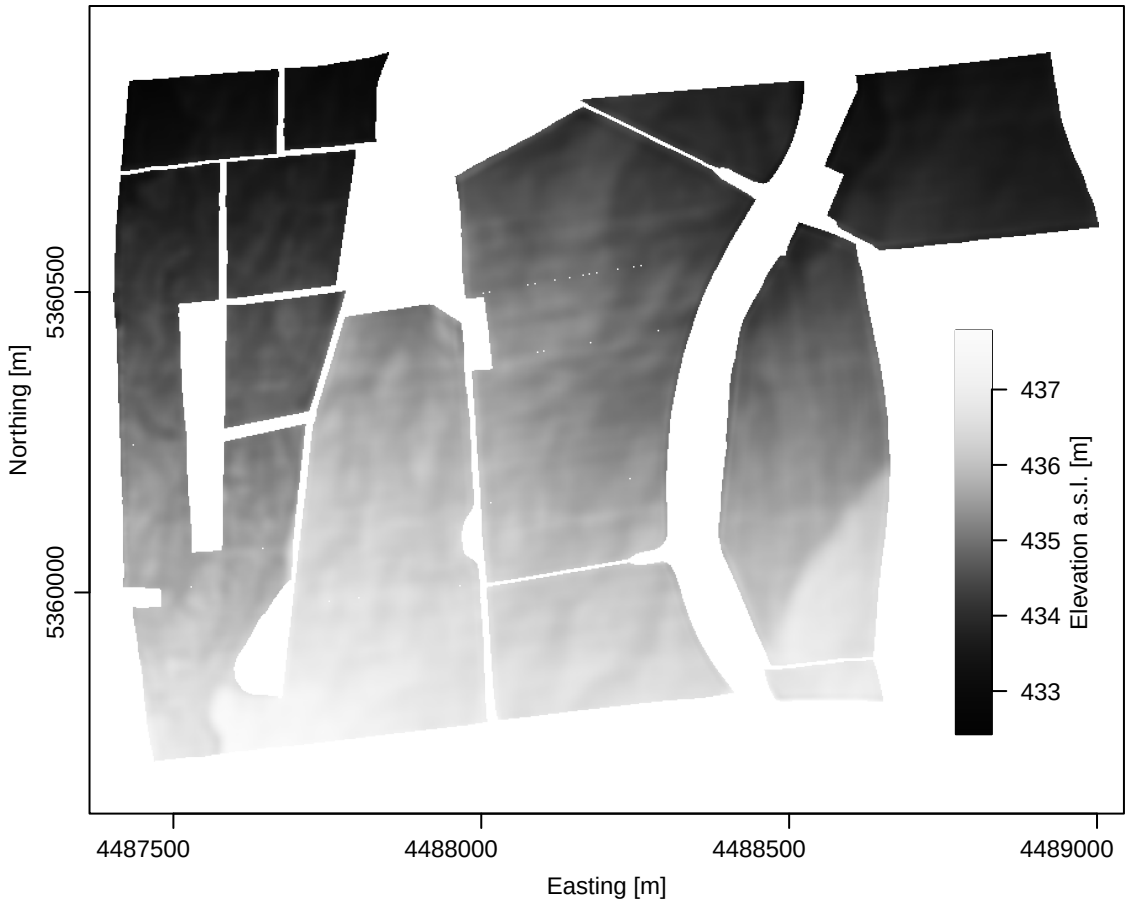

Figure 6.2: Digital elevation model (DEM) in terms of a 2 m×2 m grid of elevation above sea level (a.s.l.). The DEM was obtained by outlier removal and smoothing of the original data source from the Bavarian land surveying office (Landesamt für Vermessung und Geoinformation, n.d.).

can be neglected considering the magnitude of the small and micro scale variability of z_s, which is therefore equivalent to ϵ_z in equation (4.7). From a visual appraisal of figure 4.3, it follows that the depicted graph can reasonably be approximated by its gradient on an interval with the extent of ϵ_z. Equation (4.7) and equation (4.8) can thus be considered valid and the back transformation expressed in equation (4.9) be applied.

z_s obtained with machine and hand augers and along a transect of excavated profiles was mostly shallow (<0.6 m). The mineral soil sites exhibited less variability than the peat soil sites. Soils with measured z_s deeper than 0.8 m occurred only on the peat soil sites, where the range of soil thickness was very wide. However, the majority of the sampled peat soils were shallow too (figure 6.1). Only few samples showed local occurrences of deep intact peat as shown on figure A.1a, whereas the shallow peat soils correspond to those degraded throughout the whole profile (figure A.1b).

6.2 High resolution mapping of auxiliary variables

The topography of the study site can be described at three scales. At the largest scale, there is an overall decline of approximately 3 ‰ from south to north. The medium scale topography exhibits three ‘‘terraces’’. The lowest corresponds with the peat soils in the western part of the study site (figure 5.1), the medium terrace with most of the mineral soil and the highest consists of a raised area at the south-eastern corner of the study site (figure 6.2). The small scale topography exhibits flat undulating patterns as displayed in figure 5.3 with horizontal extend of around 25 m (two times the semivariogram range of elevation) and vertical extend of 0.25 m (relative relief within horizontal extent; section 5.2).

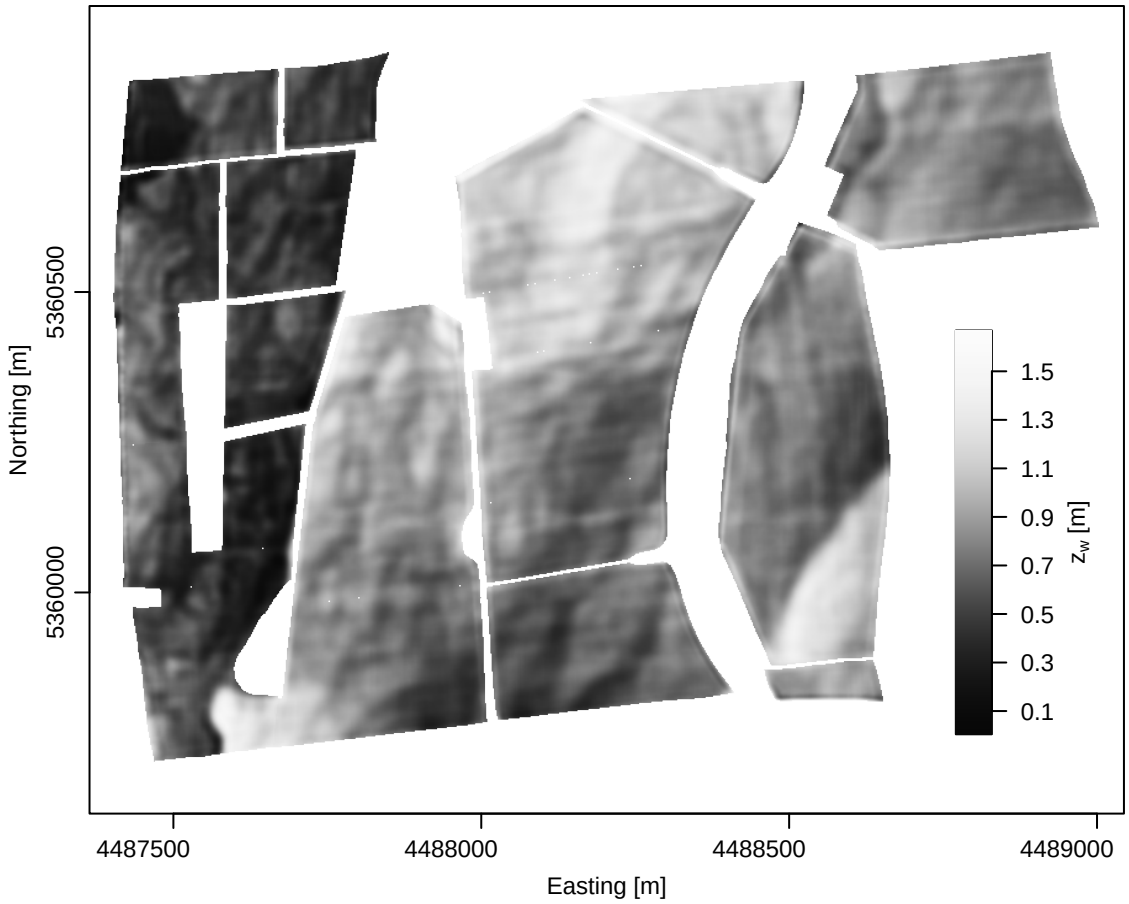

Figure 6.3: 2 m×2 m grid of groundwater table depth (z_w) obtained as the difference between a digital elevation model (DEM; figure 6.2) and modelled groundwater table height (chapter 3).

The groundwater table has a northward decline of approximately 4 ‰ (figure 3.4), thus similar to the decline of the land surface. Accordingly, due to the fact that groundwater table depth (z_w) is the difference between ground surface elevation and groundwater table height, the large scale decline is not reflected in the map of z_w. But, as the groundwater table has been modelled as a smooth surface (chapter 3), z_w exhibits patterns that derive from the terraced medium scale and small scale undulating topography of the study site (figure 6.3).

The wetness index (w), as a topography derived parameter (compare equation (5.1)), naturally inherits patterns from topography. Due to the overall flat terrain of the study site, overlain by the small scale undulating patterns, flow accumulates in the small valleys, which often drain into the soil because they have a dead end. This leads to upslope contributing areas (A_s) that do not reach across the small scale undulations. Consequently, w inherits only the small scale patterns from topography at the study site (figure 6.4). Obviously, the mentioned inheritance is not a mere rescaling of elevation data because of the accumulating process described by w. Therefore the small scale topographic patterns are retained in the map of w, but the small valleys appear sharpened. Additionally, in the map of w these patterns appear to be clipped to the gridded geometry of the DEM, as they exhibit preferably the orthogonal and diagonal directions of the northwards oriented square grid. This is a common artefact of digital terrain analysis (Florinsky, 2005). It should be mentioned here too that artefacts of the original DEM, partly persisting in the corrected DEM from which w was derived, also do not leave w unaffected. Some straight south-north oriented valleys appearing at the north-eastern corner and less obviously along the south edge of the study site (figure 6.4) clearly derive from such structures in the DEM (figure 5.2 and figure 5.3) that are deemed to be artefacts (section 5.2).

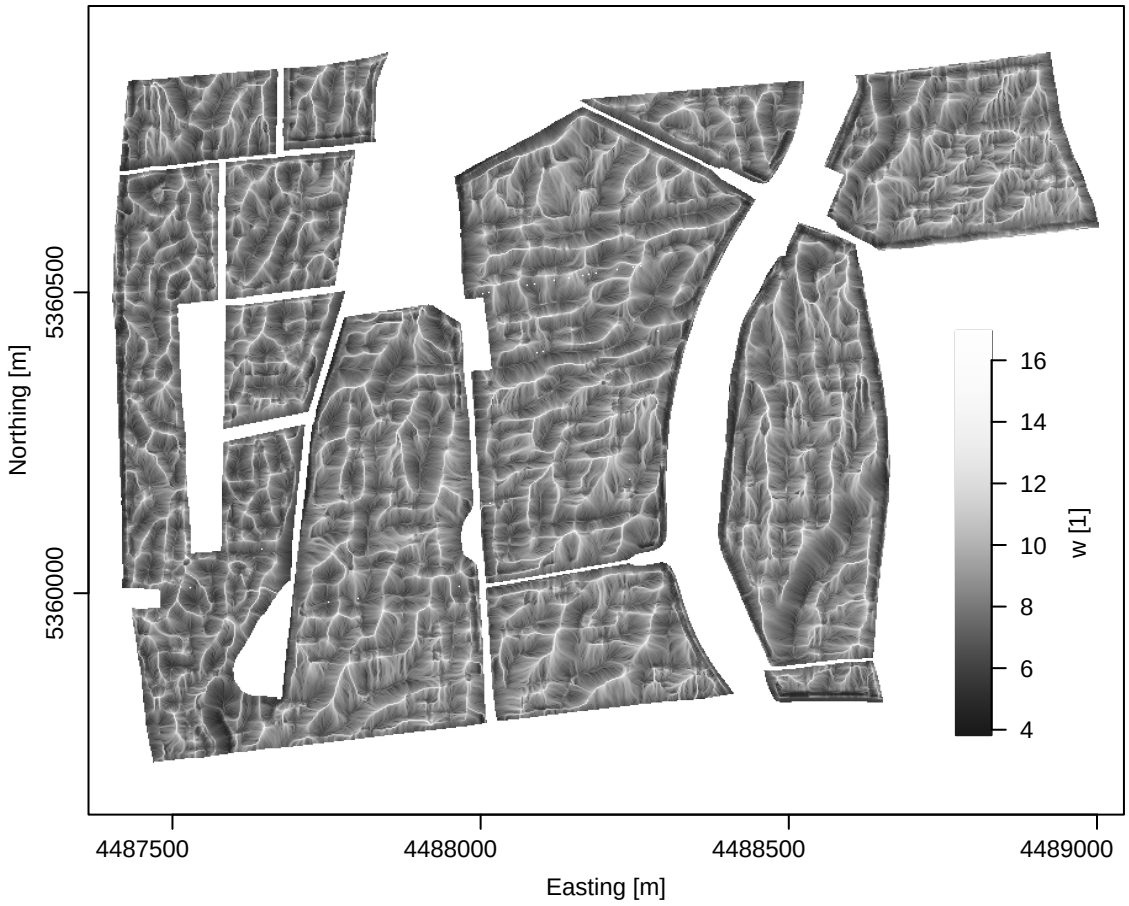

Figure 6.4: 2 m×2 m grid of wetness index (w) derived from upslope contributing area (A_s) and steepest slope angle (γ) according to equation (5.1). A_s and γ have been computed from a digital elevation model (DEM) with GRASS (GRASS Development Team, 2011).

The map of apparent electrical conductivity of the ground (σ_a) exhibits two obvious patterns (figure 6.5). Firstly, the distinct areas of high σ_a at the south-west and north-west edges of the study site. Both areas correspond to deep non-degraded peat layers (z_s from 0.3 m to 1.4 m), partly with intercalated ochre, found during the ground truth sampling (compare figure A.1a and d). Secondly, curvilinear features of increased σ_a appear, whose main direction corresponds to the terraced medium scale topographic features visible on the map of z_w (figure 6.3). These curvilinear features correspond to the small scale topographic patterns observable on the maps of z_w and w. Compared to the smoothly undulating characteristic of these patterns observable on the DEM (figure 5.3) and the map of z_w, respectively the sharpened characteristic on the map of w, the patterns appear with a medium characteristic on the map of σ_a.

6.3 Structural semivariogram analysis

The semivariogram of transformed z_w was modelled with a nested structure containing a short range Gaussian structure and a long range spherical structure. The practical range of the Gaussian structure was 60 m; the range of the spherical structure was 380 m. The Gaussian structure was attributed to the small scale smoothly undulating patterns (Goovaerts, 1997) in the topography of the study site which is reflected in z_w. The spherical structure seems related to the terraced topography pattern (figure 6.6a).

The semivariogram of w was modelled with a single short range exponential structure with a practical range of 24 m, attributed to the small scale topography response of w, which reflects water movement in the landscape (figure 6.6b). The steep linear behaviour at the origin of the

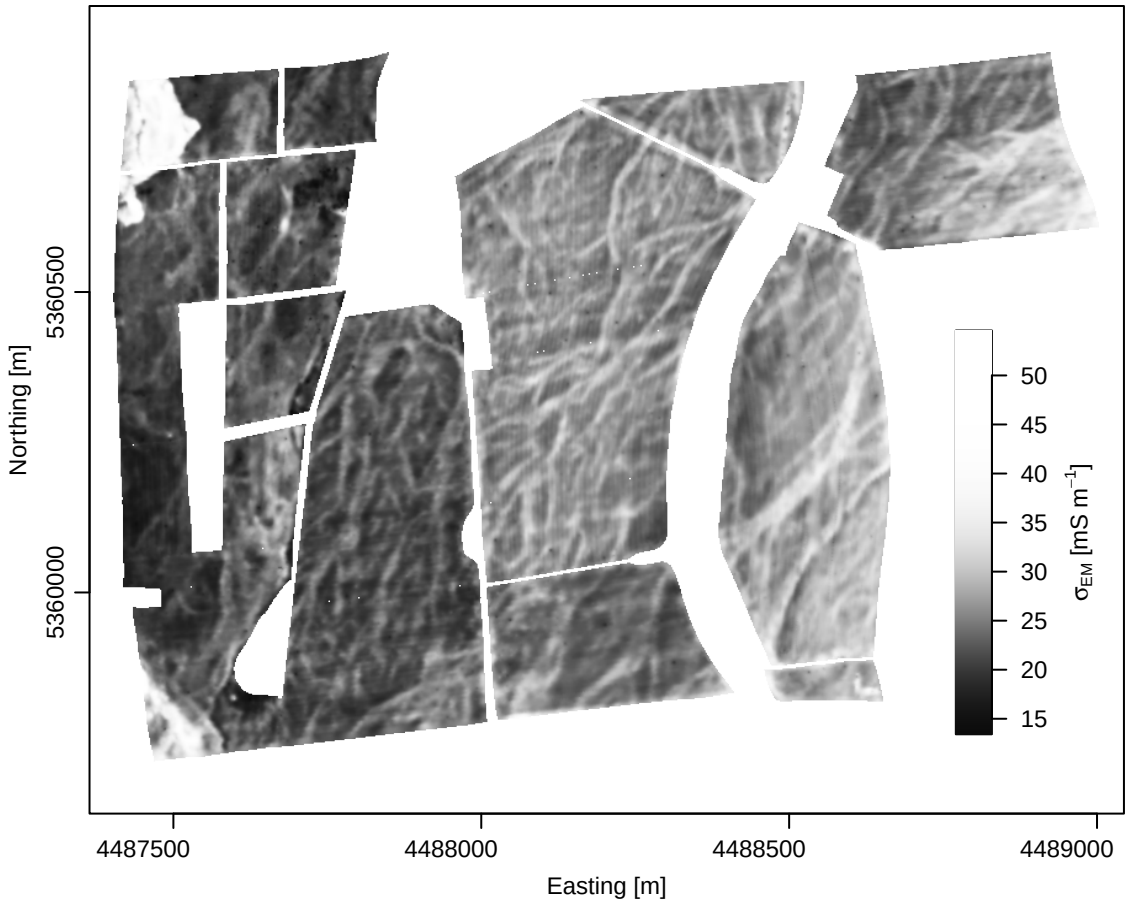

Figure 6.5: 2 m×2 m grid of apparent electrical conductivity of the ground (σ_{a}), obtained by ordinary kriging with the data from an extensive σ_{a}-survey with on average 765 measurements per hectare (chapter 2). A nested semivariogram model obtained by a structural analysis (figure 6.6c) was used for kriging each grid cell with data in a neighbourhood of 10 m radius.

exponential model is in line with the larger contrasts at short distances due to accumulation in the curvilinear channels expressed in w.

As σ_{a} was expected to be controlled amongst others by z_{w} and soil moisture, its semivariogram was modelled by a nested structure containing those used to model the semivariograms of transformed z_{w} ($R(z_{\mathrm{w}})$) and w. No additional structures but a nugget effect were needed to obtain a satisfying fit of the semivariogram of σ_{a} (figure 6.6c). The fact that the short range structure of σ_{a} could be modelled with the structures attributed to smoothly undulating topography and topography response of w is in accordance with the intermediate characteristic of small scale patterns on the map of σ_{a}.

The semivariogram of transformed z_{s} ($R(z_{\mathrm{s}})$) was modelled with the same structures used for modelling of the three above mentioned semivariograms. This was supported by the expectation that z_{s} is controlled by the same geomorphological processes as small scale topography (Gaussian structure) and water accumulation (exponential structure). A similar rationale can be provided for the spherical structure because soil development can be influenced by groundwater (Baker et al., 2004). This is obvious from the occurrence of thick peat horizons in the part of the study site where groundwater is especially shallow.

The short range exponential structure appeared to be predominant on short lags of the semivariogram of $R(z_{\mathrm{s}})$, which can be expected to be hardly influenced by a trend (Goovaerts, 1997). Additionally, it was the only structure in the semivariogram of w, which was not used as a covariate in equation (5.2), and thus should remain in the residual structure of $R(z_{\mathrm{s}})$ (Kitanidis, 1993). Thus, the short range exponential structure was used in the generalised least squares (GLS) fit of the trend model as residual spatial autocorrelation structure.

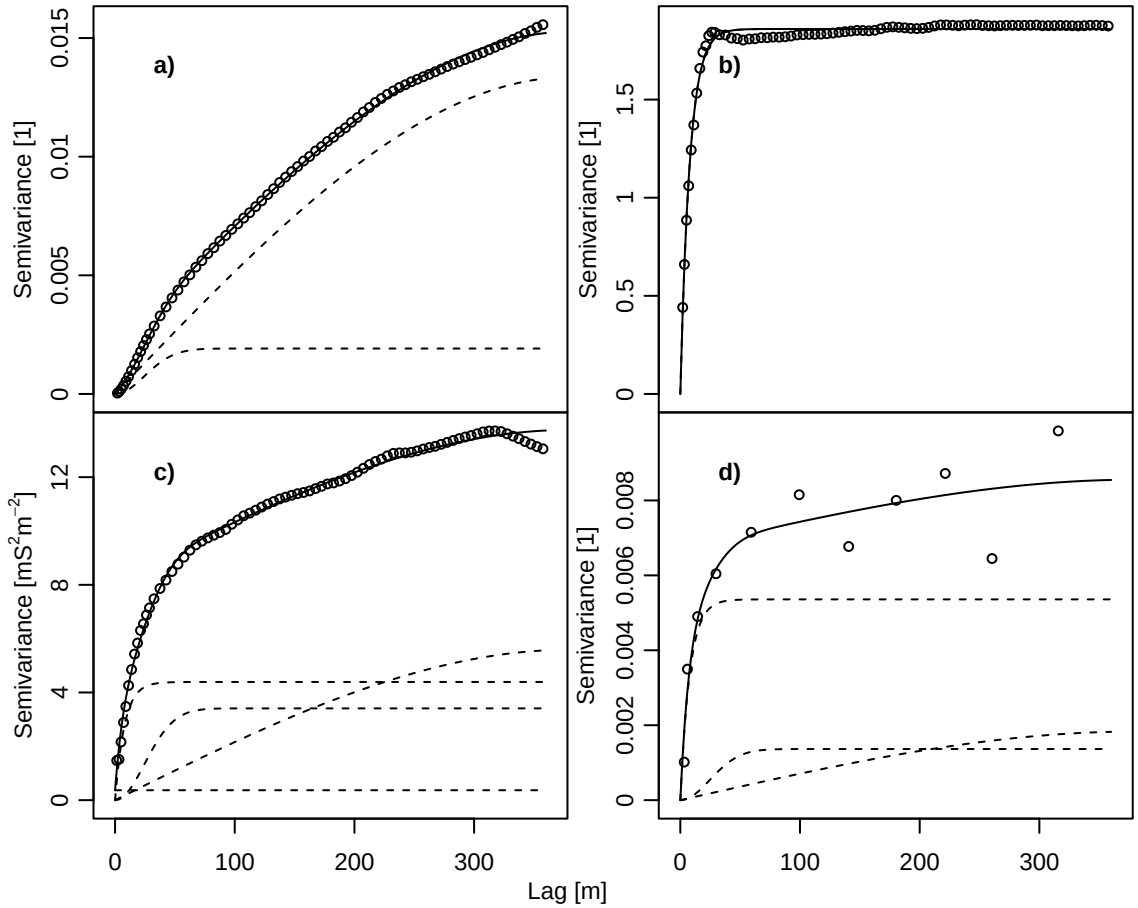

Figure 6.6: Experimental semivariograms (points) and semivariogram models (continuous lines) of a) transformed groundwater table depth ($R(z_{\mathrm{w}})$), b) wetness index (w), c) apparent electrical conductivity of the ground (σ_{a}) and d) transformed soil thickness ($R(z_{\mathrm{s}})$). Dashed lines show the basic semivariogram models contained in the nested semivariogram models: a spherical model with a range of 380 m (a), c) and d)), a Gaussian model with a practical range (Journel and Huijbregts, 1978) of 60 m (a), c) and d)), an exponential model with a practical range of 24 m (c), d) and the only structure in b)) and a nugget effect (c)).

6.4 Prediction of soil thickness and model evaluation

For 81 % of the locally fitted trend models, at least one of σ_{a} and $R(z_{\mathrm{w}})$ exhibited a regression coefficient representing a slope that differed significantly from zero on a 10 % confidence level. The regression coefficient associated to $R(z_{\mathrm{w}})$ was significant for 26 % of the fitted models. The relaxed confidence level of 10 % was chosen because the model was fitted to small neighbourhoods consisting of few points. Including only sampling sites exhibiting the same layer configuration as the prediction location (either $z_{\mathrm{w}} > z_{\mathrm{s}}$ or $z_{\mathrm{w}} < z_{\mathrm{s}}$) in the local fitting of the trend model did not allow selecting at least 10 sampling points within a search radius of 360 m for six sampling sites, which thus were omitted in this approach. Of the remaining sites, 79 % exhibited at least one significant coefficient. For 30 % of these fits, $R(z_{\mathrm{w}})$ exhibited a significant coefficient. For 2 % respectively 4 % of the fits, $R(z_{\mathrm{w}})$ was the only covariate associated with a significant coefficient (table 6.1).

In terms of the RMSE of the back transformed response, the prediction error was less than 5 cm for 30 % of the locally fitted trend models when all sampling sites were included. Including only sampling sites exhibiting the same layer configuration resulted in a RMSE of less than 5 cm for 37 % of the fitted models (table 6.1). From those sampling sites, where at least 20 neighbouring sites were located within a search radius of 100 m, 64 % respectively 69 % (as can be calculated from the numbers in table 6.1) exhibited a RMSE of less than 5 cm. Additionally, almost all of those sampling sites exhibited a significant coefficient for σ_{a} and more than half of

Table 6.1: Proportions ([%]) of local fits of the trend model that met the conditions given in both the respective row and column.

	a)[a]					b)[b]				
	p_{β_1}[c] < 0.1	p_{β_2}[d] < 0.1	η[e] < 0.05	r[f] <|	r[f] >|	p_{β_1}[c] < 0.1	p_{β_2}[d] < 0.1	η[e] < 0.05	r[f] <|	r[f] >|
p_{β_1}[c] < 0.1	79					75				
p_{β_2}[d] < 0.1	24	26				26	30			
η[e] < 0.05	29	15	30			31	18	37		
r[f] $\leq$ 100	25	14	16	25		25	15	18	26	
r[f] > 100	54	12	13	0	75	50	15	20	0	74

[a] All sampling sites used in neighbourhood selection
[b] Only sampling sites exhibiting the same layer configuration as the prediction location (either $z_w > z_s$ or $z_w < z_s$) used in neighbourhood selection
[c] p-value associated to β_1 in equation (5.2)
[d] p-value associated to β_2 in equation (5.2)
[e] Root mean squared error (RMSE) of back transformed local fits [m]
[f] Radius of the neighbourhood used for fitting [m]

Table 6.2: Summary of the measures of goodness of fit for local fits of the trend model.

	a)[a]		b)[b]	
	η[c] [m]	e[d] [m]	η[c] [m]	e[d] [m]
minimum	0.02	0.00	0.02	0.00
1st quartile	0.04	0.02	0.04	0.02
median	0.07	0.04	0.06	0.04
4th quartile	0.10	0.09	0.08	0.08
maximum	0.34	1.21	0.30	0.53

[a] All sampling sites used in neighbourhood selection
[b] Only sampling sites exhibiting the same layer configuration as the prediction location (either $z_w > z_s$ or $z_w < z_s$) used in neighbourhood selection
[c] Root mean squared error (RMSE) of back transformed local fits [m]
[d] Absolute residual of cross-validation [m]

them for $R(z_w)$. This indicates that for a search radius of 100 m, the assumption of homogeneous layers was appropriate and the variability within the neighbourhood sufficient for a reliable model fit when including 20 sampling sites. For larger search radii, still about two thirds of the corresponding fits exhibited significant coefficients (table 6.1). A Wilcoxon matched pairs signed rank test on the RMSEs of the back transformed model response showed that the fits using only consistent layer configurations performed significantly better (p<0.001).

The cross-validation approach revealed, besides considerably larger maximum residuals, that the error of single predictions in the centre of the neighbourhoods was of the same order of magnitude as the RMSEs obtained for each fit individually (table 6.2). While a maximal residual of 1.21 m occurred when all sampling sites were used in the fitting procedure, this could be reduced to 0.34 m, when only sampling sites exhibiting the same layer configuration were used in the fit procedure (table 6.2; figure 6.7). The overall RMSEs obtained in cross-validation were 0.14 m

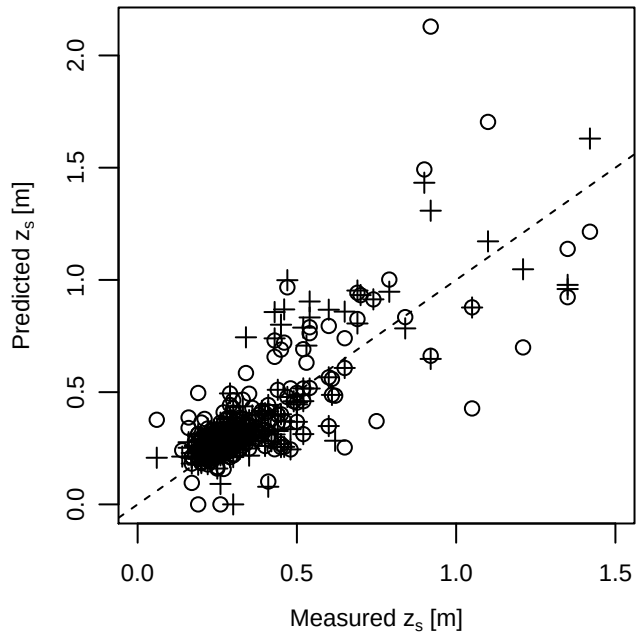

Figure 6.7: Soil thickness (z_s) predicted in a cross-validation approach plotted against measured values. Points are derived from fitting the trend model with all sampling sites in the neighbourhood irrespective of the layer configuration ($n = 297$), crosses with only sampling sites of the same layer configuration as the prediction location (either $z_w > z_s$ or $z_w < z_s$; $n = 291$). The dashed line is the 1:1 line.

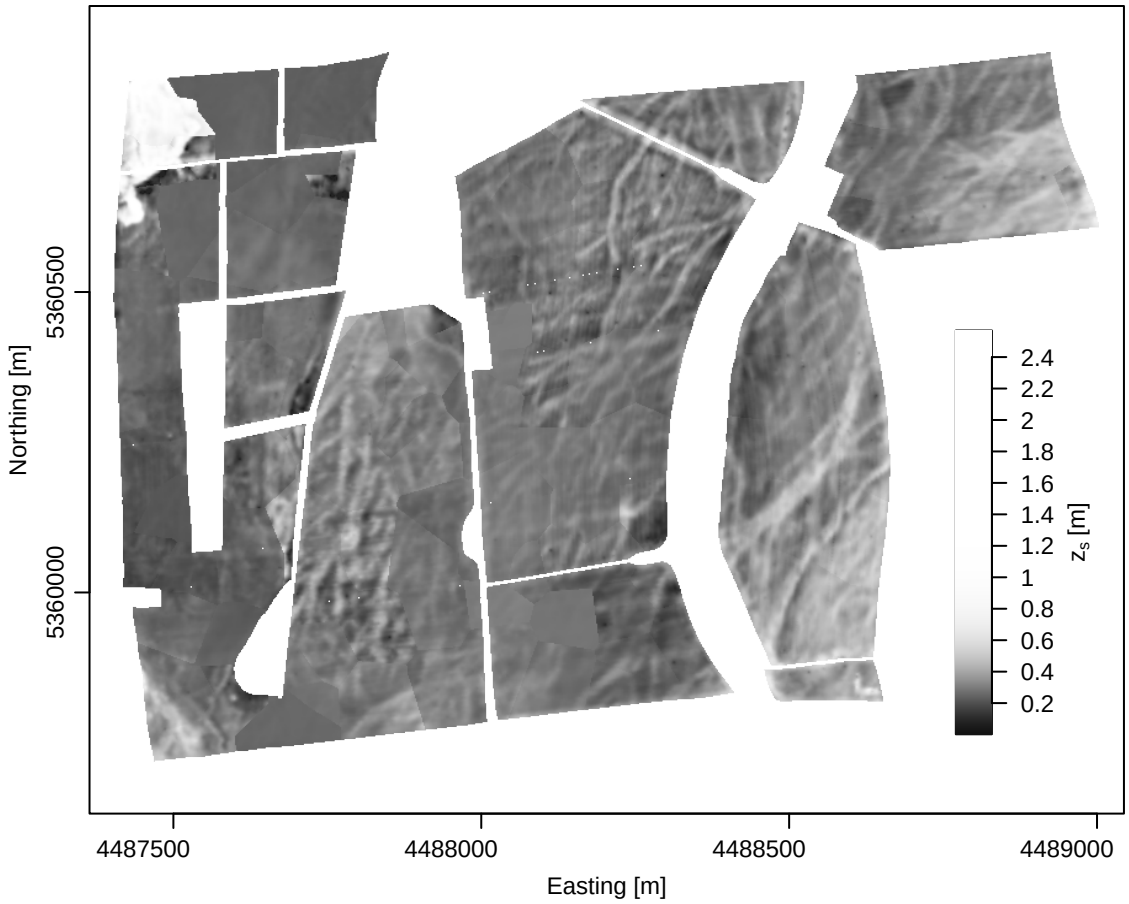

Figure 6.8: 2 m×2 m grid of soil thickness (z_s) as predicted by the physically based trend model expressed in equation (5.2). The model was fitted within local neighbourhoods of sampling sites and the prediction of each grid cell executed with the coefficients associated to the nearest neighbour sampling site.

and 0.12 m respectively. The mean errors obtained in cross-validation were 0.02 m respectively 0.01 m, indicating that the prediction of z_s was not considerably biased.

The map of predicted z_s mainly exhibits the same small scale patterns as the maps of σ_a, z_w and w (figure 6.8). The areas with deep non-degraded peat layers in the south-west and north-west edges of the study site are clearly visible, though the limit of the respective area in the north-west edge is displaced. This displacement occurred due to the breaklines between the Thiessen polygons, within which the fitting was applied. These breaklines were not necessarily colocated with physical breaklines. Breaklines are also clearly visible around sampling sites, where either σ_a or both covariates of the linear model failed to predict z_s. In these areas, as the coefficients of the regression model were not significant, no variability of soil thickness could be explained. Hence the flat and homogeneous appearance of the corresponding parts of the map.

7 Discussion

7.1 High resolution mapping of auxiliary variables

Extensive mapping of environmental variables at a sub-field scale requires detailed and accurate data.

Accuracy is required in the domain of the measured variables, because there is no use of a high resolution map exhibiting much noise and little signal. Where the signal can be distinguished from noise, the noise can be filtered by means of interpolation. Further, in the analysis of extensive datasets such as digital elevation models (DEM) or extensively measured apparent electrical conductivity of the ground (σ_a), interpolation filters erroneous single measurements, which cannot be efficiently detected by visual inspection. This effect has been used in the present study to obtain reliable estimates of true σ_a at soil sampling sites as well as on the 2 m$\times$2 m grid used for interpolation of soil thickness (z_s). Noise filtering was applied to the DEM, because filtering of DEMs is a necessary step to obtain plausible results of terrain analysis (Hengl et al., 2004).

High resolution mapping of groundwater table height generally suffers from spatially sparse datasets (Buchanan and Triantafilis, 2009; Rouhani and Myers, 1990). In this case, the main goal of interpolation is not noise filtering but the accurate prediction at unmeasured locations. The present study used an approach based on physical knowledge of the processes that generate the shape of the water table (chapter 3). However, short range spatial patterns in table height could not be observed from the sparse wells and thus could not be modelled. But spatial variations in groundwater table height at the scale of the undulating patterns in topography are conceivable due to preferential recharge within the concavities of these patterns (Böhlke, 2002). The generally accurate predictions of table height and the physical explanations of the observed patterns, however, allow to conceive the generated map as being reasonably accurate at the used scale and resolution.

Positional accuracy is of equal concern for the assessment of spatial variation and co-variation as accuracy in the domain of measured variables (Cressie and Kornak, 2003; Grimm and Behrens, 2010). Measuring positions with an accuracy appropriate for the assessment of sub-field scale variability is possible with nowadays differential and Real Time Kinematic Global Positioning System (GPS) receivers (van Bergeijk et al., 1998). However, technical implications can lead to situations where the measured positions do not correspond exactly to the positions of interest (Speckmann, 2000). A solution for such an implication—an offset between GPS antenna and a trailed sensor—is presented in chapter 2. It reduced the positioning bias of the measurements of σ_a, such that a geostatistical estimation of measured σ_a-values from neighbouring values was possible with an error of the order of magnitude of measurement accuracy.

7.2 Process based assessment of spatial variation

The results of the present study give evidence of associations between physical relationships and semivariogram structures (section 6.3). The shared spatial patterns appearing on the maps of auxiliary variables suggest physical relationships between the variables (figure 5.3, figure 6.3 and figure 6.4, figure 6.5). This is confirmed by the structural analysis of their semivariograms. The semivariogram of σ_a exhibits both the Gaussian structure of the smoothly undulating topography reflected in groundwater table depth (z_w) and the exponential structure from the high-contrast wetness index (w; figure 6.6). Thus, σ_a is intermediate between both other variables, as it also appears from the maps. This reflects the property of σ_a of being an integrative parameter for many soil properties (Friedman, 2005). σ_a is dependent on soil moisture and texture (Auerswald et al., 2001; Friedman, 2005) and topography controls the spatial variation of soil moisture and texture (Moore et al., 1993; Rosenbloom et al., 2001; Western et al., 1999). In turn, σ_a shares

spatial structuring with topography as well as with topography derived parameters such as w, which reflects the accumulation of water in concavities of the land surface. This supports approaching a geostatistical analysis from a process based perspective. A process based approach to geostatistical analysis can be to assess the spatial structure of a variable from pure knowledge about the process that generated it, instead of applying a data driven approach (Kerry and Oliver, 2011). Another way is to explain soil spatial variability by means of physically related auxiliary variables (McBratney et al., 2003). In both cases, the sampling effort could be reduced, which otherwise would be needed for the estimation of the semivariogram or for direct assessment of a target variable (Kerry and Oliver, 2011; McBratney et al., 2003). Auxiliary variables can be incorporated in geostatistical modelling by the use of variable mean models. Whenever part of the variability of a target variable is related to a covariate via a known function describing the variable mean, this relationship can be used to get sharper predictions than with a completely stochastic model (Goovaerts, 1997; Kitanidis, 1993). In the present study, the use of a physically based variable mean model and structural semivariogram analysis were combined in both the prediction of groundwater table height (chapter 3) and of z_{s}. The semivariogram of transformed z_{s} ($R(z_{\mathrm{s}})$) was modelled using a set of basic semivariogram functions, of which the single structures have been chosen based on physical rationale. These structures were fitted to the experimental semivariograms of physically related high resolution auxiliary variables, and thus provided reliable estimates of the real spatial structures also present in $R(z_{\mathrm{s}})$.

Using prior knowledge about physical processes in the modelling and analysis of semivariograms allows interpreting the results with respect to these processes (Goulard and Voltz, 1992; Journel and Huijbregts, 1978). A viable interpretation can be given for the small scale spatial patterns appearing as curvilinear features on the maps of auxiliary variables and as short range structures in their semivariograms. A strong impression that arises from the curvilinear features is that of braided rivers. To underline this, an aerial photograph showing recent braided rivers exhibiting similar features is given in figure A.3 to be compared with figure 5.3. The study site lies in an outwash plain (Münchner Schotterebene; Traub, 1956) with shallow soils over glacial gravels. The latter likely exhibit a paleotopography that has been formed by braided rivers. Then, the recent alluvial soil is a filling of the channels formed by the braided rivers and the actual topography is a subdued replica of the paleotopography. Thus, the patterns of braided rivers were observable in the DEM. The filling of channels of former braided rivers with alluvium has been observed for another flood plain in Germany (Hagedorn and Rother, 1992), which is in line with the finding, that z_{s} could be predicted by using covariates that are related with topography and accumulation of water and solid material.

7.3 Predicting soil thickness with a physically based model

The prediction of layer depth with σ_{a} as well as with topography derived parameters as covariates is quite common in the literature and this has been highlighted already in the introduction (chapter 1). The reported findings often correspond with the findings in the present study. Saey et al. (2008) reconstructed a paleotopography by assessing the thickness of a loess cover by means of σ_{a}. Bourennane et al. (2000) predicted the thickness of a silty-clay-loam horizon using slope gradient as a covariate in a flat area, which exhibited a mean slope of 0.5 % when it was derived from a 20 m$\times$20 m DEM (King et al., 1999). Though their results have been obtained at larger scale and coarser resolution, they agree with the finding of the present study, that z_{s} is related to topography even in a relatively flat terrain. However, in an agriculturally used anthropogenic landscape, topography not necessarily still exhibits the shape which lead to the actual z_{s}. Moreover, anthropogenic processes might have altered z_{s} (Kuriakose et al., 2009). The study area of the present study has an agricultural landuse history. The peat soil site has been used as permanent grassland for meanwhile over 50 years. The mineral soil site has been used as

arable land for over 40 years before conversion to grassland between 1997 and 2000 (Schnyder et al., 2006). Such landuse history suggests that the terrain has been flattened by the use of rollers on grassland and especially by tillage during the use as arable land of the mineral soil site (Van Oost et al., 2005). This is supported by the fact, that the small scale patterns of topography appear smoother and of larger extend on the mineral soil site (compare figure 5.1 and figure 5.3). Such flattening renders it useful for the assessment of z_{s} to not rely solely on topography derived parameters, but to make use of parameters that ''look into'' the soil. Such parameters, e.g. σ_{a}, can reveal the effects of past processes. Francés and Lubczynski (2011) used topography derived parameters and σ_{a} to predict topsoil thickness in a geostatistical approach. The present study combines both topography derived parameters and σ_{a} in a physically based statistical model, which additionally makes use of the dependence of σ_{a} on shallow groundwater.

There have been other attempts to incorporate the physically based depth response functions of σ_{a} (chapter 4) in models for the prediction of z_{s}. Saey et al. (2008) have build an objective function based on the depth response function of the vertically oriented EM38 ($R(z)$). That way, they minimised the difference between measured and predicted depth of the limit between two layers. Under the assumption of spatially homogeneous layers that vary only in depth, a single relationship between σ_{a} and layer depth was retrieved for the whole study site. Saey et al. (2009) extended the approach by additionally incorporating the depth response of the horizontally oriented EM38 into the objective function. However, the use of multiple σ_{a}-sensors and their depth response functions did not prove to give considerably more accurate predictions of topsoil depths (Sudduth et al., 2010). Additionally, the approach is still limited to the assumption of the ground being consistent of two homogeneous layers within the extend of the domain under study (Saey et al., 2009; Sudduth et al., 2010). In the present study, the assumption of homogeneous layers has been generalised to an arbitrary number of homogeneous layers, n. The prediction of the depth of one layer is then based on σ_{a} and the depths of the remaining $n-1$ layers (equation (4.6)). Based on this general model, a specific model was build for the prediction of z_{s} by using σ_{a} and z_{w} as covariates. By fitting the resulting regression model to small neighbourhoods around the prediction locations instead of assuming a unique relationship for the whole study site, the restriction to homogeneous layers over the whole study site could be removed.

In spite of the heterogeneous soils on the study site (section 6.1), the prediction of z_{s} was effective. The accuracy was of the same order of magnitude as could be obtained with previous physically based models, which have been applied on smaller study sites exhibiting a single soil type. In the present study a root mean squared error (RMSE) of 0.12 m was obtained on 116 ha. Sudduth et al. (2010) obtained at least 0.11 m on 13 ha for the prediction of depth to an argillic horizon on a claypan soil. Saey et al. (2008) and Saey et al. (2009) obtained RMSEs of 0.22 m respectively 0.26 m on 2 ha for the prediction of the thickness of loess over a clayey subsoil. Considering the magnitude of small and micro scale variability of z_{s} (see section 6.1), the magnitude of the RMSE obtained in the present study shows that it consists to a considerable part of such variability. Another effect contributing to prediction error is the definition of z_{s}, given in section 5.3 as ''the distance between ground surface and the top of the gravely substrate within which no considerable signs of soil formation or mixing with soil are visible''. A similar definition is given by Kuriakose et al. (2009) as ''the depth from the surface to more-or-less consolidated material''. Both definitions reflect that there is not always a sharp discordance between soil and subsoil (compare also figure A.2). But, if build on σ_{a}-depth response functions, present attempts to predict z_{s} incorporate the assumption of discrete layers. Obviously, this can only be a simplified notion of reality. Thus, the predictions with such models can be seen as (at least possibly) accurate predictions of a naturally fuzzy variable.

Predicting z_{s} can be performed with similar accuracy, regardless of whether regression models are based on whatever function might fit the data or on physically based functions

(e.g. Sudduth et al., 2010). However, purely statistical relationships are never more than time and site specific (Boettinger et al., 1997). Contrarily, some generalisation is possible within the domain of a physically based model. Saey et al. (2009) even presented a solution to predict depth without any calibration, though this seems hardly generally possible. The possibility to generalise has been shown in the present study by the fact, that accurate predictions of z_{s} were possible on a heterogeneous site and by the comparison of predictions based on two different neighbourhood selections. Including all sampling sites, regardless of the layer configuration, lead to large residuals at locations where the layer configuration was not consistent within the neighbourhood. Including only sampling sites with consistent layer configuration in the neighbourhood lead to more accurate predictions (table 6.2). However, the latter failed completely in the present implementation, where not enough sampling sites with consistent layer configuration could be found within a search radius of 360 m. The failure to predict z_{s} underlined the physical meaning of the model, if no neighbouring sampling sites exhibited consistent layer configuration, as no model can be fitted to a single point.

However, this can impede mapping without extensive ground truth sampling. At the used study site, especially high proportions of accurate fits and significant regression coefficients occurred at neighbourhoods with more than 20 points within a search radius of 100 m. This corresponds to a sampling density of more than 6 points per hectare, or a spacing of less than 40 m when sampling on a regular grid. Thus, more extensive sampling would have been needed to accurately assess the physical relationship throughout the whole study site. But with regard to the fuzziness of the definition of z_{s} and its micro scale variability observed during soil sampling (section 6.1), it is at the one hand questionable whether this would lead to more accurate predictions, and at the other hand the predictions obtained with the current sampling design can already be deemed ‘‘exact’’.

Moving towards continuously varying trend coefficients is another way to assess the physical relationship throughout the whole study site. In the current approach, response and covariates are treated as continuously varying in space. But when mapping, their relationship is discretised to the Thiessen polygons around sampling sites, as is noticeable on the interpolated map of z_{s} (figure 6.8). Moving towards a continuously varying relationship leads to a more realistic appearance of the map and to a more correct representation of the continuous nature of the phenomenon under study. A common geostatistical method, kriging with external drift (Goovaerts, 1997), estimates the regression coefficients within neighbourhoods of the unsampled prediction locations instead of only neighbourhoods around sampling sites. However, this requires a unique function relating response and covariates throughout the whole study area. This is not given in a true sense where the layer configuration changes within the study area, and ignoring this leads to inaccurate predictions, as has been shown above. A possibility might be treating the regression coefficients themselves as continuous random functions. This would allow interpolating them to the desired resolution of the map prior to prediction of the response. However, further work is needed to carefully check the effects of the spatial disaggregation that takes place when moving from the neighbourhood support of the fitted coefficients to the smaller support of interpolated coefficients (Heuvelink and Pebesma, 1999).

Unobserved small scale spatial variations in groundwater table height might have lead to an underestimation of the correlation between σ_{a} and transformed z_{w} ($R(z_{\mathrm{w}})$). In turn, this is a possible cause of the regression coefficient associated with $R(z_{\mathrm{w}})$ in the linear trend model being insignificant at the majority of sampling sites. However, it was the only significant coefficient at some sampling sites (table 6.1), possibly caused by a direct effect on peat soil thickness through the retarding effect on peat decomposition of a shallow water table (Gorham, 1991; Kasimir-Klemedtsson et al., 1997). Thus, omitting z_{w} as a covariate, though globally possibly of no great effect, would have locally impeded a reasonable prediction.

8 Conclusions

The physical relations between soil thickness (z_s), topography, shallow groundwater and apparent electrical conductivity of the ground (σ_a) have been shown. They were effectively exploited for the prediction of z_s. The existence and form of the relations was derived from theoretical considerations, upon which a regression model was build. A spatially explicit approach was used to fit the model, including a process based structural analysis of the semivariograms of involved variables. This lead to sufficiently accurate predictions of z_s, despite the heterogeneous soils at the study site. The prediction error was of similar magnitude as micro scale spatial variation of soil thickness, which occurred within the support of the auxiliary variables.

The kinematic model, developed for the estimation of sensor positions in on-the-go applications, reduced the apparent prediction error of σ_a below the measurement error. Thus in general, it offers the possibility to improve the quality of high resolution maps obtained from on-the-go sensor measurements. The application in the present study underlines its usefulness for the analysis of spatially covarying high resolution auxiliary variables, within which accurate positioning is especially a concern for the assessment of short range spatial relations.

The physical conceptual model of the groundwater table explained most of the variability in table height data at the study site. The unexplained variation was in an order of magnitude of few decimetres. Thus, the model captured the majority of processes generating the shape of the water table. Hence, the present study provides a proof of concept for the use of physically based variable mean models in groundwater table mapping. Within this study, the use of the concept resulted in predictions of the groundwater table, which, in conjunction with topography and σ_a, had predictive capability in the assessment of z_s.

The physically based model for the prediction of z_s allowed some generalisation to different configurations of layering in the ground. Thus, it exhibits validity beyond being a mere site specific regression model. However, different study sites might exhibit properties that require building different relationships into a model suitable for explaining soil thickness. But from the general model equation developed in the present study, specific models for the prediction of layer depths with σ_a can readily be build.

Overall, the methods and results presented in this study give evidence, that physical reality is worth being considered explicitly in the formulation of models for variables in different applications. Not only the understanding of a variable in its physical context is improved, but also its predictions can be evaluated quantitatively and qualitatively with respect to physical reality.

Acknowledgements

I appreciate the support of my supervisor, Prof. Karl Auerswald, who presumably carried most of the burden to make me turn input into output. His ideas and his knowledge provided much of the material this dissertation is made of.

I also appreciate the help of Richard Wenzel, who conducted the conductivity survey and measurements of groundwater table height. Further, Moritz Wetzel, Georg Vogel, Eduard Buckl, the team of Grünschwaige research station (and many others who provided help) were indispensable for the soil sampling campaign.

Ulrike Ostler and her patience were especially essential for the development of the model in chapter 2 but always a support.

The provision of groundwater table height data by the Wasserwirtschaftsamt München and Flughafen München GmbH powered the model presented in chapter 3.

Last but not least, Prof. Schnyder, Melitta Sternkopf and the whole team of the Lehrstuhl für Grünlandlehre are accountable for the support and the good times I had at the Lehrstuhl.

A Colour photographs

Figure A.1: Exemplary photographs of characteristic soil profiles. Two soil cores shown in one photograph have been excavated at a distance of approximately 0.5 m between each other. a) Deep peat soil, degraded near the surface due to aeration and intact in depth. b) Shallow peat soil, degraded throughout the whole profile. c) Shallow soil consisting of a single layer of humic mineral soil. d) Profile with alternating horizons of mineral soil, ochre and peat. e) Humic mineral soil with a loamy horizon of varying thickness between topsoil and gravelly substrate.

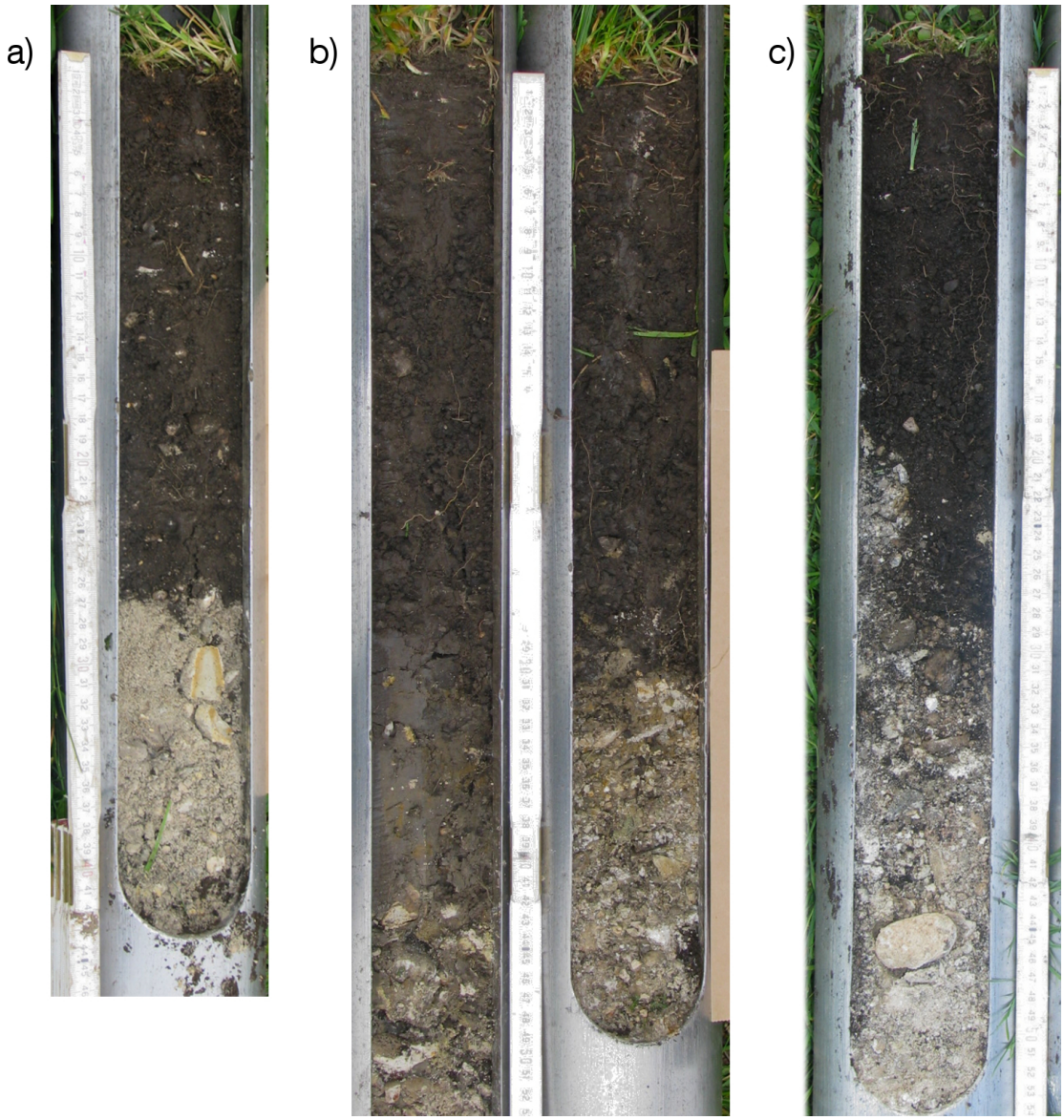

Figure A.2: Exemplary photographs illustrating different characteristics of the limit between soil and gravelly substrate: a) Sharp discordance, b) gradual change in proportion of gravel without clear limit and of varying extent, c) micro scale variability of soil thickness (z_s) within the extend of the probe.

Table A.1: Characteristics of soil profiles shown in figure A.1 and figure A.2.

	Easting[a] [m]	Northing[a] [m]	z_s[b] [m]	z_w[c] [m]	w[d] [1]	σ_a[e] [mS m^{-1}]
Figure A.1a	4487469	5360839	0.92	0.28	10.6	50.1
Figure A.1b	4487522	5360041	0.20	0.29	12.8	19.8
Figure A.1c	4488232	5359849	0.27	0.48	8.2	23.7
Figure A.1d	4487468	5359835	0.62	0.67	7.5	39.7
Figure A.1e	4488811	5360861	0.40	0.86	9.9	26.9
Figure A.2a	4488434	5360354	0.25	0.71	9.0	22.7
Figure A.2b	4487516	5359960	0.32	0.58	7.0	19.1
Figure A.2c	4488194	5360357	0.37	0.70	10.1	31.7

[a] Click on coordinates in the PDF-version shows sampling location on aerial photograph in a web browser
[b] Soil thickness
[c] Groundwater table depth
[d] Wetness index (equation (5.1))
[e] Apparent electrical conductivity of the ground

Figure A.3: Braided rivers form the mouth of the Rißbach at the upper course of the river Isar in the Bavarian Alps. Aerial photograph: © **Bayersiche Vermessungsverwaltung (www.geodaten.bayern.de)**.

B Notations and acronyms

A_s . . . . . upslope contributing area (land-surface parameter)

DEM . . . . . digital elevation model

EM38 . . . . . ground conductivity meter operating at low induction numbers (Geonics Ltd., Mississauga, Canada)

γ . . . . . steepest slope angle (land-surface parameter)

GLS . . . . . generalised least squares

GNSS . . . . . global navigation satellite system

GPS . . . . . Global Positioning System (GNSS operated by the United States Department of Defense)

R . . . . . function mapping depth divided by the intercoil spacing of the σ_a-measurement instrument (z) to the relative contribution of the halfspace below z to the σ_a-signal (cumulative depth response function; equation (4.2)). For simplicity, the output of R, $R(z)$, is referred to as ''transformed layer depth''

R^2 . . . . . coefficient of determination

RMSE . . . . . root mean squared error

σ_a . . . . . apparent electrical conductivity of the ground

σ_i . . . . . electrical conductivity of the ith (counted from the ground surface) homogeneous layer of the ground

w . . . . . wetness index (land-surface parameter, equation (5.1))

z . . . . . depth below the σ_a-measurement instrument, divided by the intercoil spacing of the instrument

z_i . . . . . distance between ground surface and the lower limit of the ith (counted from the ground surface) homogeneous layer, divided by the intercoil spacing of the σ_a-measurement instrument

z_s . . . . . soil thickness (distance between ground surface and the top of the gravely substrate within which no considerable signs of soil formation or mixing with soil are visible) or soil thickness divided by the intercoil spacing of the EM38

z_w . . . . . groundwater table depth (distance between ground surface and water table) or groundwater table depth divided by the intercoil spacing of the EM38

List of Figures

List of Tables

Bibliography

Adamchuk, V. I., Hummel, J. W., Morgan, M. T. and Upadhyaya, S. K. (2004): On-the-go soil sensors for precision agriculture, Computers and Electronics in Agriculture **44**(1): 71–91.

Afzal, M. and Adams, W. A. (1992): Heterogeneity of soil mineral nitrogen in pasture grazed by cattle, Soil Science Society of America Journal **56**(4): 1160–1166.

Atkinson, P. M. and Tate, N. J. (2000): Spatial scale problems and geostatistical solutions: A review, Professional Geographer **52**(4): 607–623.

Auernhammer, H. (2001): Precision farming - the environmental challenge, Computers and Electronics in Agriculture **30**(1-3): 31–43.

Auerswald, K., Simon, S. and Stanjek, H. (2001): Influence of soil properties on electrical conductivity under humid water regimes, Soil Science **166**(6): 382–390.

Baker, B. J., Fausey, N. R. and Islam, K. R. (2004): Comparison of soil physical properties under two different water table management regimes, Soil Science Society of America Journal **68**(6): 1973–1981.

Baker, J. L. and Johnson, H. P. (1981): Nitrate-nitrogen in tile drainage as affected by fertilization, Journal of Environmental Quality **10**(4): 519–522.

Birrell, S. J., Sudduth, K. A. and Borgelt, S. C. (1996): Comparison of sensors and techniques for crop yield mapping, Computers and Electronics in Agriculture **14**(2-3): 215–233.

Bivand, R. S., Pebesma, E. J. and Gómez-Rubio, V. (2008): Applied spatial data analysis with R, Use R!, Springer, New York.

Boettinger, J. L., Doolittle, J. A., West, N. E., Bork, E. W. and Schupp, E. W. (1997): Nondestructive assessment of rangeland soil depth to petrocalcic horizon using electromagnetic induction, Arid Soil Research and Rehabilitation **11**(4): 375–390.

Bork, E. W., West, N. E., Doolittle, J. A. and Boettinger, J. L. (1998): Soil depth assessment of sagebrush grazing treatments using electromagnetic induction, Journal of Range Management S. 469–474.

Bourennane, H. and King, D. (2003): Using multiple external drifts to estimate a soil variable, Geoderma **114**(1-2): 1–18.

Bourennane, H., King, D. and Couturier, A. (2000): Comparison of kriging with external drift and simple linear regression for predicting soil horizon thickness with different sample densities, Geoderma **97**(3-4): 255–271.

Brevik, E. C., Fenton, T. E. and Lazari, A. (2006): Soil electrical conductivity as a function of soil water content and implications for soil mapping, Precision Agriculture **7**(6): 393–404.

Brolsma, R. J., van Beek, L. P. H. and Bierkens, M. F. P. (2010): Vegetation competition model for water and light limitation. II: spatial dynamics of groundwater and vegetation, Ecological Modelling **221**(10): 1364–1377.

Brus, D. J., Knotters, M., van Dooremolen, W. A., van Kernebeek, P. and van Seeters, R. J. M. (1992): The use of electromagnetic measurements of apparent soil electrical conductivity to predict the boulder clay depth, Geoderma **55**(1-2): 79–93.

Buchanan, S. and Triantafilis, J. (2009): Mapping water table depth using geophysical and environmental variables, Ground Water **47**(1): 80–96.

Bundesanstalt für Geowissenchaften und Rohstoffe (2008): Hydrogeologische Übersichtskarte von Deutschland (HÜK200).

Burrough, P. A., van Gaans, P. F. M. and Hootsmans, R. (1997): Continuous classification in soil survey: Spatial correlation, confusion and boundaries, Geoderma **77**(2-4): 115–135.

Böhlke, J. K. (2002): Groundwater recharge and agricultural contamination, Hydrogeology Journal **10**(1): 153–179.

Cassman, K. G. (1999): Ecological intensification of cereal production systems: Yield potential, soil quality, and precision agriculture, Proceedings of the National Academy of Sciences of the United States of America **96**(11): 5952–5959.

Ciminale, M., Gallo, D., Lasaponara, R. and Masini, N. (2009): A multiscale approach for reconstructing archaeological landscapes: Applications in northern apulia (Italy), Archaeological Prospection **16**(3): 143–153.

Corwin, D. L. and Lesch, S. M. (2005a): Apparent soil electrical conductivity measurements in agriculture, Computers and Electronics in Agriculture **46**(1-3): 11–43.

Corwin, D. L. and Lesch, S. M. (2005b): Characterizing soil spatial variability with apparent soil electrical conductivity, I. survey protocols, Computers and Electronics in Agriculture **46**(1-3): 103–133.

Corwin, D. L. and Plant, R. E. (2005): Applications of apparent soil electrical conductivity in precision agriculture (special issue), Computers and Electronics in Agriculture **46**(1-3).

Cressie, N. and Kornak, J. (2003): Spatial statistics in the presence of location error with an application to remote sensing of the environment, Statistical Science **18**(4): 436–456.

Dobos, E. and Hengl, T. (2009): Soil mapping applications, in T. Hengl and H. I. Reuter (eds), Geomorphometry, number 33 in Developments in soil science, Elsevier, S. 461–479.

Doolittle, J. A. and Collins, M. E. (1998): A comparison of EM induction and GPR methods in areas of karst, Geoderma **85**(1): 83–102.

Doolittle, J. A., Sudduth, K. A., Kitchen, N. R. and Indorante, S. J. (1994): Estimating depths to claypans using electromagnetic induction methods, Journal of Soil and Water Conservation **49**(6): 572 –575.

Erkert, T. W., Sessions, J. and Layton, R. D. (1989): A method for determining offtracking of multiple unit vehicle combinations, International Journal of Forest Engineering **1**(1): 9–16.

Ernst, L. F. (1978a): Drainage of undulating sandy soils with high groundwater tables: I. a drainage formula based on a constant hydraulic head ratio, Journal of Hydrology **39**(1-2): 1–30.

Ernst, L. F. (1978b): Drainage of undulating sandy soils with high groundwater tables: II. the variable hydraulic head ratio, Journal of Hydrology **39**(1-2): 31–50.

Fasbender, D., Peeters, L., Bogaert, P. and Dassargues, A. (2008): Bayesian data fusion applied to water table spatial mapping, Water Resources Research **44**(12): W12422.

Finke, P. A., Brus, D. J., Bierkens, M. F. P., Hoogland, T., Knotters, M. and de Vries, F. (2004): Mapping groundwater dynamics using multiple sources of exhaustive high resolution data, Geoderma **123**(1-2): 23–39.

Florinsky, I. (2005): Artificial lineaments in digital terrain modelling: Can operators of topographic variables cause them?, Mathematical Geology **37**(4): 357–372.

Francés, A. P. and Lubczynski, M. W. (2011): Topsoil thickness prediction at the catchment scale by integration of invasive sampling, surface geophysics, remote sensing and statistical modeling, Journal of Hydrology **405**(1-2): 31–47.

Freeland, R. S., Yoder, R. E., Ammons, J. T. and Leonard, L. L. (2002): Mobilized surveying of soil conductivity using electromagnetic induction, Applied Engineering in Agriculture **18**(1): 121–126.

Friedman, S. (2005): Soil properties influencing apparent electrical conductivity: a review, Computers and Electronics in Agriculture **46**(1-3): 45–70.

Ganskopp, D. C. and Johnson, D. D. (2007): GPS error in studies addressing animal movements and activities, Rangeland Ecology & Management **60**(4): 350–358.

Garlick, G. S., Kanga, D. N. and Miller, G. G. (1993): Vehicle offtracking: A globally stable solution, ITE Journal **63**(3): 17–21.

Geonics Limited: EM38, online: http://www.geonics.com/html/em38.html, cited 28 October 2011.

Goovaerts, P. (1997): Geostatistics for natural resources evaluation, Oxford University Press, New York.

Goovaerts, P. (2000): Geostatistical approaches for incorporating elevation into the spatial interpolation of rainfall, Journal of Hydrology **228**(1-2): 113–129.

Gorham, E. (1991): Northern peatlands: Role in the carbon cycle and probable responses to climatic warming, Ecological Applications **1**(2): 182.

Gottfried, T. (2008): Abhängigkeit der tiefenintegralen scheinbaren elektrischen Leitfähigkeit von Bodenmächtigkeit und Grundwasserflurabstand an einem Standort am Nordrand der Münchener Schotterebene, diploma thesis, Technische Universität München.

Gottfried, T., Auerswald, K. and Ostler, U. (2012): Kinematic correction for a spatial offset between sensor and position data in on-the-go sensor applications, Computers and Electronics in Agriculture **84**(0): 76–84.

Goulard, M. and Voltz, M. (1992): Linear coregionalization model – tools for estimation and choice of cross-variogram matrix, Mathematical Geology **24**(3): 269–286.

GRASS Development Team (2011): Geographic resources analysis support system (GRASS).

Grimm, R. and Behrens, T. (2010): Uncertainty analysis of sample locations within digital soil mapping approaches, Geoderma **155**(3-4): 154–163.

Grunwald, S. (2009): Multi-criteria characterization of recent digital soil mapping and modeling approaches, Geoderma **152**(3-4): 195–207.

Hagedorn, J. and Rother, N. (1992): Holocene floodplain evolution of small rivers in the uplands of lower saxony, germany, Geomorphology **4**(6): 423–432.

Hague, T., Marchant, J. A. and Tillett, N. D. (2000): Ground based sensing systems for autonomous agricultural vehicles, Computers and Electronics in Agriculture **25**(1-2): 11–28.

Haitjema, H. M. and Mitchell-Bruker, S. (2005): Are water tables a subdued replica of the topography?, Ground Water **43**: 781–786.

Haunschild, H. (1981): Erläuterungen zur Geologischen Karte von Bayern 1:500 000, Bayerisches Geologisches Landesamt, München: 3. neubearb. Aufl.

Hayes Jr., W. A. and Vepraskas, M. J. (2000): Morphological changes in soils produced when hydrology is altered by ditching, Soil Science Society of America Journal **64**(5): 1893–1904.

Heil, K. and Schmidhalter, U. (2012): Characterisation of soil texture variability using the apparent soil electrical conductivity at a highly variable site, Computers & Geosciences **39**(0): 98–110.

Hejcman, M. and Smrž, Z. (2010): Cropmarks in stands of cereals, legumes and winter rape indicate sub-soil archaeological features in the agricultural landscape of central europe, Agriculture Ecosystems & Environment **138**(3-4): 348–354.

Hengl, T. (2006): Finding the right pixel size, Computers & Geosciences **32**(9): 1283–1298.

Hengl, T., Gruber, S. and Shrestha, D. P. (2004): Reduction of errors in digital terrain parameters used in soil-landscape modelling, International Journal of Applied Earth Observation and Geoinformation **5**: 97–112.

Heuvelink, G. B. M. and Pebesma, E. J. (1999): Spatial aggregation and soil process modelling, Geoderma **89**(1-2): 47–65.

Heuvelink, G. B. M. and Webster, R. (2001): Modelling soil variation: past, present, and future, Geoderma **100**(3-4): 269–301.

Hiscock, K. (2005): Hydrogeology: principles and practice, Wiley-Blackwell, Malden, MA.

Hofierka, J., Mitášová, H. and Neteler, M. (2009): Geomorphometry in GRASS GIS, in T. Hengl and H. I. Reuter (eds), Geomorphometry, number 33 in Developments in soil science, Elsevier, S. 387–410.

Hoogland, T., Heuvelink, G. B. M. and Knotters, M. (2010): Mapping water-table depths over time to assess desiccation of groundwater-dependent ecosystems in the netherlands, Wetlands **30**(1): 137–147.

Hoover, K. and Wolman, M. (2005): Beyond the semivariogram: Patterns, scale, and hydrology in a semi-arid landscape, Advances in Water Resources **28**(9): 885–898.

Huisman, J. A., Hubbard, S. S., Redman, J. D. and Annan, A. P. (2003): Measuring soil water content with ground penetrating radar: A review, Vadose Zone Journal **2**(4): 476–491.

Hurford, A. (2009): GPS measurement error gives rise to spurious 180° turning angles and strong directional biases in animal movement data, PLoS ONE **4**(5): e5632.

Iqbal, J., Thomasson, J. A., Jenkins, J. N., Owens, P. R. and Whisler, F. D. (2005): Spatial variability analysis of soil physical properties of alluvial soils, Soil Science Society of America Journal **69**(4): 1338–1350.

Journel, A. G. and Huijbregts, C. J. (1978): Mining geostatistics, Academic Press, London.

Kasimir-Klemedtsson, Å., Klemedtsson, L., Berglund, K., Martikainen, P., Silvola, J. and Oenema, O. (1997): Greenhouse gas emissions from farmed organic soils: a review, Soil Use and Management **13**(s4): 245–250.

Kerry, R. and Oliver, M. A. (2011): Soil geomorphology: Identifying relations between the scale of spatial variation and soil processes using the variogram, Geomorphology **130**(1-2): 40–54.

Kibblewhite, M. G., Ritz, K. and Swift, M. J. (2008): Soil health in agricultural systems, Philosophical Transactions of the Royal Society B-Biological Sciences **363**(1492): 685–701.

King, D., Bourennane, H., Isambert, M. and Macaire, J. J. (1999): Relationship of the presence of a non-calcareous clay-loam horizon to DEM attributes in a gently sloping area, Geoderma **89**(1-2): 95–111.

Kitanidis, P. K. (1993): Generalized covariance functions in estimation, Mathematical Geology **25**(5): 525–540.

Kitchen, N. R., Sudduth, K. A. and Drummond, S. T. (1996): Mapping of sand deposition from 1993 midwest floods with electromagnetic induction measurements, Journal of Soil and Water Conservation **51**(4): 336–340.

Kitchen, N. R., Sudduth, K. A. and Drummond, S. T. (1999): Soil electrical conductivity as a crop productivity measure for claypan soils, Journal of Production Agriculture **12**(4): 607–617.

Knotters, M. and Bierkens, M. F. P. (2000): Physical basis of time series models for water table depths, Water Resources Research **36**(1): 181–188.

Knotters, M., Brus, D. and Oude Voshaar, J. (1995): A comparison of kriging, co-kriging and kriging combined with regression for spatial interpolation of horizon depth with censored observations, Geoderma **67**: 227–246.

Kravchenko, A. N. (2003): Influence of spatial structure on accuracy of interpolation methods, Soil Science Society of America Journal **67**(5): 1564–1571.

Kuriakose, S. L., Devkota, S., Rossiter, D. and Jetten, V. (2009): Prediction of soil depth using environmental variables in an anthropogenic landscape, a case study in the Western Ghats of Kerala, India, Catena **79**(1): 27–38.

Kvamme, K. L. (2003): Geophysical surveys as landscape archaeology, American Antiquity **68**(3): 435–457.

Landesamt für Vermessung und Geoinformation: Digitales Geländemodell 2 (DGM 2) aus Laserscanning, online: http://www.vermessung.bayern.de/geobasis_lvg/gelaendemodell/dgm2.html, cited 15 February 2012.

Lark, R. M., Stafford, J. V. and Bolam, H. C. (1997): Limitations on the spatial resolution of yield mapping for combinable crops, Journal of Agricultural Engineering Research **66**(3): 183–193.

Li, W. D., Li, B. G., Shi, Y. C. and Tang, D. Y. (1997): Application of the markov chain theory to describe spatial distribution of textural layers, Soil Science **162**(9): 672–683.

Lin, H. S., Wheeler, D., Bell, J. and Wilding, L. (2005): Assessment of soil spatial variability at multiple scales, Ecological Modelling **182**(3-4): 271–290.

Lück, E., Gebbers, R., Ruehlmann, J. and Spangenberg, U. (2009): Electrical conductivity mapping for precision farming, Near Surface Geophysics **7**(1): 15–25.

MacMillan, R. A. and Shary, P. A. (2009): Landforms and landform elements in geomorphometry, in T. Hengl and H. I. Reuter (eds), Geomorphometry, number 33 in Developments in soil science, Elsevier, S. 227–254.

Massey, R. E., Myers, D. B., Kitchen, N. R. and Sudduth, K. A. (2008): Profitability maps as an input for site-specific management decision making, Agronomy Journal **100**(1): 52–59.

McBratney, A. B., Mendoça Santos, M. L. and Minasny, B. (2003): On digital soil mapping, Geoderma **117**(1-2): 3–52.

McBratney, A. B., Odeh, I. O. A., Bishop, T. F. A., Dunbar, M. S. and Shatar, T. M. (2000): An overview of pedometric techniques for use in soil survey, Geoderma **97**(3-4): 293–327.

McBratney, A. B. and Pringle, M. J. (1999): Estimating average and proportional variograms of soil properties and their potential use in precision agriculture, Precision Agriculture **1**(2): 125–152.

McNeill, J. D. (1980a): Electrical conductivity of soils and rocks: Technical Note TN-5.

McNeill, J. D. (1980b): Electromagnetic terrain conductivity measurement at low induction numbers: Technical Note TN-6.

Mertens, F. M., Paetzold, S. and Welp, G. (2008): Spatial heterogeneity of soil properties and its mapping with apparent electrical conductivity, Journal of Plant Nutrition and Soil Science **171**(2): 146–154.

Mistele, B. and Schmidhalter, U. (2008): Spectral measurements of the total aerial N and biomass dry weight in maize using a quadrilateral-view optic, Field Crops Research **106**(1): 94–103.

Mitášová, H., Mitas, L., Brown, W. M., Gerdes, D. P., Kosinovsky, I. and Baker, T. (1995): Modeling spatially and temporally distributed phenomena - new methods and tools for GRASS GIS, International Journal of Geographical Information Systems **9**(4): 433–446.

Montagne, D., Cornu, S., Le Forestier, L. and Cousin, I. (2009): Soil drainage as an active agent of recent soil evolution: a review, Pedosphere **19**(1): 1–13.

Moore, I. D., Gessler, P. E., Nielsen, G. A. and Peterson, G. A. (1993): Soil attribute prediction using terrain analysis, Soil Science Society of America Journal **57**(2): 443–452.

Moore, I. D., Grayson, R. B. and Ladson, A. R. (1991): Digital terrain modeling - a review of hydrological, geomorphological, and biological applications, Hydrological Processes **5**(1): 3–30.

Nelson, A., Reuter, H. I. and Gessler, P. (2009): DEM production methods and sources, in T. Hengl and H. I. Reuter (eds), Geomorphometry, number 33 in Developments in soil science, Elsevier, S. 65–86.

Nelson, H. H. and McDonald, J. R. (2001): Multisensor towed array detection system for UXO detection, IEEE Transactions on Geoscience and Remote Sensing **39**(6): 1139–1145.

Nolan, B. T. (2001): Relating nitrogen sources and aquifer susceptibility to nitrate in shallow ground waters of the united states, Ground Water **39**(2): 290–299.

Pebesma, E. J. (2004): Multivariable geostatistics in s: the gstat package, Computers & Geosciences **30**(7): 683–691.

Peckham, S. D. (2009): Geomorphometry and spatial hydrologic modelling, in T. Hengl and H. I. Reuter (eds), Geomorphometry, number 33 in Developments in soil science, Elsevier, S. 579–602.

Peeters, L., Fasbender, D., Batelaan, O. and Dassargues, A. (2010): Bayesian data fusion for water table interpolation: Incorporating a hydrogeological conceptual model in kriging, Water Resources Research **46**: W08532.

Peets, S., Mouazen, A. M., Blackburn, K., Kuang, B. and Wiebensohn, J. (2012): Methods and procedures for automatic collection and management of data acquired from on-the-go sensors with application to on-the-go soil sensors, Computers and Electronics in Agriculture **81**: 104–112.

Peters, L., Daniels, J. J. and Young, J. D. (1994): Ground-penetrating radar as a subsurface environmental sensing tool, Proceedings of the IEEE **82**(12): 1802–1822.

Phillips, B. D., Skaggs, R. W. and Chescheir, G. M. (2010): A method to determine lateral effect of a drainage ditch on wetland hydrology: field testing, Transactions of the ASABE **53**(4): 1087–1096.

Pinheiro, J., Bates, D., DebRoy, S., Sarkar, D. and R Development Core Team (2012): nlme: Linear and nonlinear mixed effects models.

Pinheiro, J. C. and Bates, D. M. (2000): Mixed-Effects Models in S and S-PLUS, Springer.

Posa, D. (1989): Conditioning of the stationary kriging matrices for some well-known covariance-models, Mathematical Geology **21**(7): 755–765.

Power, J. F., Sandoval, F. M., Ries, R. E. and Merrill, S. D. (1981): Effects of topsoil and subsoil thickness on soil water content and crop production on a disturbed soil, Soil Science Society of America Journal **45**: 124.

R Development Core Team (2012): R: A language and environment for statistical computing: ISBN 3-900051-07-0.

Raes, D. and Deproost, P. (2003): Model to assess water movement from a shallow water table to the root zone, Agricultural Water Management **62**(2): 79–91.

Reitz, P. and Kutzbach, H. D. (1996): Investigations on a particular yield mapping system for combine harvesters, Computers and Electronics in Agriculture **14**(2-3): 137–150.

Rivest, M., Marcotte, D. and Pasquier, P. (2008): Hydraulic head field estimation using kriging with an external drift: A way to consider conceptual model information, Journal of Hydrology **361**(3-4): 349–361.

Robinson, D. A., Lebron, I., Lesch, S. M. and Shouse, P. (2004): Minimizing drift in electrical conductivity measurements in high temperature environments using the EM-38, Soil Science Society of America Journal **68**(2): 339–345.

Rosenberry, D. O. and Winter, T. C. (1997): Dynamics of water-table fluctuations in an upland between two prairie-pothole wetlands in north dakota, Journal of Hydrology **191**(1-4): 266–289.

Rosenbloom, N. A., Doney, S. C. and Schimel, D. S. (2001): Geomorphic evolution of soil texture and organic matter in eroding landscapes, Global Biogeochemical Cycles **15**(2): 365–381.

Ross, K. W., Morris, D. K. and Johannsen, C. J. (2008): A review of intra-field yield estimation from yield monitor data, Applied Engineering in Agriculture **24**(3): 309–317.

Rouhani, S. and Myers, D. E. (1990): Problems in space-time kriging of geohydrological data, Mathematical Geology **22**(5): 611–623.

Saey, T., Simpson, D., Vermeersch, H., Cockx, L. and Van Meirvenne, M. (2009): Comparing the EM38DD and DUALEM-21S sensors for depth-to-clay mapping, Soil Science Society of America Journal **73**: 7.

Saey, T., Simpson, D., Vitharana, U. W. A., Vermeersch, H., Vermang, J. and Van Meirvenne, M. (2008): Reconstructing the paleotopography beneath the loess cover with the aid of an electromagnetic induction sensor, Catena **74**(1): 58–64.

Saey, T., Van Meirvenne, M., De Smedt, P., Cockx, L., Meerschman, E., Islam, M. M. and Meeuws, F. (2011): Mapping depth-to-clay using fitted multiple depth response curves of a proximal EMI sensor, Geoderma **162**(1-2): 151–158.

Samouëlian, A., Cousin, I., Tabbagh, A., Bruand, A. and Richard, G. (2005): Electrical resistivity survey in soil science: a review, Soil and Tillage Research **83**(2): 173–193.

Sayers, M. W. (1991): Exact equations for tractrix curves associated with vehicle offtracking, Vehicle System Dynamics **20**(5): 297–308.

Schmidhalter, U. and Oertli, J. J. (1993): Capillary rise from the groundwater table in silty and loamy multi-layered sand soils, Zeitschrift für Kulturtechnik und Landentwicklung **34**(5): 279–288.

Schnyder, H., Schwertl, M., Auerswald, K. and Schäufele, R. (2006): Hair of grazing cattle provides an integrated measure of the effects of site conditions and interannual weather variability on δ^{13}C of temperate humid grassland, Global Change Biology **12**(7): 1315–1329.

Schumann, A. W. and Zaman, Q. U. (2003): Mapping water table depth by electromagnetic induction, Applied Engineering in Agriculture **19**(6): 675–688.

Sheets, K. R. and Hendrickx, J. M. H. (1995): Noninvasive soil water content measurement using electromagnetic induction, Water Resources Research **31**: 2401.

Sherlock, M. D. and McDonnell, J. J. (2003): A new tool for hillslope hydrologists: spatially distributed groundwater level and soilwater content measured using electromagnetic induction, Hydrological Processes **17**(10): 1965–1977.

Shiyomi, M., Okada, M., Takahashi, S. and Tang, Y. (1998): Spatial pattern changes in aboveground plant biomass in a grazing pasture, Ecological Research **13**(3): 313–322.

Simbahan, G. C., Dobermann, A. and Ping, J. L. (2004): Site-specific management - screening yield monitor data improves grain yield maps, Agronomy Journal **96**(4): 1091–1102.

Sinowski, W. and Auerswald, K. (1999): Using relief parameters in a discriminant analysis to stratify geological areas with different spatial variability of soil properties, Geoderma **89**(1-2): 113–128.

Skaggs, R. W., Brevé, M. A. and Gilliam, J. W. (1994): Hydrologic and water-quality impacts of agricultural drainage, Critical Reviews in Environmental Science and Technology **24**(1): 1–32.

Skaggs, R. W., Chescheir, G. M. and Phillips, B. D. (2005): Methods to determine lateral effect of a drainage ditch on wetland hydrology, Transactions of the ASAE **48**(2): 577–584.

Skog, I. and Händel, P. (2009): In-car positioning and navigation technologies - a survey, IEEE Transactions on Intelligent Transportation Systems **10**(1): 4–21.

Slavich, P. (1990): Determining EC_a-depth profiles from electromagnetic induction measurements, Australian Journal of Soil Research **28**(3): 443–452.

Sonka, S. T., Bauer, M. E., Cherry, E. T., Colburn, J. W., Heimlich, R. E., Joseph, D. A., Leboeuf, J. B., Lichtenberg, E., Mortensen, D. A., Searcy, S. W., Ustin, S. L. and Ventura, S. J. (1997): Precision agriculture in the 21st century: Geospatial and information technologies in crop management, National Academies Press, Washington, D.C.

Speckmann, H. (2000): Providing measured position data for agricultural machinery, Computers and Electronics in Agriculture **25**(1-2): 87–106.

Speckmann, H. and Jahns, G. (1999): Development and application of an agricultural BUS for data transfer, Computers and Electronics in Agriculture **23**(3): 219–237.

Sudduth, K. A., Bollero, N. R., Bullock, G. A. and Wiebold, D. G. (2003): Comparison of electromagnetic induction and direct sensing of soil electrical conductivity, Agronomy Journal **95**(3): 472.

Sudduth, K. A. and Drummond, S. T. (2007): Yield editor: Software for removing errors from crop yield maps, Agronomy Journal **99**(6): 1471–1482.

Sudduth, K. A., Drummond, S. T. and Kitchen, N. R. (2001): Accuracy issues in electromagnetic induction sensing of soil electrical conductivity for precision agriculture, Computers and Electronics in Agriculture **31**(3): 239–264.

Sudduth, K. A. and Hummel, J. W. (1993): Soil organic-matter, CEC, and moisture sensing with a portable NIR spectrophotometer, Transactions of the ASAE **36**(6): 1571–1582.

Sudduth, K. A., Kitchen, N. R., Myers, D. B. and Drummond, S. T. (2010): Mapping depth to argillic soil horizons using apparent electrical conductivity, Journal of Environmental & Engineering Geophysics **15**(3): 135.

Tantum, S. L., Collins, L. M., Khadr, N. and Barrow, B. J. (2003): Correcting GPS measurement errors induced by system motion over uneven terrain, Proceedings of SPIE **5089**: 1105–1115.

Tantum, S. L., Zhu, Q., Torrione, P. A. and Collins, L. M. (2009): Modeling position error probability density functions for statistical inversions using a Goff-Jordan rough surface model, Stochastic Environmental Research and Risk Assessment **23**(2): 155–167.

Tarokh, A. B. and Miller, E. L. (2007): Subsurface sensing under sensor positional uncertainty, IEEE Transactions on Geoscience and Remote Sensing **45**(3): 675–688.

Tiwari, H. K. and Elston, R. C. (1999): The approximate variance of a function of random variables, Biometrical Journal **41**(3): 351–357.

Tonkin, M. J. and Larson, S. P. (2002): Kriging water levels with a regional-linear and point-logarithmic drift, Ground Water **40**(2): 185–193.

Torisu, R., Mugucia, S. W. and Takeda, J. (1992): The kinematics and open-loop characteristics of tractor-trailer combinations, Journal of the Faculty of Agriculture, Iwate University **20**: 299–314.

Traub, F. (1956): Hydrogeologische Übersichtskarte 1:500 000 - Erläuterungen zu Blatt München, Bundesanstalt für Landeskunde, Remagen.

Triantafilis, J. and Monteiro Santos, F. A. (2009): 2-Dimensional soil and vadose-zone representation using an EM38 and EM34 and a laterally constrained inversion model, Australian Journal of Soil Research **47**(8): 809–820.

Tòth, J. (1963): A theoretical analysis of groundwater flow in small drainage basins, Journal of Geophysical Research **68**(16): 4795–4812.

van Bergeijk, J., Goense, D., Keesman, K. J. and Speelman, L. (1998): Digital filters to integrate global positioning system and dead reckoning, Journal of Agricultural Engineering Research **70**(2): 135–143.

Van Oost, K., Van Muysen, W., Govers, G., Deckers, J. and Quine, T. A. (2005): From water to tillage erosion dominated landform evolution, Geomorphology **72**(1-4): 193–203.

von Asmuth, J. R. and Knotters, M. (2004): Characterising groundwater dynamics based on a system identification approach, Journal of Hydrology **296**(1-4): 118–134.

Western, A. W., Grayson, R. B., Blöschl, G., Willgoose, G. R. and McMahon, T. A. (1999): Observed spatial organization of soil moisture and its relation to terrain indices, Water Resources Research **35**(3): 797–810.

Zhang, Q. and Qiu, H. (2004): A dynamic path search algorithm for tractor automatic navigation, Transactions of the ASAE **47**(2): 639–646.

Zimmerman, D. L. (1993): Another look at anisotropy in geostatistics, Mathematical Geology **25**(4): 453–470.